MASTER

Analysis and design of a rotary and a linear actuator for 2-DoF applications

Meessen, K.J.

Award date:
2008

TU/e technische universiteit eindhoven

Capaciteitsgroep Elektrische Energietechniek
Electromechanics & Power Electronics

Master of Science Thesis

Analysis and design of a rotary and a linear actuator for 2-DoF applications

K.J. Meessen
EPE.2008.A.01

Coaches:

dr. J.J.H. Paulides, TU/e
dr. E.A. Lomonova, TU/e
ir. R.A.J. van der Burg, Assembléon

January 30, 2008

/ faculteit elektrotechniek

Analysis and design of a rotary and a linear actuator for 2-DoF applications

K.J. Meessen*
University of Technology Eindhoven & Assembléon

Supervisors:
Dr. J. J. H. Paulides (TU/e)
Dr. E. A. Lomonova (TU/e)
Ir. R. A. J. van der Burg (Assembléon)

January 30, 2008

*k.j.meessen@student.tue.nl

Contents

Abstract

This thesis describes the multi-physical analysis of a linear and a rotary actuator to apply in a rotary-linear motion system. Using semi-analytical field equations, several models are derived to develop a fast design tool.

The first part of this research presents the analysis of a linear actuator. In the analysis, four different topologies of a slotless tubular permanent magnet actuator (TPMA) are investigated. Using axial symmetry and Fourier theory, a unified semi-analytical solution for the magnetic field equations of the four topologies is derived in a two-dimensional axisymmetric coordinate system. Using these semi-analytical field equations, a time efficient analysis is performed on the magnetic field in the actuator. Several magnetostatic models are implemented and coupled to electrical and thermal equations to design a TPMA for a high acceleration motion profile. Two topologies showed to be favorable for high acceleration applications and one of them is realized by means of a prototype.

The second part focusses on the rotary part of the two degrees of freedom (2-DoF) system. In the first Section of this part, eddy current losses of the currently used rotary actuator are calculated. The effect of using a solid steel back-iron instead of a laminated steel back-iron is investigated using a finite element analysis (FEA). The calculations are compared to measurements. To analyse and design a rotary actuator, semi-analytical models are derived for a slotless permanent magnet actuator for two different rotor topologies, i.e. parallel magnetized and radially magnetized. The magnetic behavior of both models is analyzed and compared by a parametric search on geometric parameters. The magnetostatic models are coupled to thermal models to calculate the torque capabilities.

Publications

The various outcomes of this thesis have led to the following publications:

- K. J. Meessen, E. A. Lomonova, J. J. H. Paulides, "Multi-physical Analysis and Design of a Slotless Tubular PM Actuator for High Acceleration Applications", *IEEE Transactions on Magnetics,* pp. 1-8, in review process.

- K. J. Meessen, J. J. H. Paulides, and E. A. Lomonova, "Eddy-current stator solid steel back-iron losses in small brushless permanent magnet machines", *IEEE International Magnetics Conference Madrid, Spain, May 2008,* pp. 1-3

During the master phase, a traineeship at the Royal Institute of Technology (KTH) Stockholm has led to another publication:

- K. J. Meessen, P. Thelin, J. Soulard, and E.A. Lomonova, "Inductance Calculations of PMSMs with FEM Including PM Flux Change, Self- and Cross-Saturations", *IEEE Transactions on Magnetics,* pp. 1-8, to be published in 2008.

Acknowledgements

This work is established at the University of Technology Eindhoven in the group of Electromechanics and Power Electronics (EPE) of the department of Electrical Engineering in close cooperation with Assembléon. I want to thank all people who were involved in my graduation project. Especially I want to thank Johan Paulides and Elena Lomonova for the direct coaching of my project and for all the feedback on my work, and Assembléon, represented by Rik van der Burg, for the possibility of working on this project.

Many thanks to Bart Gysen for all the useful information on semi-analytical field solutions and his help by solving the axially magnetized topology and many other problems. Furthermore, thanks to Teun Oome and Hans Rovers for sharing IM 0.12 with me and their help in general. Finally, I would like to thank Marijn Uyt De Willigen for his help on the prototype at the very last moment.

List of symbols

Symbols

$\vec{A}$	Magnetic vector potential	Wb m^{-1}
$\vec{B}$	Magnetic flux density	T
B_g	Magnetic loading in the airgap	T
B_{rem}	Remanent flux density	T
C_i	Coefficient	-
D	Duty cycle	-
F	Force	N
$\vec{H}$	Magnetic field strength	A m^{-1}
I	Current	A
J_m	Moment of inertia	kg m^2
J	Current density	A m^{-2}
L	Length	m
L	Inductance	H
$\vec{M}$	Magnetization	A m^{-1}
M	Mutual inductance	H
N_{turns}	Number of turns	-
N_{coils}	Number of coils	-
P	Power	W
Q	Electrical loading	A
R	Radius	m
R	Resistance	Ω
T	Torque	N m
U	Voltage	V
a	Acceleration	m s^{-2}
a_i	Coefficient	-
b_i	Coefficient	-
d	Distance	m
e	Electro motive force (EMF)	V
f	Frequency	Hz
h	Heat transfer coefficient	W m^{-2} K^{-1}
i	Current	A
j	Harmonic number	-
k_p	Packing factor	-
l	Length	m
m	Mass	kg
m_n	Spatial frequency	m^{-1}
n	Harmonic number	-
p	Number of pole pairs	-
q_j	Spatial frequency	m^{-1}
r	Radial position	m
$\vec{r}$	Unit vector	-

t	Time	s
u	Voltage	V
v	Velocity	m s^{-1}
z	Axial position	m
$\vec{z}$	Unit vector	-
α	Angular acceleration	rad s^{-2}
α_p	Magnet pitch to pole pitch ratio	-
ΔT	Temperature gradient	K
ε	Function of j and n	-
η	Function of j and n	-
θ	Rotation around z	rad
$\vec{\theta}$	Unit vector	-
μ_0	Permeability of vacuum	H m^{-1}
μ_r	Relative permeability	-
ρ	Resistivity	Ω m
σ	Function of j and n	-
τ_{mr}	Axial length of radially magnetized magnet	m
τ_{mz}	Axial length of axially magnetized magnet	m
τ_p	pole pitch	m
φ	magnetic scalar potential	A
ω	Angular velocity	rad s^{-1}
$\mathcal{B}_{I0}$	Bessel function of first kind of 0^{th} order	-
$\mathcal{B}_{I1}$	Bessel function of first kind of 1^{th} order	-
$\mathcal{B}_{K0}$	Bessel function of second kind of 0^{th} order	-
$\mathcal{B}_{K1}$	Bessel function of second kind of 1^{th} order	-
$\mathcal{F}$	Magneto-motive force	A
$\mathcal{K}$	Function	-
$\mathcal{R}$	Reluctance	H^{-1}

Subscripts

I	In Region I
II	In Region II
III	In Region III
g	In the center of the airgap
r	In the radial direction
z	In the axial direction
θ	In the circumferential direction

Acronyms

EMF	Electro motive force
FE	Finite Element
FEA	Finite Element Analysis
FEM	Finite Element Method
MEC	Magnetic equivalent model
MMF	Magneto motive force
RMS	Root mean square
THD	Total harmonic distortion

Chapter 1

Introduction

Assembléon is a world-wide supplier of Surface Mount Technology (SMT) placement solutions. The Surface Mounted Devices (SMD) are placed on Printed Circuit Boards (PCB) using pick-and-place (P&P) machines. An ever increasing demand for more cost-effectiveness solutions drives Assembléon towards a redesign of their P&P machines. This redesign should increase the current capacity of 150k components per hour, increase the functionality, and lower the costs.

One P&P machine contains several *placement robots* in series which provide the pick and place operation. This robot consist of a computer for control, a feeder trolley to provide a reel with components, and a moveable placement module for the pick and place action. This placement module is mounted on a linear actuator to move in the x-axis (short stroke direction) which is mounted on a spindle to move in the y-axis (the long stroke direction). This work focusses on the placement module.

1.1 The placement module

The placement module contains a linear actuator to move in the z-direction to pick and place a component, and a rotary actuator to be able to orient the component in the desired direction. The linear actuator is a voice-coil actuator which moves the complete rotating actuator up and down to pick and place components as shown in Fig. 1.1.

The shaft of the rotary actuator is hollow to feed through a vacuum to be able to pick a component. After the component is picked, the linear actuator will move this component up. A camera module placed on the placement module will identify the component and the rotary actuator orient the component in the desired direction.

In the current solution, the rotary actuator is directly mounted on the moving part of the voice coil actuator. The expectation is that combining both actuators will increase the efficiency. The goal of this work is to develop two actuators which can be combined to get a more efficient system.

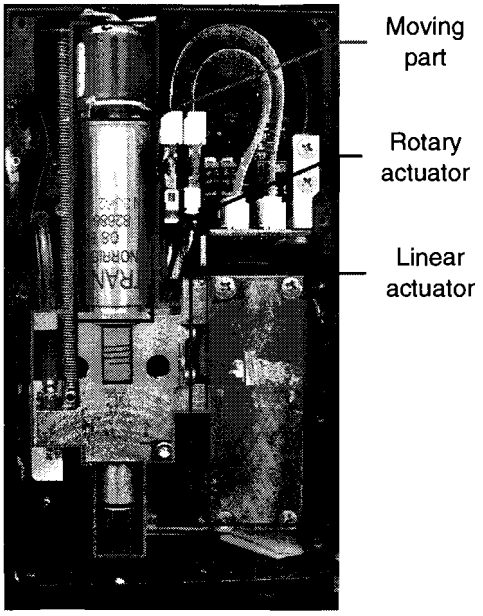

Figure 1.1: Current Assembléon pick and place module.

1.2 Requirements and Specifications

In the previous section is stated that the complete placement module contains two actuators which have to be combined in one system. This system has one translator which can move in the θ-direction (rotate), and move in the z-direction (linear). In this section, the requirements for the separate actuators, as well as for the complete system are given.

1.2.1 Rotary actuator

Table 1.1 shows the specifications of the rotary (θ) actuator. The estimated load inertia is based on the current design of the rotary actuator. The main part of the load inertia is caused by the magnet, the inertia of the shaft, the nozzle, and the component is negligible.

Table 1.1: Specifications of the theta-actuator

Parameter	Value
Estimated friction torque	2 mNm
Estimated load inertia	$5.0\text{x}10^{-7}$ kgm^2
Peak acceleration	$\leq$ 3500 rad/s^2
Maximum velocity	$\leq$ 125.6 rad/s (20 Hz)
Duty cycle	$\leq$ 54%
Continuous mechanical power	127mW

Figure 1.2 gives the worst case motion profile of the θ-actuator. Directly after the pick-action, the actuator starts to rotate to orient the component. In this worst case situation, the actuator rotates 540 degrees to orient the component in the right position. The nozzle, placed at the end of the shaft to pick a component, has to be rotated to its starting position

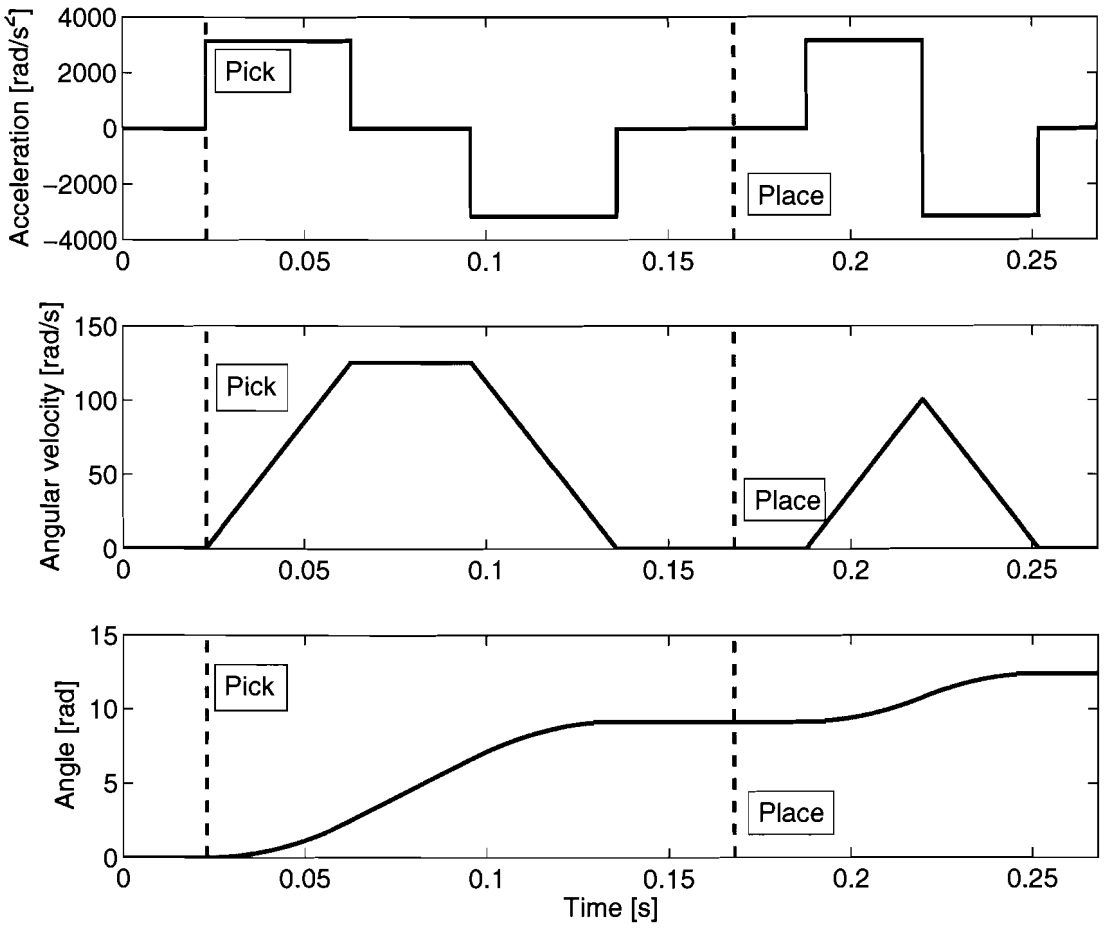

Figure 1.2: Worst case rotary actuator motion profile. This cycle is continuously repeated.

after the place action. As can be seen from the motion profile of the angle, the rotor always turns in one direction. This is done to avoid wear of the seals between the vacuum tube and the shaft.

During one complete cycle, the actuator is four times accelerated with the maximum acceleration/deceleration. This four accelerations take 144 ms in total. One complete cycle is 268 ms. Therefore, the worst case duty cycle is:

$$D_{theta} = 54\%. \tag{1.1}$$

The total maximum estimated torque T_{total} is

$$T_{total} = J_m\alpha + T_{friction} = 3.75\text{mNm}, \tag{1.2}$$

where J_m is the moment of inertia of the rotor and the load, α the maximum angular velocity, and $T_{friction}$ is the friction torque. The angular velocity ω increases linearly during maximum acceleration. Therefore, the mean value of the angular velocity during maximum acceleration is used to calculate the mean mechanical power during maximum acceleration

$$P = \omega T_{total} = 235\text{mW}. \tag{1.3}$$

The continuous mechanical power during one cycle is

$$P_{continuous} = 159\text{mW}. \tag{1.4}$$

The total power dissipated in the actuator is higher due to iron losses and joule losses in the windings.

1.2.2 Linear actuator

The specifications of the linear actuator are listed in Table 1.2. The static force of 41 N is used to put components into connectors at the PCB. The total payload of the z-actuator includes its mover and the rotary actuator since they are mounted on the same shaft. The estimated payload mass is 0.13 kg. Figure 1.3 shows the motion profile of the z-actuator.

Table 1.2: Specifications of the z-actuator

Parameter	Value
Stroke	35 mm
Peak acceleration	150 m/s^2
Maximum speed	2 m/s
Static force	41 N (for 250 ms)
Estimated payload mass	0.13 kg
Duty cycle	34 %
Continuous mechanical power	5.7 W

At $t = 0$, the shaft starts to move downwards to pick a component. The acceleration is equal to the maximum acceleration until the position of the shaft is at -10 mm. After this position, the actuator starts to decelerate to have velocity equal to zero at the moment the system picks a component. When the component is picked from the reel, the shaft moves upwards until position $z = 0$ is reached. The shaft starts to move downwards when the place-position on the PCB is reached and the same movement is repeated.

The z-actuator moves with the positive respectively negative maximum acceleration during 92 ms. With a total worst case cycle time of 268 ms the duty cycle of the z-actuator is

$$D_z = 34\%. \tag{1.5}$$

Accelerating the payload mass at the maximum acceleration gives a force and mechanical power

$$F = 19.50\text{N}, \tag{1.6}$$

$$P = 16.77\text{W}. \tag{1.7}$$

Where P is the mean mechanical power during maximum acceleration. The continuous mechanical power during one complete cycle is

$$P_{continuous} = 5.7\text{W}. \tag{1.8}$$

Note that the total power dissipated in the actuator is higher due to iron losses and copper losses.

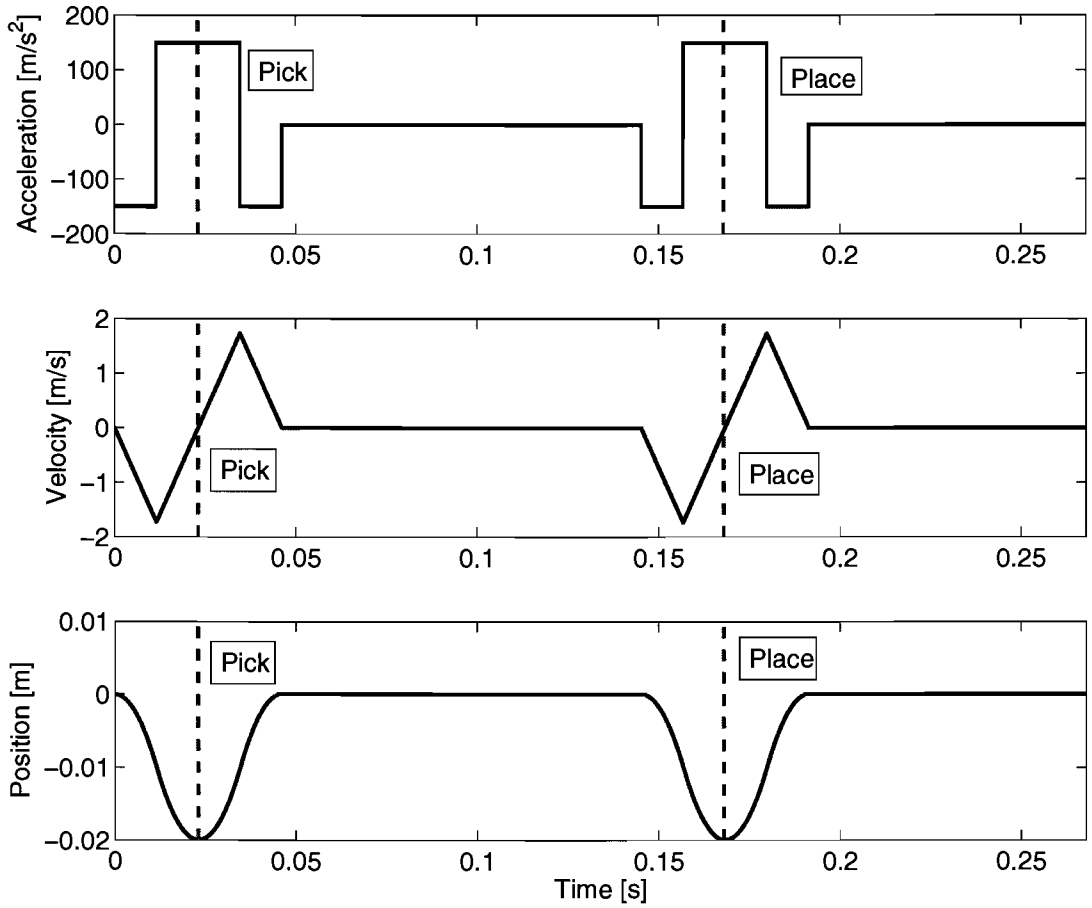

Figure 1.3: Worst case z-actuator motion profile. This cycle is continuously repeated.

1.2.3 System

The placement module uses a vacuum to pick the component from a reel. To be able to feed through this vacuum, the shaft has to be hollow. Therefore, the rotor diameter has to be at least 4 mm. The space for the two actuator is limited in the placement module. Table 1.3 gives the dimensions for the combination of the two actuators.

Table 1.3: Specifications of the system

Parameter	Value
Inner diameter shaft	$\geq$2.5 mm
Outer diameter stator	$\leq$18.0 mm
Length	$\leq$140.0 mm

1.3 Rotary-linear motion

The combination of rotational and linear motion is widely used in modern tooling machines and robotics. In conventional machinery, this two-degrees of freedom (2-DoF) motion is realized by combining a conventional rotary and linear actuator. The major disadvantages of this solution are the relatively high moving mass, as the linear actuator has to move the complete rotary actuator, and the moving cables for the rotary actuators, especially in quick motion applications.

In literature, several combinations of linear and rotary actuators are presented. Some interesting examples are presented in the next section.

1.3.1 Review of existing rotary-linear motion systems

Switched reluctance machines

In [12] and [13], a switched reluctance machine (SRM) is proposed as a candidate to provide the 2-degrees of freedom. The system consist of one translator and multiple stators which can be controlled independently as shown in Fig. 1.4. Simultaneously, but unequal excitation of the same windings in each stator produces the torque and the force. The torque, T, is the

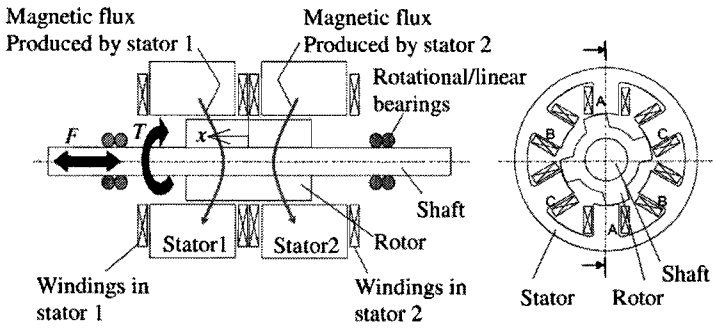

Figure 1.4: Rotary-linear system using two switched reluctance machines [13].

sum of the same directional reluctance torque on the part of the translator in both stator 1 and stator 2. The force in the x-direction is produced by the difference in excitation of both stators.

In [13] is shown that the two degrees of freedom can be controlled independently. However, the force density of the actuator is low and as a result of stacking multiple rotary actuators, the number of end windings is increased. This results in more losses as the end-windings do not contribute in the force or the torque production.

Induction machines

A second class of machines used for rotary-linear systems is the induction machine. Several publications are found where induction machines are combined to provide the 2-DoF. In [14], shows another example of stacking multiple rotary actuators in the axial direction two provide the thrust force. By controlling the phase of the supply voltage for each stator winding, the translator can produce a rotary, linear and a combined motion.

[15] presents a linear helical-motion induction motor that can be used in stacked arrangement to provide pure rotary, pure linear, or helical motion. One motor produces a helical motion due to skewed windings and different conductor layers in the rotor.

In [16] a 2-DoF system consisting one translator and two stators is proposed for a pick and place module. As can be seen in Fig. 1.5, the winding configuration of the stator providing linear motion, and the winding configuration of the stator providing the rotary motion are different. By changing the axial length of the two stators, the system provides more force or

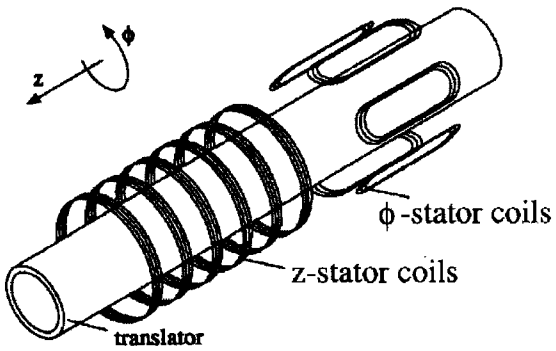

Figure 1.5: Rotary-linear system using two induction motors on one translator [16].

torque.

As for the switched reluctance motor, the power density of the induction motor is lower than the power density of an actuator system using permanent magnet materials. Another disadvantage of the induction motor is the heat generated in the rotor. However, an advantage of an induction motor is the easy and low cost geometry, e.g. the translator in the induction machine in Fig. 1.5 is an aluminium tube without any permanent magnet material.

Permanent magnet machines

Patents [17],[18], and [19] show rotary-linear actuators with permanent magnets. In [20], an detailed overview of some rotary-linear actuators is given and a new design is proposed. This design is optimized for high speed applications and focusses mainly on the mechanical design of the system. The system is based on two actuators having one translator and two stators with air-bearings in between. The thesis show interesting mechanical aspects, e.g. different bearing types and sensing methods. However, in this thesis the design is focussed on the electromagnetic design.

Patent [17] is a system based on one translator with two different magnetization patterns for the two DoF. These two patterns interact with two different coil sets as shown in Fig. 1.6. One coil set is wounded in the longitudinal direction to create torque, and the second coil set is wounded in the circumferential direction to create linear force. The topology of the rotary-linear actuator in this thesis is similar to this actuator with one translator and two different magnetization patterns. However, it will be optimized for very high acceleration levels in the z-direction.

In [18] and [21], an actuator is presented with only one magnetization pattern on the translator and two sets of coils to provide the two motion directions. Fig. 1.7a shows the

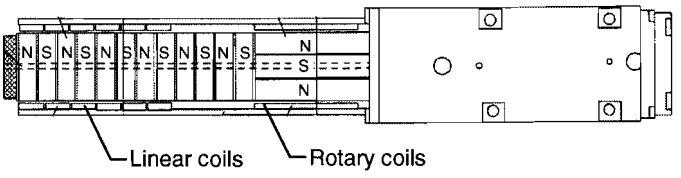

Figure 1.6: Rotary-linear system using one translator with two magnetization patterns [17].

topology of one of the actuators. Both actuators in [18] and [21] have a translator with a

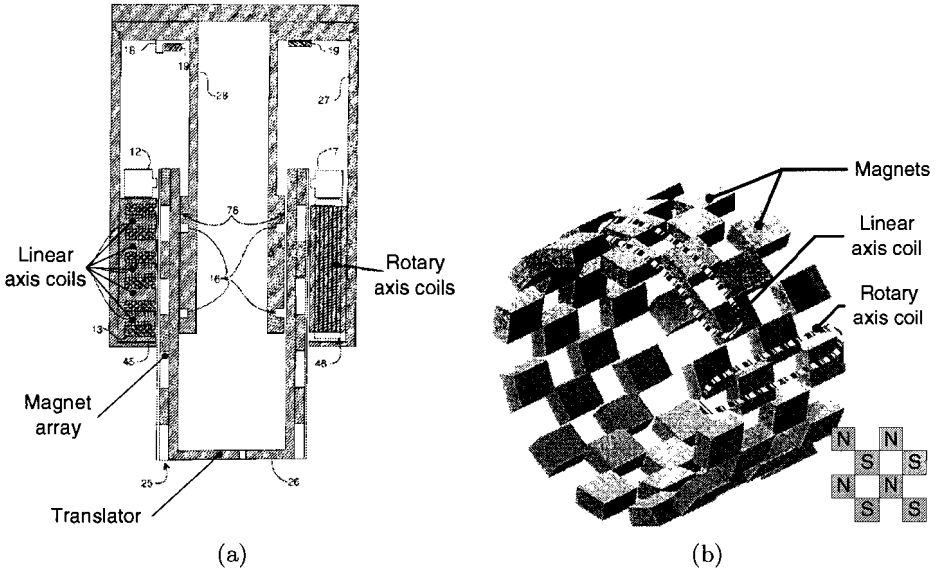

Figure 1.7: Rotary-linear system using one translator with a checkerboard magnetization pattern. (a) The complete actuator, (b) the magnetization pattern [18].

checkerboard magnetization pattern as shown in Fig. 1.7b. Two different sets of coils are placed at both sides of the translator. One set has windings oriented in the axial direction to provide rotary motion, the second set has radial oriented windings to provide linear motion as shown in Fig. 1.7b. Using one magnetization pattern for rotation and translation requires less translator length. However, as can be seen in Fig. 1.7b, with this magnetization pattern only 50% of the translator surface is covered with magnets, thus theoretically the efficiency is 50% compared to a regular machine.

As the requirements of the P&P application here desires a high force density, the actuator presented in [18] does not seem to be appropriate. However, using one magnetization pattern on the translator is an interesting option.

The last permanent magnet rotary-linear actuator reviewed here is patent [19], which presents an actuator for a P&P application. The actuator comprises two single-phase Lorentz force actuators as can be seen in Fig. 1.8. The stator has a soft-magnetic core with a cylindrical coil around it for the linear force, and a shell with a toroidal coil for the rotational

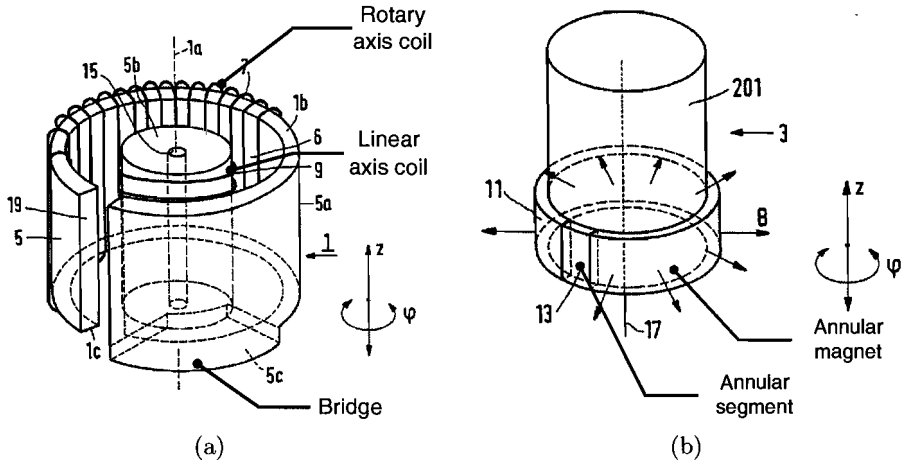

Figure 1.8: Rotary-linear system comprising two single-phase Lorentz force actuators. (a) The stator part, (b) the translator part [19].

force. The translator consists of a radially magnetized annular magnet, interrupted by an annular segment magnetized in the opposite direction. Linear force is produced by interaction of the cylindrical coil and the annular shaped magnet. The rotational force is created by interaction of the toroidal coil and the magnetic translator. The magnetic flux due to the magnet ring leaves the rotor, links the toroidal coil and passes through the bridge and the core back to the magnet ring. Due to the gap in the shell, the flux is forced to link the toroidal coil always in the same direction. The flux linkage of the toroidal coil changes due to the oppositely magnetized annular segment. Therefore, a rotational force can be produced when the annular segment is located within the angular extend of the toroidal coil.

This actuator provides in a compact and simple way both rotational and linear force. However, due to the large airgap and the incomplete use of the magnet for linear motion, this actuator has a low power density.

Chapter 2

Linear actuator

In this chapter, a linear actuator is analyzed and designed to provide the force in the z-direction. A moving magnet tubular actuator, as shown in Fig. 2.1, is chosen to be the best actuator to produce the force in this application. The main reason to choose this topology is the round translator, this translator can rotate without disturbing the linear force production. Therefore, the combination with a rotary actuator becomes easier. A second reason is the high force density of this type of actuators and the absence of end-windings.

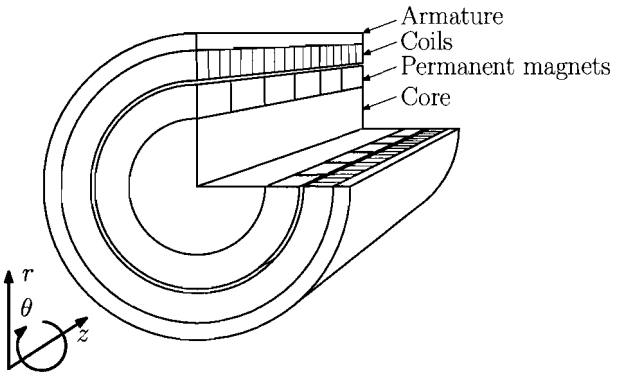

Figure 2.1: Slotless tubular permanent magnet actuator.

Due to the small size of the actuator, a slotless topology is chosen. This structure is easier to manufacture as the resulting armature is a simple hollow tube. A second advantage is the smoother force characteristic due to the absence of slot cogging. However, slotless actuators have a larger effective airgap and therefore a lower magnetic loading. This reduces the force density of the actuator [22].

The thrust force of a TPMA can be expressed in terms of the *magnetic loading* and the *electrical loading*

$$F_{thrust} = B_g L_{active} \pi D_g Q, \tag{2.1}$$

where B_g is the *magnetic loading* in the airgap, Q is the *electrical loading*, L_{active} is the active length of the stator of the TPMA, and D_g is the airgap diameter [23]. When only the translator mass is considered as load and friction is neglected, the acceleration capability of

the actuator is

$$a = \frac{F_{thrust}}{m_{translator}}, \tag{2.2}$$

where the mass of the translator, which is a cylinder, is

$$m_{translator} \propto R^2. \tag{2.3}$$

As can be seen, the force increases linearly with the radius, while the mass increases with the radius squared. Therefore, the acceleration decreases linearly with the radius, thus a small radius is favorable for a high acceleration level.

The first part of this section presents the models of different topologies and a parametric search on the magnetic loading. In the second part the electrical loading and the force are analyzed. Two final designs are presented at the end of the chapter. The actuator here is designed without taken into account the rotary motion.

2.1 Magnetic loading in the z-actuator

In this section, general expressions are derived to describe the magnetic field produced by the magnets in the tubular actuator. Four different topologies are analyzed. First, the topology with radially magnetized surface-mounted magnets is presented, the second topology is a tubular actuator with an Halbach magnet array and a soft-magnetic core, the third topology is a Halbach magnet array with a non-magnetic core, and the last topology is a tubular actuator with axial magnetized magnets separated by soft-magnetic pole pieces. The actuators have a slotless stationary part with coils and a mover with surface mounted magnets.

The topologies are analyzed using semi-analytical models. In these models the following assumptions are made:

1. The permanent magnets have a linear demagnetization characteristic, and are fully magnetized in the direction of magnetization.

2. The mover is assumed to be infinitely long, the end effects are neglected

3. The stator and mover back-iron are infinitely permeable.

The permanent magnets in the analysis are modeled as magnets with a remanent flux density, B_{rem}, of 1.2T and a relative permeability, μ_r of 1.05. The demagnetization curve is shown in Fig. 2.2a.

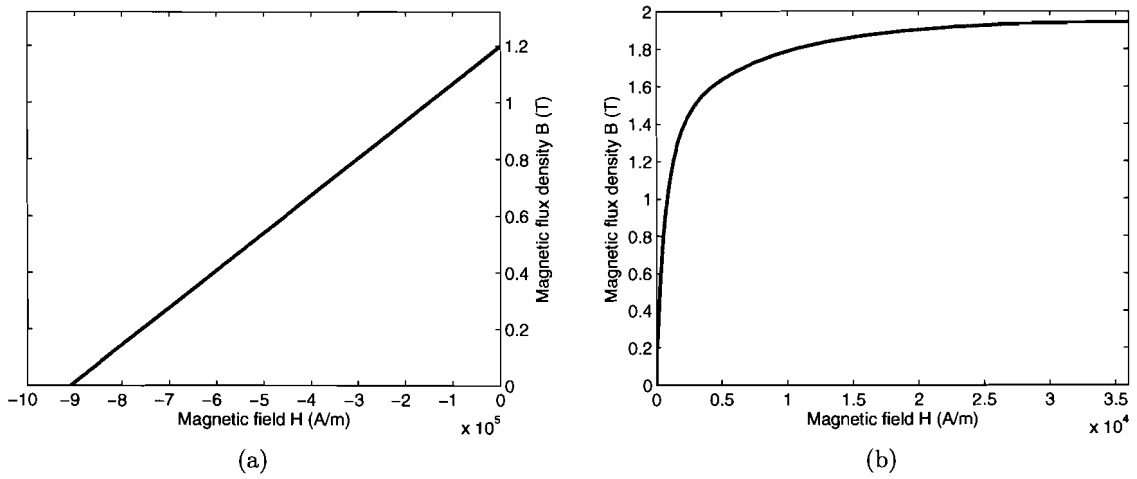

Figure 2.2: (a) Demagnetization curve of the permanent magnets. (b) BH-curve of mild steel AI1010.

2.1.1 Saturation

As the permeability of the iron parts in the actuator is a non-linear function of the flux, the third assumption is only valid when the iron is not saturated. Fig. 2.2b shows the non-linear behavior of mild steel AI1010, which is often used in actuators. To verify assumption three, the influence of the non-linear behavior of the iron parts on the magnetic loading of the actuator is calculated using a simple magnetic equivalent circuit (MEC). Fig. 2.3 shows the MEC of a radial magnetized tubular actuator. The reluctances in the circuit are representing

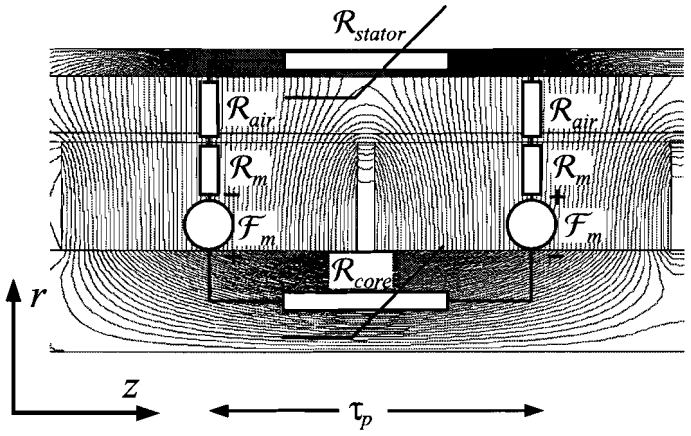

Figure 2.3: Magnetic equivalent circuit of one pole-pair of a radial magnetized tubular actuator.

the different materials in the actuator where the reluctance is

$$\mathcal{R} = \frac{l}{\mu_0 \mu_r A} \tag{2.4}$$

where l is the radial length, A is the area in the angular direction, μ_r is the relative permeability and μ_0 is the permeability of vacuum. The reluctances representing the iron parts,

$\mathcal{R}_{stator}$ and $\mathcal{R}_{core}$ are non-linear. The magnetomotive force (MMF) source, $\mathcal{F}_m$, represents the magnets.

To calculate the influence of $\mathcal{R}_{stator}$ on the magnetic loading, $\mathcal{R}_{core}$ is set to infinity, the influence of $\mathcal{R}_{core}$ is calculated with $\mathcal{R}_{stator} = \infty$. As can be seen in Fig. 2.3, it is hard to define the reluctance $\mathcal{R}_{stator}$ and $\mathcal{R}_{core}$ as one reluctance because the flux density in these regions is not uniformly distributed. Therefore, the reluctances are worst case models where the assumption is made that the length of the reluctance is τ_p and that the flux density in this part is uniform.

$$\mathcal{R}_{air} = \frac{l_g + l_{coil}}{\mu_0 \tau_p 2\pi R_{air}}, \tag{2.5}$$

$$\mathcal{R}_m = \frac{l_m}{\mu_0 \mu_r \tau_p 2\pi R_m}, \tag{2.6}$$

$$\mathcal{R}_{stator} = \frac{\tau_p}{\mu_0 \mu_r l_{stator} 2\pi R_{stator}}, \tag{2.7}$$

$$\mathcal{R}_{core} = \frac{\tau_p}{\mu_0 \mu_r l_{core} 2\pi R_{core}}, \tag{2.8}$$

where $R_{air}, R_m, R_{stator}, R_{core}$ are the radii at the middle of the different parts. The values for the geometric parameters are shown in Table 2.1. Fig. 2.4 shows the effect of the increasing

Table 2.1: Geometric parameters for the saturation model

R_{out} (mm)	9.00
l_{stator} (mm)	1.00
l_{coil} (mm)	1.50
l_g (mm)	0.20
l_{core} (mm)	2.00
τ_p (mm)	8.50

flux density in the stator and the core on the total reluctance of the flux path. As the magnetic loading is proportional to the inverse of the reluctance, the magnetic loading decreases rapidly for a flux density higher than 1.5 T in the iron parts of the actuator. Therefore, to ensure that assumption three is valid, a constraint is added to the analysis that the flux density is below 1.5 T in the iron parts.

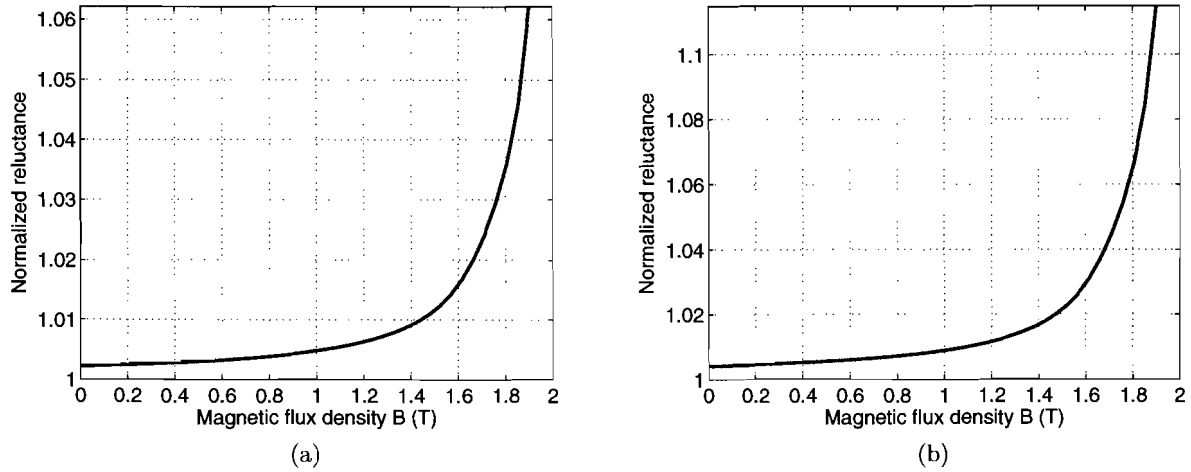

Figure 2.4: Influence of increasing flux density in the (a) stator and (b) core of the actuator on the total reluctance of the flux path.

2.1.2 Magnetic vector potential

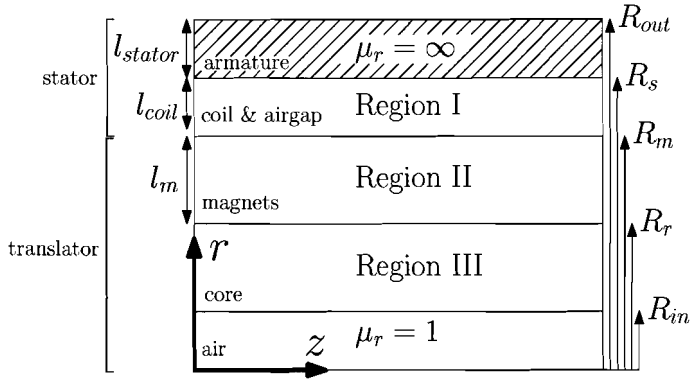

Figure 2.5: Regions in the tubular actuator.

To calculate the magnetic field produced by the magnets, three regions are considered as shown in Fig. 2.5. Region I is the source free airspace/winding region, region II is the magnet region, and region III is the core region. Region III can be either non-magnetic or soft-magnetic. In case that region III is non-magnetic, this region has to be considered as a source-free region. Otherwise, region III is not considered as a region but replaced by a boundary condition at $r = R_r$. The magnetic field equations are solved in the $r-z$ coordinate system using the magnetic vector potential, $\vec{A}$, which is defined as [7]

$$\vec{B} = \nabla \times \vec{A}, \tag{2.9}$$

where

$$\vec{B} = \mu_0 \vec{H} \quad \text{in the source free air-space region (I,III),} \tag{2.10}$$
$$\vec{B} = \mu_0(\mu_r \vec{H} + \vec{M}) \quad \text{in the magnet region (II).} \tag{2.11}$$

The flux density $\vec{B}$, which has only a component in the $\vec{r}$ and a component in the $\vec{z}$ direction, results in only a A_θ component. Therefore, the vector potential becomes a scalar. The flux density can be written as

$$\vec{B} = B_r \vec{r} + B_z \vec{z}, \tag{2.12}$$
$$B_r = -\frac{\partial A_\theta}{\partial_z}, \tag{2.13}$$
$$B_z = \frac{\partial}{r \partial r}(r A_\theta) \tag{2.14}$$

The governing magnetic field equations in terms of the vector magnetic potential $\vec{A}$ are

$$\nabla^2 \vec{A}_{I,III} = 0, \tag{2.15}$$
$$\nabla^2 \vec{A}_{II} = -\mu_0 \nabla \times \vec{M}, \tag{2.16}$$

where μ_0 is the permeability of air and $\vec{M}$ is the magnetization vector. In polar coordinates, the Laplace equation (2.15) and the Poisson equation (2.16) can be written as

$$\begin{aligned} \nabla^2 A_{I\theta} &= \left(\frac{\partial^2 A_{I\theta}}{\partial r^2} + \frac{1}{r}\frac{\partial A_{I\theta}}{\partial r} - \frac{1}{r^2} A_{I\theta} + \frac{\partial^2 A_{I\theta}}{\partial z^2} \right) \vec{\theta} \\ &= \left(-\frac{\partial}{\partial z} B_{Ir} + \frac{\partial}{\partial r} B_{Iz} \right) \vec{\theta} \\ &= 0 \end{aligned} \tag{2.17}$$

$$\begin{aligned} \nabla^2 A_{II\theta} &= \left(\frac{\partial^2 A_{II\theta}}{\partial r^2} + \frac{1}{r}\frac{\partial A_{II\theta}}{\partial r} - \frac{1}{r^2} A_{II\theta} + \frac{\partial^2 A_{II\theta}}{\partial z^2} \right) \vec{\theta} \\ &= \left(-\frac{\partial}{\partial z} B_{IIr} + \frac{\partial}{\partial r} B_{IIz} \right) \vec{\theta} \\ &= -\mu_0 \left(\frac{\partial M_r}{\partial z} - \frac{\partial M_z}{\partial r} \right) \vec{\theta} \end{aligned} \tag{2.18}$$

$$\begin{aligned} \nabla^2 A_{III\theta} &= \left(\frac{\partial^2 A_{III\theta}}{\partial r^2} + \frac{1}{r}\frac{\partial A_{III\theta}}{\partial r} - \frac{1}{r^2} A_{III\theta} + \frac{\partial^2 A_{III\theta}}{\partial z^2} \right) \vec{\theta} \\ &= \left(-\frac{\partial}{\partial z} B_{IIIr} + \frac{\partial}{\partial r} B_{IIIz} \right) \vec{\theta} \\ &= 0. \end{aligned} \tag{2.19}$$

These differential equations are solved by the method of separation of variables. The summation can be disregarded as the differential equations should hold for every n. The solution for $A_{I\theta}$, $A_{II\theta}$ and $A_{III\theta}$ are a Bessel function in the radial, ($\vec{r}$), direction and a sinusoidal

function in the axial, $\vec{z}$, direction.

$$A_{I\theta}(r,z) = \sum_{n=1,2,3,..}^{\infty} \frac{1}{m_n}\Big(a_{1n}\mathcal{B}_{\mathcal{I}1}(m_n r) + b_{1n}\mathcal{B}_{\mathcal{K}1}(m_n r)\Big)\cos(m_n z), \tag{2.20}$$

$$\begin{aligned} A_{II\theta}(r,z) = \sum_{n=1,2,3,..}^{\infty} \frac{1}{m_n}\Big[\Big(\mathcal{K}_{an}(m_n r) + a_{2n}\Big)\mathcal{B}_{\mathcal{I}1}(m_n r) \\ -\Big(\mathcal{K}_{bn}(m_n r) - b_{2n}\Big)\mathcal{B}_{\mathcal{K}1}(m_n r)\Big)\Big]\cos(m_n z). \end{aligned} \tag{2.21}$$

$$A_{III\theta}(r,z) = \sum_{n=1,2,3,..}^{\infty} \frac{1}{m_n}\Big(a_{3n}\mathcal{B}_{\mathcal{I}1}(m_n r) + b_{3n}\mathcal{B}_{\mathcal{K}1}(m_n r)\Big)\cos(m_n z). \tag{2.22}$$

$$\tag{2.23}$$

Where a_{1n},b_{1n}, a_{2n}, and b_{2n} are constants obtained by the boundary conditions, $\mathcal{B}_{\mathcal{I}1}$ and $\mathcal{B}_{\mathcal{K}1}$ are modified Bessel functions of the first and second kind respectively with order 1, and $\mathcal{K}_{an}$ and $\mathcal{K}_{bn}$ are functions which result from substitution of (2.21) into (2.18). m_n is the spatial frequency which contains only odd harmonics and is defined as

$$m_n = \frac{(2n-1)\pi}{\tau_p}. \tag{2.24}$$

According to (2.13) and (2.14) in combination with (2.20) and (2.21), the following solution for B_{Ir}, B_{Iz}, B_{IIr}, B_{IIz}, B_{IIIr}, and B_{IIIz} are obtained:

$$B_{Ir}(r,z) = \sum_{n=1,2,3,..}^{\infty} \Big(a_{1n}\mathcal{B}_{\mathcal{I}1}(m_n r) + b_{1n}\mathcal{B}_{\mathcal{K}1}(m_n r)\Big)\sin(m_n z), \tag{2.25}$$

$$B_{Iz}(r,z) = \sum_{n=1,2,3,..}^{\infty} \Big(a_{1n}\mathcal{B}_{\mathcal{I}0}(m_n r) - b_{1n}\mathcal{B}_{\mathcal{K}0}(m_n r)\Big)\cos(m_n z), \tag{2.26}$$

$$\begin{aligned} B_{IIr}(r,z) = \sum_{n=1,2,3,..}^{\infty} \Big[\Big(\mathcal{K}_{an}(m_n r) + a_{2n}\Big)\mathcal{B}_{\mathcal{I}1}(m_n r) \\ -\Big(\mathcal{K}_{bn}(m_n r) - b_{2n}\Big)\mathcal{B}_{\mathcal{K}1}(m_n r)\Big]\sin(m_n z), \end{aligned} \tag{2.27}$$

$$\begin{aligned} B_{IIz}(r,z) = \sum_{n=1,2,3,..}^{\infty} \Big[\Big(\mathcal{K}_{an}(m_n r) + a_{2n}\Big)\mathcal{B}_{\mathcal{I}0}(m_n r) \\ +\Big(\mathcal{K}_{bn}(m_n r) - b_{2n}\Big)\mathcal{B}_{\mathcal{K}0}(m_n r)\Big]\cos(m_n z), \end{aligned} \tag{2.28}$$

$$B_{IIIr}(r,z) = \sum_{n=1,2,3,..}^{\infty} \Big(a_{3n}\mathcal{B}_{\mathcal{I}1}(m_n r) + b_{3n}\mathcal{B}_{\mathcal{K}1}(m_n r)\Big)\sin(m_n z), \tag{2.29}$$

$$B_{IIIz}(r,z) = \sum_{n=1,2,3,..}^{\infty} \Big(a_{3n}\mathcal{B}_{\mathcal{I}0}(m_n r) - b_{3n}\mathcal{B}_{\mathcal{K}0}(m_n r)\Big)\cos(m_n z). \tag{2.30}$$

$$\tag{2.31}$$

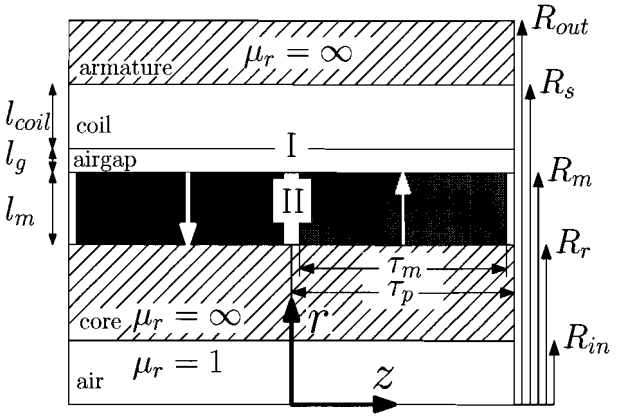

Figure 2.6: Tubular actuator topology with radially magnetized magnets. Region I contains the airgap and the winding area, Region II is the magnet region.

2.1.3 Radially magnetized topology

In the radially magnetized topology shown in Fig. 2.6, the magnets are magnetized in positive and negative radial direction alternatively. Therefore, the magnetization vector $\vec{M}$ is described by a Fourier series of a square wave with only a component in the radial direction [1].

$$\begin{aligned} \vec{M} = M_r \vec{r} &= \sum_{n=1,2,3,..}^{\infty} M_{rn} \sin(m_n z)\, \vec{r}, \\ M_{rn} &= \frac{4B_{rem}}{\mu_0 \tau_p m_n} \sin\left(\frac{m_n \tau_p}{2}\right) \sin\left(\frac{m_n \tau_p \alpha_p}{2}\right). \end{aligned} \tag{2.32}$$

Where τ_p is the pole pitch, and α_p is the magnet to pole pitch ratio $\frac{\tau_m}{\tau_p}$.

Using this magnetization in (2.21) and (2.18) results in the following expressions for $\mathcal{K}_{an}(m_n r)$ and $\mathcal{K}_{bn}(m_n r)$,

$$\mathcal{K}_{an}(m_n r) = -\mu_0 M_{rn} \int_{m_n R_r}^{m_n r} \frac{\mathcal{B}_{\mathcal{K}1}(x)}{\mathcal{B}_{\mathcal{I}1}(x)\mathcal{B}_{\mathcal{K}0}(x) + \mathcal{B}_{\mathcal{K}1}(x)\mathcal{B}_{\mathcal{I}0}(x)} dx, \tag{2.33}$$

$$\mathcal{K}_{bn}(m_n r) = -\mu_0 M_{rn} \int_{m_n R_r}^{m_n r} \frac{\mathcal{B}_{\mathcal{I}1}(x)}{\mathcal{B}_{\mathcal{I}1}(x)\mathcal{B}_{\mathcal{K}0}(x) + \mathcal{B}_{\mathcal{K}1}(x)\mathcal{B}_{\mathcal{I}0}(x)} dx. \tag{2.34}$$

As this topology has a soft-magnetic core, region III is not treated as a region, Therefore, an extra boundary condition at $r = R_r$ is added. The constants a_{1n}, b_{1n}, a_{2n}, and b_{2n} can consequently be derived from the boundary conditions. As there are four unknowns, four independent boundary conditions are necessary to find the solutions. General boundary conditions can be found by evaluating the integral form of the Maxwell equations over control volumes at material interfaces [7]. This results in

1. The tangential component of $\vec{H}$ is continuous if the surface current density at the interface is zero.

2. The normal component of $\vec{B}$ is continuous across an interface.

The iron in the translator and the stator is assumed to be infinitely permeable and eddy-currents in both magnets and iron-parts are neglected. Therefore, the boundary conditions for this problem are

$$B_{Iz}(r,z)\big|_{r=R_s} = 0, \tag{2.35}$$
$$H_{IIz}(r,z)\big|_{r=R_r} = 0, \tag{2.36}$$
$$B_{Ir}(r,z)\big|_{r=R_m} = B_{IIr}(r,z)\big|_{r=R_m}, \tag{2.37}$$
$$H_{Iz}(r,z)\big|_{r=R_m} = H_{IIz}(r,z)\big|_{r=R_m}. \tag{2.38}$$

The boundary conditions must hold for all harmonics, therefore the summations in (2.29) to (2.28) are neglected in the following expressions.

1. Boundary condition (2.35):

$$B_{Iz}(R_s,z) = \Big(a_{1n}\mathcal{B}_{\mathcal{I}0}(m_nR_s) - b_{1n}\mathcal{B}_{\mathcal{K}0}(m_nR_s)\Big)\cos(m_nz) = 0,$$

as the solution must be valid for all z, the $\cos(m_nz)$ term can be eliminated, hence

$$a_{1n}\mathcal{B}_{\mathcal{I}0}(m_nR_s) = b_{1n}\mathcal{B}_{\mathcal{K}0}(m_nR_s),$$

substitution of $\mathcal{B}_{\mathcal{I}0}(m_nR_s)$ by C_{17n}, and $\mathcal{B}_{\mathcal{K}0}(m_nR_s)$ by C_{18n} gives,

$$a_{1n}C_{17n} = b_{1n}C_{18n}. \tag{2.39}$$

2. Boundary condition (2.36):

$$\begin{aligned} H_{IIz}(R_r,z) &= 0, \\ \frac{1}{\mu_0\mu_r}B_{IIz}(R_r,z) &= 0, \\ B_{IIz}(R_r,z) &= \Big[\Big(\mathcal{K}_{an}(m_nR_r) + a_{2n}\Big)\mathcal{B}_{\mathcal{I}0}(m_nR_r) + \\ &\quad \Big(\mathcal{K}_{bn}(m_nR_r) - b_{2n}\Big)\mathcal{B}_{\mathcal{K}0}(m_nR_r)\Big]\cos(m_nz) = 0, \end{aligned}$$

$$\Big(\mathcal{K}_{an}(m_nR_r) + a_{2n}\Big)\mathcal{B}_{\mathcal{I}0}(m_nR_r) + \Big(\mathcal{K}_{bn}(m_nR_r) - b_{2n}\Big)\mathcal{B}_{\mathcal{K}0}(m_nR_r) = 0,$$

where from the definition of $\mathcal{K}_{an}(m_nr)$ and $\mathcal{K}_{bn}(m_nr)$ in (2.33), and (2.34) follows that $\mathcal{K}_{an}(m_nR_r)$ and $\mathcal{K}_{bn}(m_nR_r)$ are zero, which results in

$$a_{2n}\mathcal{B}_{\mathcal{I}0}(m_nR_r) - b_{2n}\mathcal{B}_{\mathcal{K}0}(m_nR_r) = 0,$$

substitution of $\mathcal{B}_{\mathcal{I}0}(m_nR_r)$ by C_{1n}, and $\mathcal{B}_{\mathcal{K}0}(m_nR_r)$ by C_{2n} gives,

$$a_{2n}C_{1n} = b_{2n}C_{2n}. \tag{2.40}$$

3. Boundary condition (2.37):

$$B_{Ir}(R_m, z) = B_{IIr}(R_m, z),$$

$$\Big(a_{1n}\mathcal{B}_{\mathcal{I}1}(m_nR_m) + b_{1n}\mathcal{B}_{\mathcal{K}1}(m_nR_m)\Big)\sin(m_nz) =$$

$$\Big[\Big(\mathcal{K}_{an}(m_nR_m) + a_{2n}\Big)\mathcal{B}_{\mathcal{I}1}(m_nR_m) - \Big(\mathcal{K}_{bn}(m_nR_m) - b_{2n}\Big)\mathcal{B}_{\mathcal{K}1}(m_nR_m)\Big]\sin(m_nz),$$

substitution of $\mathcal{B}_{\mathcal{I}1}(m_nR_m)$ by C_{11n}, and $\mathcal{B}_{\mathcal{K}1}(m_nR_m)$ by C_{12n} gives,

$$a_{1n}C_{11n} + b_{1n}C_{12n} = \Big(\mathcal{K}_{an}(m_nR_m) + a_{2n}\Big)C_{11n} - \Big(\mathcal{K}_{bn}(m_nR_m) - b_{2n}\Big)C_{12n},$$

$$a_{1n}C_{11n} + b_{1n}C_{12n} - a_{2n}C_{11n} - b_{2n}C_{12n} = \mathcal{K}_{an}(m_nR_m)C_{11n} - \mathcal{K}_{bn}(m_nR_m)C_{12n}. \quad (2.41)$$

4. Boundary condition (2.38):

$$\begin{aligned} H_{Iz}(R_m, z) &= H_{IIz}(R_m, z), \\ \frac{1}{\mu_0}B_{Iz}(R_m, z) &= \frac{1}{\mu_0\mu_r}B_{IIz}(R_m, z) - \frac{1}{\mu_r}M_z, \\ \mu_r B_{Iz}(R_m, z) &= B_{IIz}(R_m, z), \end{aligned}$$

$$\mu_r\Big(a_{1n}\mathcal{B}_{\mathcal{I}0}(m_nR_m) - b_{1n}\mathcal{B}_{\mathcal{K}0}(m_nR_m)\Big)\cos(m_nz) =$$

$$\Big[\Big(\mathcal{K}_{an}(m_nR_m) + a_{2n}\Big)\mathcal{B}_{\mathcal{I}0}(m_nR_m) + \Big(\mathcal{K}_{bn}(m_nR_m) - b_{2n}\Big)\mathcal{B}_{\mathcal{K}0}(m_nR_m)\Big]\cos(m_nz),$$

substitution of $\mathcal{B}_{\mathcal{I}0}(m_nR_m)$ by C_{9n}, and $\mathcal{B}_{\mathcal{K}0}(m_nR_m)$ by C_{10n} gives,

$$\mu_r(a_{1n}C_{9n} - b_{1n}C_{10n}) = \Big(\mathcal{K}_{an}(m_nR_m) + a_{2n}\Big)C_{9n} + \Big(\mathcal{K}_{bn}(m_nR_m) - b_{2n}\Big)C_{10n},$$

$$\mu_r a_{1n}C_{9n} - \mu_r b_{1n}C_{10n} - a_{2n}C_{9n} + b_{2n}C_{10n} = \mathcal{K}_{an}(m_nR_m)C_{9n} + \mathcal{K}_{bn}(m_nR_m)C_{10n}. \quad (2.42)$$

The constants a_{1n}, b_{1n}, a_{2n}, and b_{2n} can now be derived from the set of four independent equations. The equations can be rewritten into matrix form

$$\begin{bmatrix} C_{17_N} & -C_{18n} & 0 & 0 \\ 0 & 0 & C_{1n} & -C_{2n} \\ C_{11n} & C_{12n} & -C_{11n} & -C_{12n} \\ \mu_r C_{9n} & -\mu_r C_{10n} & -C_{9n} & C_{10n} \end{bmatrix} \begin{bmatrix} a_{1n} \\ b_{1n} \\ a_{2n} \\ b_{2n} \end{bmatrix} = \begin{bmatrix} 0 \\ 0 \\ C_{11n}\mathcal{K}_{an} - C_{12n}\mathcal{K}_{bn} \\ C_{9n}\mathcal{K}_{an} + C_{10n}\mathcal{K}_{bn} \end{bmatrix}$$

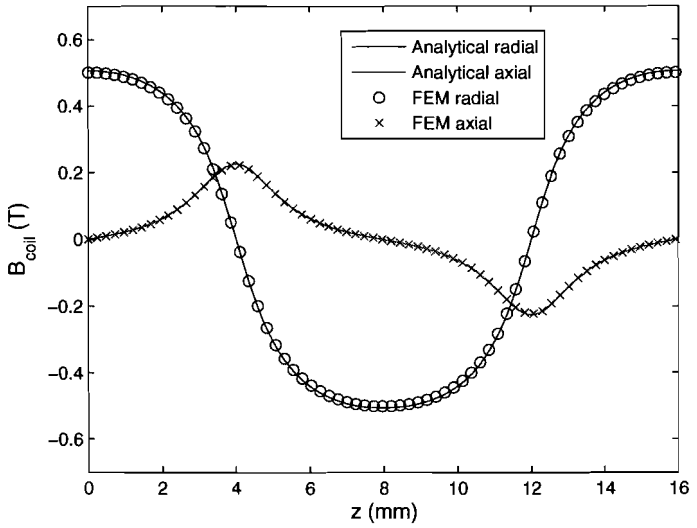

Figure 2.7: Magnetic flux density of the magnets calculated in the middle of the coil ($r = R_s - \frac{l_{coil}}{2}$), where both analytical and FEM results are shown.

This results in

$$a_{1n} = \frac{\left(\frac{C_{11n}}{C_{12n}} + \frac{C_{9n}}{C_{10n}}\right)\left(\frac{C_{1n}}{C_{2n}}\mathcal{K}_{an}(m_n R_m) + \mathcal{K}_{bn}(m_n R_m)\right)}{\left(\frac{C_{1n}}{C_{2n}} - \frac{C_{9n}}{C_{10n}}\right)\left(\frac{C_{17n}}{C_{18n}} + \frac{C_{11n}}{C_{12n}}\right) + \mu_r\left(\frac{C_{9n}}{C_{10n}} - \frac{C_{17n}}{C_{18n}}\right)\left(\frac{C_{1n}}{C_{2n}} + \frac{C_{11n}}{C_{12n}}\right)}, \tag{2.43}$$

$$a_{2n} = \frac{\left(\frac{C_{9n}}{C_{10n}}\mathcal{K}_{an}(m_n R_m) + \mathcal{K}_{bn}(m_n R_m)\right) - \mu_r\left(\frac{C_{9n}}{C_{10n}} - \frac{C_{17n}}{C_{18n}}\right)a_{1n}}{\left(\frac{C_{1n}}{C_{2n}} - \frac{C_{9n}}{C_{10n}}\right)}, \tag{2.44}$$

$$b_{1n} = \frac{C_{17n}}{C_{18n}}a_{1n}, \tag{2.45}$$

$$b_{2n} = \frac{C_{1n}}{C_{2n}}a_{2n}. \tag{2.46}$$

Where the constants C_{in} are given in Appendix B.

These equations are implemented in Matlab to calculate the magnetic field in the coils. The results are compared with FEM and shown in Fig. 2.7. The very small difference between FEM and the semi-analytical results can be explained by the difference in the models. In the semi-analytical model, the axial length is infinite whereas the FEM model has a finite length. In both models, the soft-magnetic parts are infinitely permeable.

2.1.4 Parametric search on the radial topology

In order to find optimal design parameters, a parametric analysis is performed to optimize the magnetic loading. Using the analytical equations found in the previous part, the flux density is calculated for different actuator sizes. For the analysis, the outer radius, R_{out}, is

kept constant and the core radius, R_r has a lower bound as these are final system constraints. To decrease the number of variables, the radial airgap length, l_g, and the radial coil length, l_{coil} are fixed here.

In the first analysis, the effect of varying both the pole pitch, τ_p, and the radial magnet length, l_m, on the flux density in the coil are analyzed. The radial length of the stator is fixed, therefore the core radius, R_r, changes when the radial magnet length, l_m, changes. The dimensions of the actuator in this analysis are shown in Table 2.2.

Table 2.2: Fixed parameters in analysis

R_{out} (mm)	9.00
l_{stator} (mm)	1.00
l_{coil} (mm)	1.45
l_g (mm)	0.25
R_r (mm)	$\geq$2.00
α_p	1.00

Fig. 2.8a shows the peak value of the the magnetic flux density in the middle of the coil for several values of pole pitch and magnet length and Fig. 2.8b shows the RMS value of the magnetic flux density in that analysis. As can be seen from the figures, a larger pole pitch, τ_p, results in a higher flux density. For the radial magnet length, l_m, an optimum exists at approximately 2.6 mm.

Although a larger pole pitch results in a higher flux density, it has a major drawback. As visualized in Fig. 2.9, almost all the flux from one magnet has to flow through the stator and the core. Therefore, increasing τ_p will increase the flux density in the stator and the core causing saturation of the iron. To show this effect, the peak flux density in the core and the stator are estimated and plotted in Fig. 2.8c and Fig. 2.8d. Increasing the radial length of the magnet causes a further increase of the flux density in the core, because the core radius R_r decreases with increasing magnet length.

Note that these flux densities are calculated for linear iron with an infinite permeability. In reality, the iron starts to saturate for flux density values of approximately 1.3 T. Therefore, this model provides only useful information when the estimated flux density in the core and the stator are below 1.3 T.

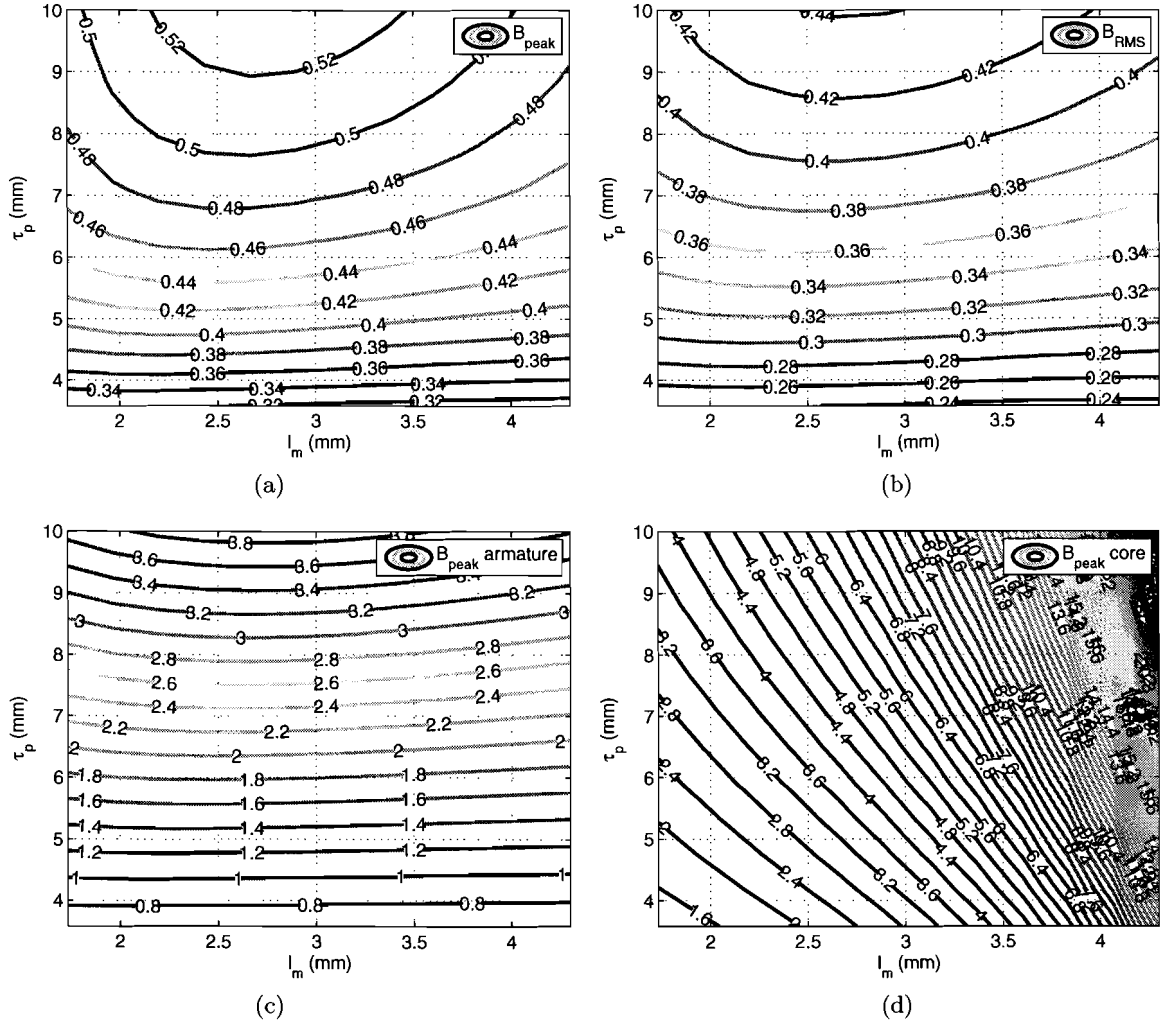

Figure 2.8: Magnetic flux density versus pole pitch τ_p and radial magnet length l_m.(a) and (b) show the peak value and the RMS value of flux density in the middle of the coil respectively, (c) shows the peak flux density in the armature and (d) shows the peak flux density in the core

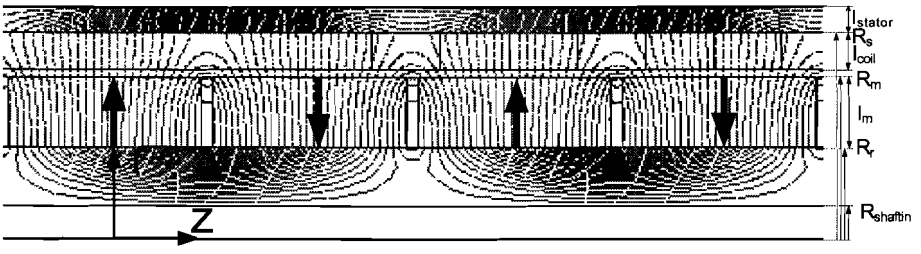

Figure 2.9: Equipotential lines in the tubular actuator with radial magnetized magnets.

Conclusion

Fig. 2.8d shows that only a geometry with $\tau_p \leq 4.5mm$ and $l_m \leq 2.0mm$ results in a design with a low level of saturation in the core. As this geometry provides a relatively low flux

density in the coil, the radial magnetized tubular actuator is not favorable in this application. In order to decrease the flux density in the core, a topology with a Halbach magnet array is proposed in the next section.

2.1.5 Quasi-Halbach magnetized topology with soft-magnetic core

To minimize the flux density in the core, a Halbach magnet array is proposed. A Halbach magnet array concentrates the flux at one side of the magnets and provides a more sinusoidal flux density. [5], [2] The magnets in a Halbach array are sinusoidally magnetized. Since, in practice, it is relatively difficult to manufacture magnets with an ideal Halbach magnetization, a simpler form, referred to as quasi-Halbach, is used here. Instead of one magnet with sinusoidal magnetization, a two-segmented magnet array is used. The magnetization is shown in Fig. 2.10 and can be expressed as a Fourier series in the radial ($\vec{r}$), and a Fourier series in the axial ($\vec{z}$) direction. [6]

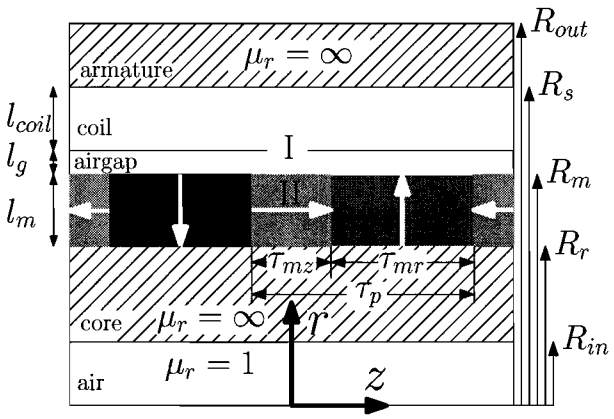

Figure 2.10: Tubular actuator topology with a quasi-Halbach magnetized magnet array with a magnetic core. Region I contains the airgap and the winding area, Region II is the magnet region.

In this section, the same approach as in the previous section is used to calculate the magnetic field in a tubular actuator with a quasi-Halbach magnet array as shown in Fig. 2.10. The resulting magnetization vector is

$$\vec{M} = M_r\vec{r} + M_z\vec{z} = \sum_{n=1,2,3,..}^{\infty} M_{rn}\sin(m_n z)\,\vec{r} + \sum_{n=1,2,3,..}^{\infty} M_{zn}\cos(m_n z)\,\vec{z},$$

$$M_{rn} = \frac{4B_{rem}}{\mu_0\tau_p m_n}\sin\left(\frac{m_n\tau_p}{2}\right)\sin\left(\frac{m_n\tau_p\alpha_p}{2}\right), \tag{2.47}$$

$$M_{zn} = \frac{4B_{rem}}{\mu_0\tau_p m_n}\sin\left(\frac{m_n(1-\alpha_p)\tau_p}{2}\right), \tag{2.48}$$

where τ_p is the pole pitch, and α_p is the radially magnetized magnet pitch to pole pitch ratio $(\frac{\tau_{mr}}{\tau_p})$.

The general solution presented in section 2.1.2 is still valid as only the magnetization vector is changed. The boundary conditions for this problem are the same as for the radially

magnetized topology

$$B_{Iz}(r,z)\big|_{r=R_s} = 0, \tag{2.49}$$
$$H_{IIz}(r,z)\big|_{r=R_r} = 0, \tag{2.50}$$
$$B_{Ir}(r,z)\big|_{r=R_m} = B_{IIr}(r,z)\big|_{r=R_m}, \tag{2.51}$$
$$H_{Iz}(r,z)\big|_{r=R_m} = H_{IIz}(r,z)\big|_{r=R_m}. \tag{2.52}$$

To find a_{1n}, a_{2n}, b_{1n} and b_{2n} in the expressions for the magnetic field, (2.29) to (2.28), the boundary conditions have to be solved. As the boundary conditions must hold for all harmonics, the summations in (2.49) to (2.52) are neglected in the following expressions.

1. Boundary condition (2.49):
   The derivation of this equation is the same as in (2.39).

2. Boundary condition (2.50):
   As the magnetization has a z-component, the equation here is slightly different than (2.40)

$$H_{IIz}(R_r,z) = 0$$
$$\frac{1}{\mu_0\mu_r}B_{IIz}(R_r,z) - \frac{1}{\mu_r}M_z = 0$$

$$\frac{1}{\mu_0\mu_r}\left[\Big(\mathcal{K}_{an}(m_nR_r)+a_{2n}\Big)\mathcal{B}_{\mathcal{I}0}(m_nR_r)+\Big(\mathcal{K}_{bn}(m_nR_r)-b_{2n}\Big)\mathcal{B}_{\mathcal{K}0}(m_nR_r)\right]\cos(m_nz) = \frac{1}{\mu_r}M_{zn}\cos(m_nz),$$

   where from the definition of $\mathcal{K}_{an}(m_nr)$ and $\mathcal{K}_{bn}(m_nr)$ in (2.33), and (2.34) follows that $\mathcal{K}_{an}(m_nR_r)$ and $\mathcal{K}_{bn}(m_nR_r)$ are zero, which result in

$$\frac{1}{\mu_0\mu_r}\Big(a_{2n}\mathcal{B}_{\mathcal{I}0}(m_nR_r) - b_{2n}\mathcal{B}_{\mathcal{K}0}(m_nR_r)\Big) = \frac{1}{\mu_r}M_{zn},$$

   substitution of $\mathcal{B}_{\mathcal{I}0}(m_nR_r)$ by C_{1n}, and $\mathcal{B}_{\mathcal{K}0}(m_nR_r)$ by C_{2n} gives,

$$a_{2n}C_{1n} - b_{2n}C_{2n} = \mu_0M_{zn}. \tag{2.53}$$

3. Boundary condition (2.51):
   The derivation of this equation is the same as in (2.41).

4. Boundary condition (2.52):
   As the magnetization has a z-component, the equation here is slightly different than (2.42)

$$H_{Iz}(R_m,z) = H_{IIz}(R_m,z),$$

$$\frac{1}{\mu_0}B_{Iz}(R_m,z) = \frac{1}{\mu_0\mu_r}B_{IIz}(R_m,z) - \frac{1}{\mu_r}M_z,$$

$$\mu_rB_{Iz}(R_m,z) = B_{IIz}(R_m,z) - \mu_0M_z,$$

$$\mu_r\Big(a_{1n}\mathcal{B}_{\mathcal{I}0}(m_nR_m) - b_{1n}\mathcal{B}_{\mathcal{K}0}(m_nR_m)\Big)\cos(m_nz) =$$

$$\Big[\Big(\mathcal{K}_{an}(m_nR_m) + a_{2n}\Big)\mathcal{B}_{\mathcal{I}0}(m_nR_m) + \Big(\mathcal{K}_{bn}(m_nR_m) - b_{2n}\Big)\mathcal{B}_{\mathcal{K}0}(m_nR_m)\Big]\cos(m_nz) -$$

$$\mu_0 M_{zn}\cos(m_nz),$$

substitution of $\mathcal{B}_{\mathcal{I}0}(m_nR_m)$ by C_{9n}, and $\mathcal{B}_{\mathcal{K}0}(m_nR_m)$ by C_{10n} gives,

$$\mu_r(a_{1n}C_{9n} - b_{1n}C_{10n}) = \Big(\mathcal{K}_{an}(m_nR_m) + a_{2n}\Big)C_{9n} + \Big(\mathcal{K}_{bn}(m_nR_m) - b_{2n}\Big)C_{10n} - \mu_0 M_{zn},$$

$$\mu_r a_{1n}C_{9n} - \mu_r b_{1n}C_{10n} - a_{2n}C_{9n} + b_{2n}C_{10n} = \mathcal{K}_{an}(m_nR_m)C_{9n} + \mathcal{K}_{bn}(m_nR_m)C_{10n} - \mu_0 M_{zn}. \tag{2.54}$$

The constants a_{1n}, b_{2n}, a_{2n}, and b_{2n} can now be derived from the set of four independent equations. This results in the following matrix

$$\begin{bmatrix} C_{17_N} & -C_{18n} & 0 & 0 \\ 0 & 0 & C_{1n} & -C_{2n} \\ C_{11n} & C_{12n} & -C_{11n} & -C_{12n} \\ \mu_r C_{9n} & -\mu_r C_{10n} & -C_{9n} & C_{10n} \end{bmatrix} \begin{bmatrix} a_{1n} \\ b_{1n} \\ a_{2n} \\ b_{2n} \end{bmatrix} = \begin{bmatrix} 0 \\ \mu_0 M_{zn} \\ C_{11n}\mathcal{K}_{an} - C_{12n}\mathcal{K}_{bn} \\ C_{9n}\mathcal{K}_{an} + C_{10n}\mathcal{K}_{bn} - \mu_0 M_{zn} \end{bmatrix}$$

This results in

$$a_{1n} = \frac{\left(\frac{C_{11n}}{C_{12n}} + \frac{C_{9n}}{C_{10n}}\right)\left(\frac{C_{1n}}{C_{2n}}\mathcal{K}_{an}(m_nR_m) + \mathcal{K}_{bn}(m_nR_m)\right)}{\left(\frac{C_{1n}}{C_{2n}} - \frac{C_{9n}}{C_{10n}}\right)\left(\frac{C_{17n}}{C_{18n}} + \frac{C_{11n}}{C_{12n}}\right) + \mu_r\left(\frac{C_{9n}}{C_{10n}} - \frac{C_{17n}}{C_{18n}}\right)\left(\frac{C_{1n}}{C_{2n}} + \frac{C_{11n}}{C_{12n}}\right)} + \frac{\frac{\mu_0 M_{zn}}{C_{10n}}\left(\frac{C_{9n}}{C_{2n}} - \frac{C_{1n}}{C_{2n}}\right) + \frac{\mu_0 M_{zn}}{C_{12n}}\left(\frac{C_{11n}}{C_{2n}} - \frac{C_{11n}}{C_{10n}}\right)}{\left(\frac{C_{1n}}{C_{2n}} - \frac{C_{9n}}{C_{10n}}\right)\left(\frac{C_{17n}}{C_{18n}} + \frac{C_{11n}}{C_{12n}}\right) + \mu_r\left(\frac{C_{9n}}{C_{10n}} - \frac{C_{17n}}{C_{18n}}\right)\left(\frac{C_{1n}}{C_{2n}} + \frac{C_{11n}}{C_{12n}}\right)}, \tag{2.55}$$

$$a_{2n} = \frac{\frac{C_{9n}}{C_{10n}}\mathcal{K}_{an}(m_nR_m) + \mathcal{K}_{bn}(m_nR_m) + M_{zn}\left(\frac{\mu_0}{C_{2n}} - \frac{\mu_0}{C_{10n}}\right) - \mu_r\left(\frac{C_{9n}}{C_{10n}} - \frac{C_{17n}}{C_{18n}}\right)a_{1n}}{\left(\frac{C_{1n}}{C_{2n}} - \frac{C_{9n}}{C_{10n}}\right)} \tag{2.56}$$

$$b_{1n} = \frac{C_{17n}}{c_{18n}}a_{1n}, \tag{2.57}$$

$$b_{2n} = \frac{C_{1n}a_{2n} - \mu_0 M_{zn}}{C_{2n}}. \tag{2.58}$$

Where the constants C_{in} are given in Appendix B.

These equations are implemented in Matlab to calculate the magnetic field in the coils. The results are compared with FEM and shown in Fig. 2.11 for $\alpha_p = 0.65$. The very small difference between FEM and the semi-analytical results can be explained by the difference in the models. In the semi-analytical model, the axial length is infinite whereas the FEM model has a finite length. In both models, the soft-magnetic parts are infinitely permeable.

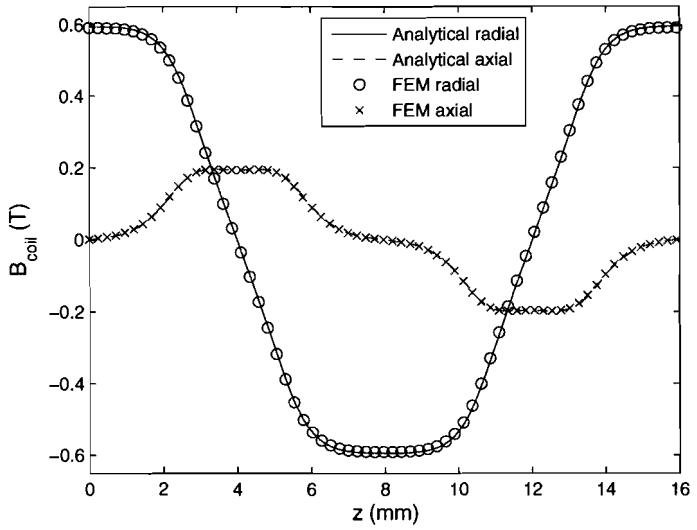

Figure 2.11: Magnetic flux density of the magnets calculated in the middle of the coil ($r = R_s - \frac{l_{coil}}{2}$) with a quasi-Halbach magnet array for $\alpha_p = 0.65$ with a soft-magnetic core. Both analytical and FEM results are shown.

2.1.6 Parametric search on the quasi-Halbach topology

In order to find optimal design parameters, a parametric analysis is performed to optimize the magnetic loading. The same approach as presented in the previous section for the radial magnetized topology is used here. The outer radius, R_{out}, is kept constant and the core radius, R_r has a lower bound. To decrease the number of variables, the radial airgap length, l_g, and the radial coil length, l_{coil} are fixed.

In the first analysis, the effect of both the pole pitch, τ_p, and the relation between τ_{mr} and τ_{mz} on the flux density in the coil are analyzed. The magnet length is fixed. The dimensions of the actuator in this analysis are shown in Table 2.3.

Table 2.3: Fixed parameters in analysis

R_{out} (mm)	9.00
l_{stator} (mm)	1.00
l_{coil} (mm)	1.45
l_g (mm)	0.25
l_m (mm)	3.00

Fig. 2.12a and Fig. 2.12b show the peak value of the fundamental and the RMS value of the flux density in the coil respectively. Both figures show that the highest flux density is achieved for $\alpha_p \approx 0.8$. Increasing the pole pitch, τ_p, results in a higher flux density. As for the radial magnetized topology, increasing pole pitch results in a higher flux density in the stator as well. In Fig. 2.13 is shown how the flux flows through the actuator.

To show the effects on the flux density in the stator, Fig. 2.12d depicts an estimation of the flux density in the stator. As can be seen, the flux density rises very quick above 1.3 T and

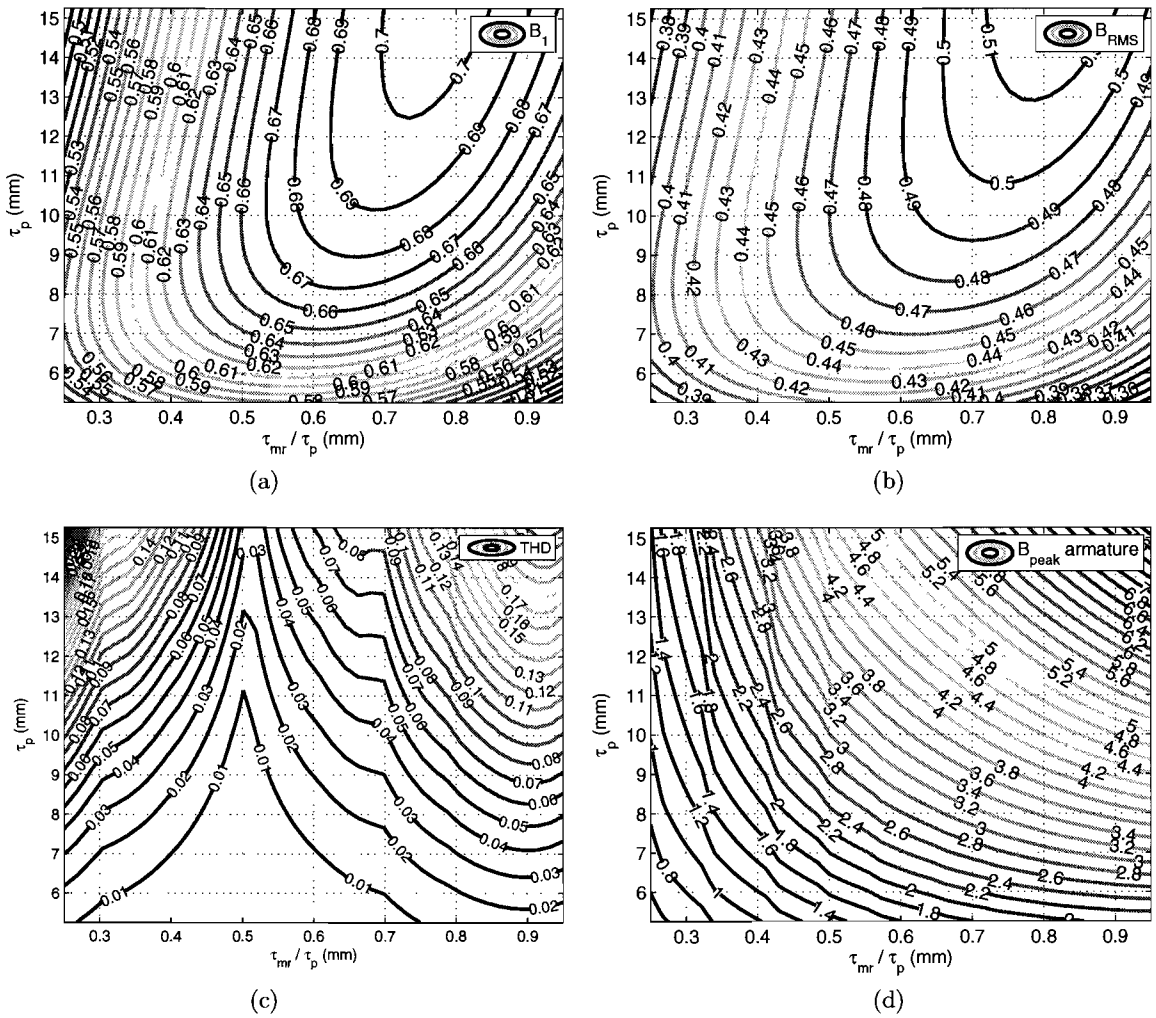

Figure 2.12: Magnetic flux density versus pole pitch τ_p and radially magnetized magnet pitch τ_{mr} to pole pitch τ_p ratio.(a) and (b) show the flux density in the middle of the coil, (c) shows the total harmonic distortion of the flux density in the middle of the coil and (d) shows the peak flux density in the armature.

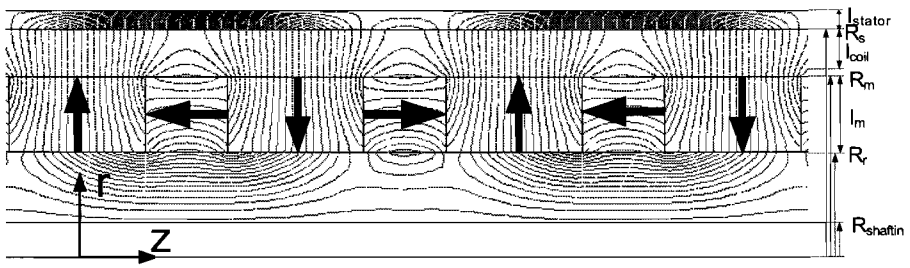

Figure 2.13: Equipotential lines in the tubular actuator with a quasi-Halbach magnet array with a soft-magnetic core.

causes saturation. Instead of for the radial magnetized topology, the radial stator length can be extended here because the flux density in the core is lower due to the flux concentration effect of the Halbach array.

In theory, a Halbach magnet array produces a sinusoidal flux density. In order to minimize the force ripple it is possible to design the quasi-Halbach array for sinusoidal flux density. In Fig. 2.12c, the total harmonic distortion is shown. For $\alpha_p = 0.5$ the total harmonic distortion is at its minimum.

A second analysis is performed to analyze the effect of changing the radial magnet length on the flux density level in the coil. The dimensions of the actuator in this analysis are shown in Table 2.4. Due to the geometric constraints $l_m \leq 4.3$ mm in the analysis. In Fig. 2.14a

Table 2.4: Fixed parameters in analysis

R_{out} (mm)	9.00
l_{stator} (mm)	1.00
l_{coil} (mm)	1.45
l_g (mm)	0.25
α_p	0.75

and Fig. 2.14b the results of the analysis are shown. Both the peak value of the fundamental and the RMS value of the flux density increases when the radial length of the magnet and the pole pitch are enlarged.

As can be seen in Fig. 2.14d, the flux density in the stator rises when the pole pitch and the magnet length increases. To prevent saturation of the armature, the flux density should be below 1.3 T. This implies that as long as $\tau_p < 6$ mm, the armature will not saturate. When a larger pole pitch is favorable, it is possible to prevent saturation by extending the radial stator length. The flux density in the stator will decrease linearly with the radial length of the stator. This implies that for $l_{stator} = 1.5$ mm, the highest possible RMS value of the flux density is now 0.74 T where for $l_{stator} = 1.0$ mm, the maximum RMS value was 0.64 T. An increase of 15 % is realized.

Fig. 2.14c shows that the influence of l_m on the total harmonic distortion of the flux density is minimal for small τ_p. The distortion increases when the pole pitch is enlarged especially for small magnet length.

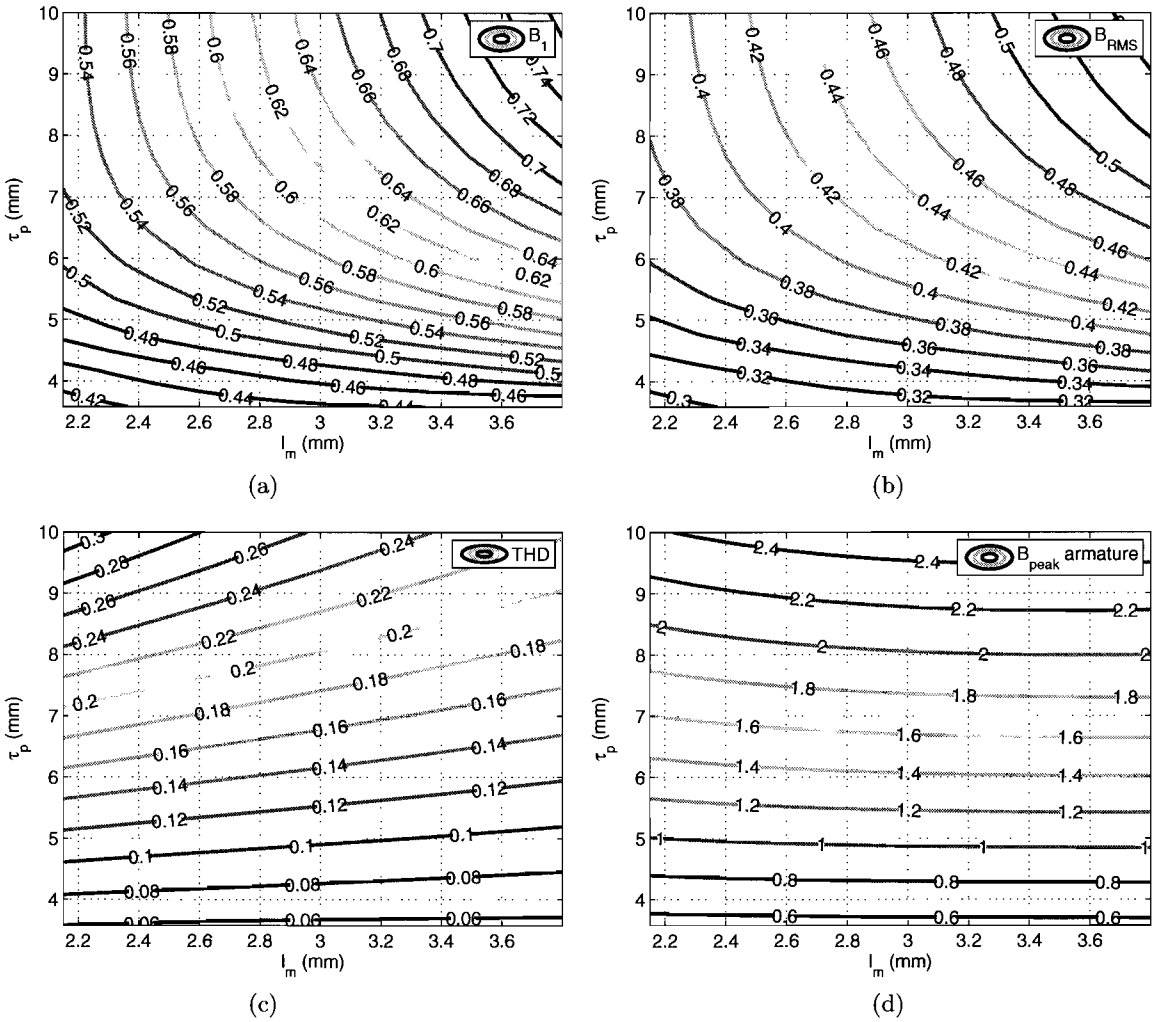

Figure 2.14: Magnetic flux density versus pole pitch τ_p and radial magnet length l_m.(a) and (b) show the flux density in the middle of the coil, (c) shows the total harmonic distortion of the flux density in the coil and (d) shows the peak flux density in the armature.

2.1.7 Quasi-Halbach magnetized topology with non-magnetic core

In the previous section, a quasi-Halbach magnet array is introduced to minimize the flux density in the core. Due to the self-shielding property of the Halbach magnet array, the soft-magnetic core can be replaced by a non-magnetic core. This implies that the iron core can be replaced by a aluminium core or no core at all, which will decrease the mass of the translator. As the z-actuator has to operate at high acceleration, the mass of the mover is a very important quantity.

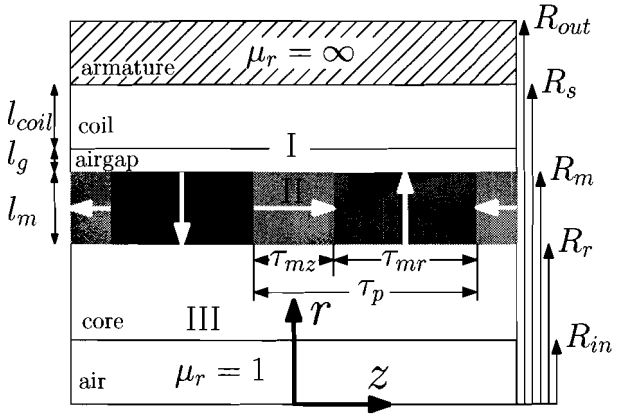

Figure 2.15: Tubular actuator topology with a quasi-Halbach magnetized magnet array with a non-magnetic core. Region I contains the airgap and the winding area, Region II is the magnet region and Region III is the non-magnetic core region.

In this section, the magnetic field equations are solved for a topology with a quasi-Halbach magnet array and a non-magnetic core. The problem is similar to the problem with a magnetic core however the third region has to be considered here, see Fig. 2.15. This source free region III contains the core and is modeled to be source-free.

The magnetization is the same as for the topology with a soft-magnetic core and can be expressed as a Fourier series in the radial ($\vec{r}$), and a Fourier series in the axial ($\vec{z}$) direction.

The resulting magnetization vector is

$$\vec{M} = M_r\vec{r} + M_z\vec{z} = \sum_{n=1,2,3,..}^{\infty} M_{rn}\sin(m_n z)\,\vec{r} + \sum_{n=1,2,3,..}^{\infty} M_{zn}\cos(m_n z)\,\vec{z},$$

$$M_{rn} = \frac{4B_{rem}}{\mu_0\tau_p m_n}\sin\left(\frac{m_n\tau_p}{2}\right)\sin\left(\frac{m_n\tau_p\alpha_p}{2}\right), \tag{2.59}$$

$$M_{zn} = \frac{4B_{rem}}{\mu_0\tau_p m_n}\sin\left(\frac{m_n(1-\alpha_p)\tau_p}{2}\right), \tag{2.60}$$

where τ_p is the pole pitch, and α_p is the radially magnetized magnet pitch to pole pitch ratio $(\frac{\tau_{mr}}{\tau_p})$.

To solve the magnetic field equations with the six variables a_{1n}, a_{2n}, a_{3n}, b_{1n}, b_{2n}, b_{3n}, six

boundary conditions are stated and solved.

$$B_{Iz}(r,z)\big|_{r=R_s} = 0, \tag{2.61}$$
$$A_{III\theta}(r,z)\big|_{r=0} = 0, \tag{2.62}$$
$$B_{Ir}(r,z)\big|_{r=R_m} = B_{IIr}(r,z)\big|_{r=R_m}, \tag{2.63}$$
$$B_{IIr}(r,z)\big|_{r=R_r} = B_{IIIr}(r,z)\big|_{r=R_r}, \tag{2.64}$$
$$H_{Iz}(r,z)\big|_{r=R_m} = H_{IIz}(r,z)\big|_{r=R_m}, \tag{2.65}$$
$$H_{IIz}(r,z)\big|_{r=R_r} = H_{IIIz}(r,z)\big|_{r=R_r}. \tag{2.66}$$

As the boundary conditions must hold for all harmonics, the summations in (2.49) to (2.52) are neglected in the following expressions.

1. Boundary condition (2.61):
   The derivation of this equation is the same as in (2.39).

2. Boundary condition (2.62):

$$A_{III\theta}(0,z) = \frac{1}{m_n}\Big(a_{3n}\mathcal{B}_{\mathcal{I}1}(0) + b_{3n}\mathcal{B}_{\mathcal{K}1}(0)\Big)\cos(m_n z) = 0,$$

   Since $\mathcal{B}_{\mathcal{I}1}(0) = 0$ and $\mathcal{B}_{\mathcal{K}1}(0) = \infty$,

$$b_{3n} = 0. \tag{2.67}$$

3. Boundary condition (2.63):
   The derivation of this equation is the same as in (2.41).

4. Boundary condition

$$B_{IIr}(R_r,z) = B_{IIIr}(R_r,z),$$

$$\Big[\Big(\mathcal{K}_{an}(m_nR_r) + a_{2n}\Big)\mathcal{B}_{\mathcal{I}1}(m_nR_r) - \Big(\mathcal{K}_{bn}(m_nR_r) - b_{2n}\Big)\mathcal{B}_{\mathcal{K}1}(m_nR_r)\Big]\sin(m_nz) =$$

$$a_{3n}\mathcal{B}_{\mathcal{I}1}(m_nR_r)\sin(m_nz),$$

   where from the definition of $\mathcal{K}_{an}(m_nr)$ and $\mathcal{K}_{bn}(m_nr)$ in (2.33), and (2.34) follows that $\mathcal{K}_{an}(m_nR_r)$ and $\mathcal{K}_{bn}(m_nR_r)$ are zero. Substitution of $\mathcal{B}_{\mathcal{I}1}(m_nR_r)$ by C_{3n}, and $\mathcal{B}_{\mathcal{K}1}(m_nR_r)$ by C_{4n} gives,

$$a_{2n}C_{3n} + b_{2n}C_{4n} - a_{3n}C_{3n} = 0,$$

5. Boundary condition (2.66):
   The derivation of this equation is the same as in (2.54).

6. Boundary condition (2.66):

$$H_{IIz}(R_r,z) = H_{IIIz}(R_r,z),$$

$$\frac{1}{\mu_0\mu_r}B_{IIz}(R_r,z) - \frac{1}{\mu_r}M_z = \frac{1}{\mu_0}B_{IIIz}(R_r,z),$$

$$B_{IIz}(R_r,z) - \mu_0 M_z = \mu_r B_{IIIz}(R_r,z),$$

$$\left[\Big(\mathcal{K}_{an}(m_nR_r)+a_{2n}\Big)\mathcal{B}_{\mathcal{I}0}(m_nR_r)+\Big(\mathcal{K}_{bn}(m_nR_r)-b_{2n}\Big)\mathcal{B}_{\mathcal{K}0}(m_nR_r)\right]\cos(m_nz)-$$

$$\mu_0 M_{zn}\cos(m_nz)=\mu_r a_{3n}\mathcal{B}_{\mathcal{I}0}(m_nR_r)\cos(m_nz),$$

where from the definition of $\mathcal{K}_{an}(m_nr)$ and $\mathcal{K}_{bn}(m_nr)$ in (2.33), and (2.34) follows that $\mathcal{K}_{an}(m_nR_r)$ and $\mathcal{K}_{bn}(m_nR_r)$ are zero. Substitution of $\mathcal{B}_{\mathcal{I}0}(m_nR_r)$ by C_{1n}, and $\mathcal{B}_{\mathcal{K}0}(m_nR_r)$ by C_{2n} gives,

$$a_{2n}C_{1n}-b_{2n}C_{2n}-\mu_r a_{3n}C_{1n}=\mu_0 M_{zn}.$$

The constants a_{1n}, a_{2n}, a_{3n}, b_{1n}, b_{2n} and b_{3n} can now be derived from the set of six independent equations formulated. The solutions are found by solving the equations using Mathematica. The equations in matrix form are given here.

$$\begin{bmatrix} C_{17n} & -C_{18n} & 0 & 0 & 0 & 0\\ 0 & 0 & 0 & 0 & 0 & 1\\ C_{11n} & C_{12n} & -C_{11n} & -C_{12n} & 0 & 0\\ 0 & 0 & C_{3n} & C_{4n} & -C_{3n} & 0\\ \mu_r C_{9n} & -\mu_r C_{10n} & -C_{9n} & C_{10n} & 0 & 0\\ 0 & 0 & C_{1n} & -C_{2n} & -\mu_r C_{1n} & 0 \end{bmatrix} \begin{bmatrix} a_{1n}\\ b_{1n}\\ a_{2n}\\ b_{2n}\\ a_{3n}\\ b_{3n} \end{bmatrix} =$$

$$\begin{bmatrix} 0\\ 0\\ K_{an}(m_nR_m)C_{11n}-K_{bn}(m_nR_m)C_{12n}\\ 0\\ K_{an}(m_nR_m)C_{9n}+K_{bn}(m_nR_m)C_{10n}-\mu_0 M_{zn}\\ \mu_0 M_{zn} \end{bmatrix} \tag{2.68}$$

Where the constants C_{in} are given in Appendix B.

The field equations are implemented in Matlab to calculate the magnetic field in the coils. The results are compared with FEM and shown in Fig. 2.7 for $\alpha_p = 0.65$. The very small difference between FEM and the semi-analytical results can be explained by the difference in the models. In the semi-analytical model, the axial length is infinite whereas the FEM model has a finite length. In both models, the iron parts are infinitely permeable.

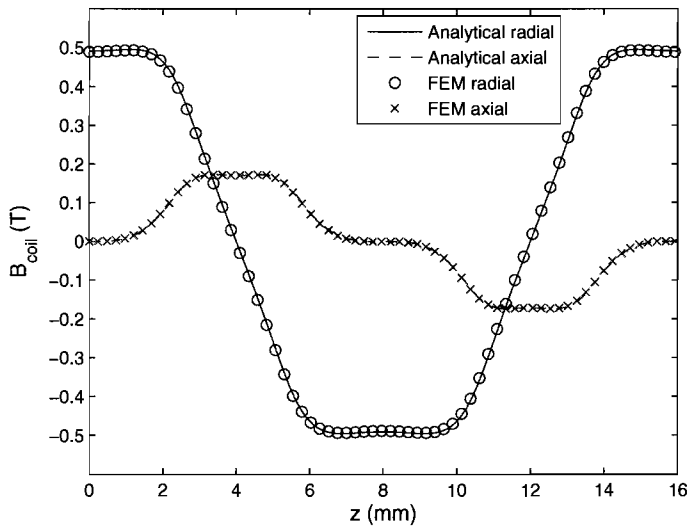

Figure 2.16: Magnetic flux density of the magnets calculated in the middle of the coil ($r = R_s - \frac{l_{coil}}{2}$) with a quasi-Halbach magnet array for $\alpha_p = 0.65$ with a non-magnetic core. Both analytical and FEM results are shown.

2.1.8 Parametric search on the quasi-Halbach topology with non-magnetic core

The same approach as presented in the previous section for the quasi-Halbach magnet array with magnetic core is used here. The outer radius, R_{out}, is kept constant and the core radius, R_r has a lower bound. To decrease the number of variables, the radial airgap length, l_g, and the radial coil length, l_{coil} are fixed.

In the first analysis, the effect of both the pole pitch, τ_p, and the magnet pitch to pole pitch ratio, α_p on the flux density in the coil are analyzed. The radial magnet length is fixed. The dimensions of the actuator in this analysis are shown in Table 2.7.

Table 2.5: Fixed parameters in analysis

R_{out} (mm)	9.00
l_{stator} (mm)	1.00
l_{coil} (mm)	1.45
l_g (mm)	0.25
l_m (mm)	4.30

Fig. 2.17a and Fig. 2.17b show the peak value of the fundamental and the RMS value of the flux density in the coil respectively. Both figures show that the highest flux density is achieved for $\alpha_p = 0.4$. The optimum for the pole pitch, τ_p, is found around 8 mm. This is in contrast to the topology with a magnetic core. In Fig. 2.18 is shown how the flux flows through the actuator. As can be seen, almost all the flux is concentrated in the airgap.

In Fig. 2.17d the flux density in the stator is shown. Since the optimum of the flux density in the coil is found for $\tau_p \approx 8$mm and $\alpha_p \approx 0.4$, no saturation will occur when the optimal

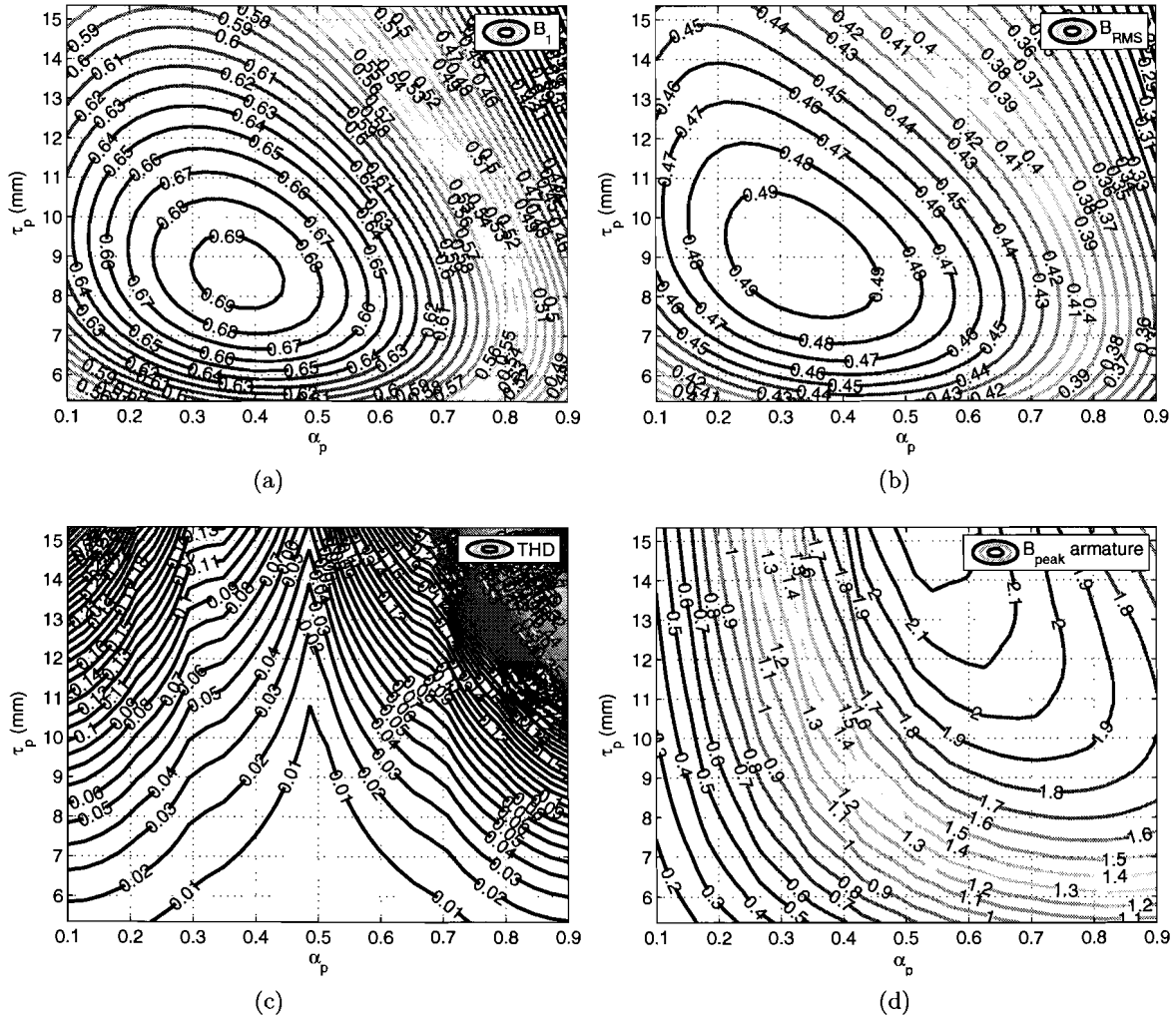

Figure 2.17: Magnetic flux density versus pole pitch τ_p and radially magnetized magnet pitch τ_{mr} to pole pitch τ_p ratio,α_p.(a) and (b) show the flux density in the middle of the coil, (c) shows the total harmonic distortion of the flux density in the middle of the coil and (d) shows the peak flux density in the armature.

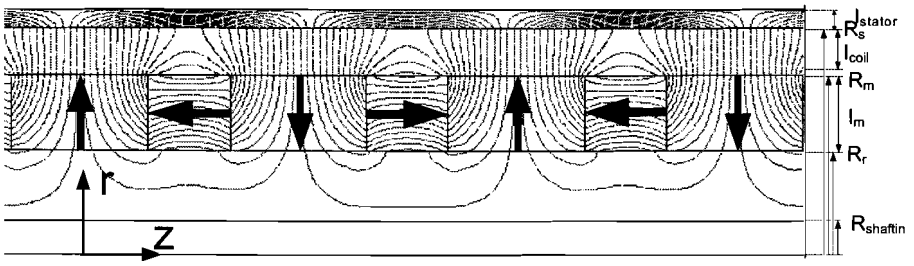

Figure 2.18: Equipotential lines in the tubular actuator with a quasi-Halbach magnet array and a non-magnetic core.

geometry is used with $l_{stator} \geq 1.00$mm.

In theory, a Halbach magnet array produces a sinusoidal flux density. In order to minimize the force ripple it is possible to design the quasi-Halbach array for sinusoidal flux density. In Fig. 2.17c, the total harmonic distortion is shown. For $\alpha_p = 0.5$, the total harmonic distortion is at its minimum.

A second analysis is performed to analyze the effect of changing the radial magnet length on the flux density level in the coil. The dimensions of the actuator in this analysis are shown in Table 2.6. Due to the geometric constraints $l_m \leq 4.3$ mm in the analysis. In Fig. 2.19a and

Table 2.6: Fixed parameters in analysis

R_{out} (mm)	9.00
l_{stator} (mm)	1.00
l_{coil} (mm)	1.45
l_g (mm)	0.25
α_p	0.50

Fig. 2.19b the results of the analysis are shown. Both the fundamental and the RMS value of the flux density increases when the radial length of the magnet is enlarged. The optimal pole pitch, τ_p, is approximately 7 mm for $l_m = 2.4$ mm and 8mm for $l_m = 2.4$ mm.

As can be seen in Fig. 2.19d, the flux density in the stator rises when the pole pitch and the magnet length increases. Fig. 2.19c shows that the influence of l_m on the total harmonic distortion of the flux density is minimal in contrary to the influence of the pole pitch, increasing the pole pitch results in more distortion.

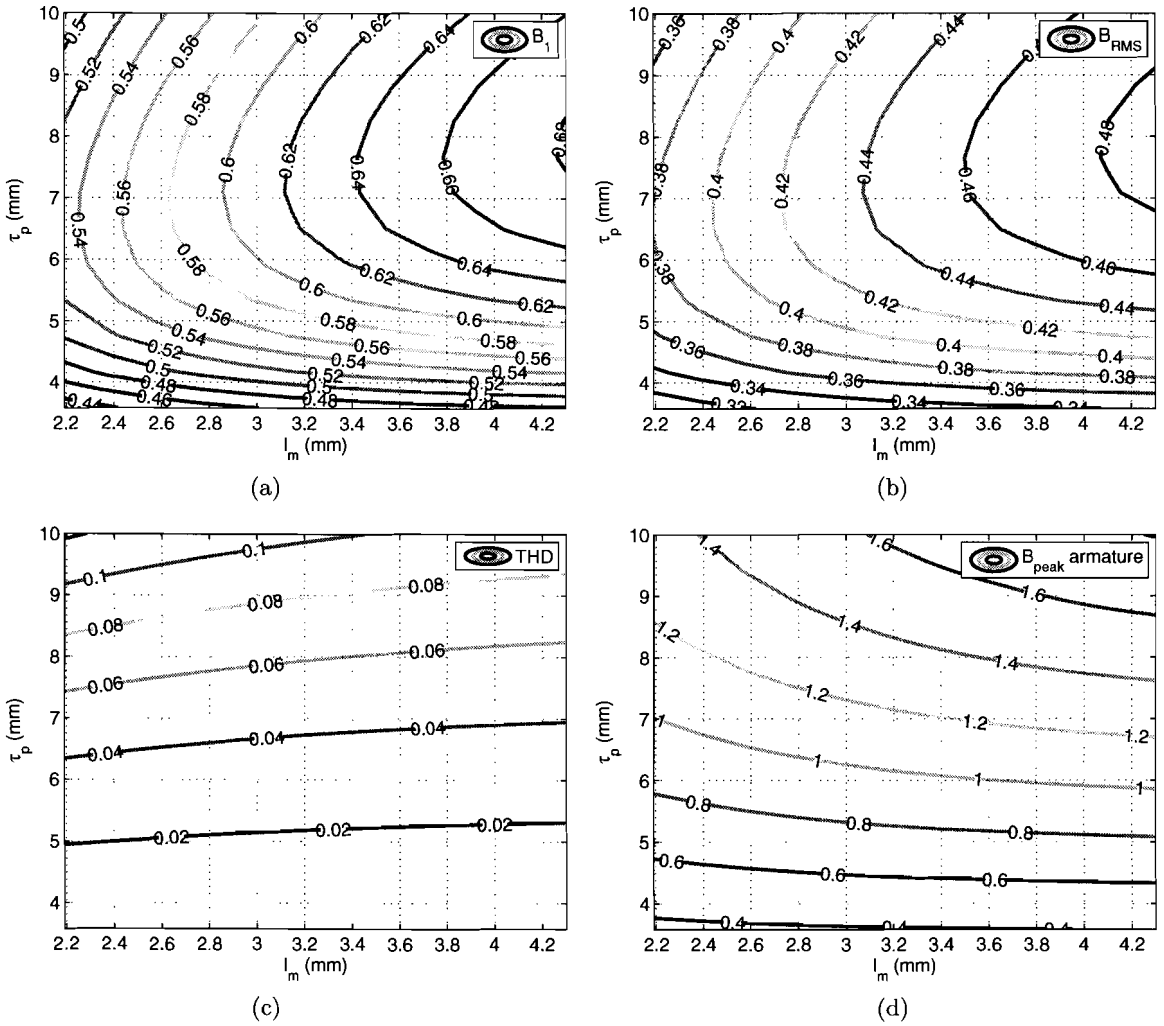

Figure 2.19: Magnetic flux density versus pole pitch τ_p and radial magnet length l_m.(a) shows the peak value of the fundamental of the flux density B1 and (b) shows the RMS value of the flux density in the middle of the coil, (c) shows the total harmonic distortion of the flux density in the coil and (d) shows the peak flux density in the armature.

2.1.9 Axially magnetized topology with non-magnetic core

The last topology analyzed in this research is the axial magnetized topology as shown in Fig. 2.20.

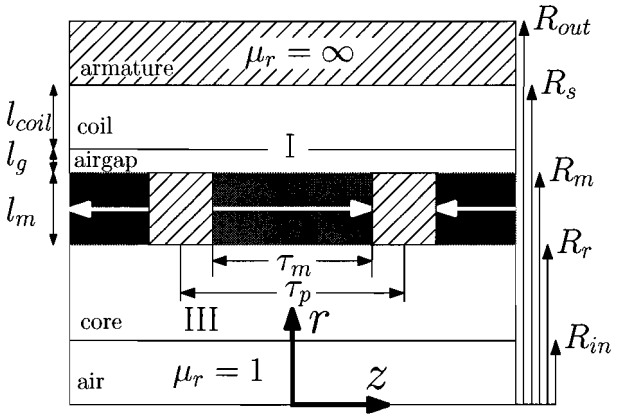

Figure 2.20: Tubular actuator topology with a axial magnetized magnet array with a non-magnetic core. Region I contains the airgap and the winding area, Region II is the magnet region and Region III is the non-magnetic core region.

This topology is similar to the quasi-Halbach topology, where the radially magnetized magnets are replaced by soft-magnetic pole pieces. The main advantage of this topology is the ease of manufacturing as the translator has only axially magnetized magnets. As less magnetic material is used, the actuator is probably cheaper as well. In this section this topology is analyzed and compared to the topologies in the previous sections.

The magnetization vector has only a component in the z-direction and is described as

$$\begin{aligned} \vec{M} = M_z\vec{z} &= \sum_{n=1,2,3,..}^{\infty} M_n \cos(m_n z)\,\vec{z}, \\ M_n &= \frac{4B_{rem}}{\mu_0 \tau_p m_n} \sin\left(\frac{m_n \alpha_p \tau_p}{2}\right). \end{aligned} \tag{2.69}$$

In the previous topologies, the derivation of the field equation was straightforward. Only boundary conditions in the axial direction had to be applied. Due to the soft-magnetic pole pieces in this topology, the magnetic field strength has to be zero at the boundaries of these pole pieces. To fullfill these radial boundary conditions, another base frequency for the Fourier series in region II is proposed. This results in the following expression for the vector potentials in the regions

$$A_{I_\theta} = \sum_{n=1}^{\infty} \frac{1}{m_n}\Big(a_{1n}\mathcal{B}_{\mathcal{I}1}(m_n r) + b_{1n}\mathcal{B}_{\mathcal{K}1}(m_n r)\Big)\cos(m_n z), \tag{2.70}$$

$$A_{III_\theta} = \sum_{n=1}^{\infty} \frac{1}{m_n}\Big(a_{3n}\mathcal{B}_{\mathcal{I}1}(m_n r) + b_{3n}\mathcal{B}_{\mathcal{K}1}(m_n r)\Big)\cos(m_n z), \tag{2.71}$$

for the airgap region and inner air region and for region II

$$A_{II_\theta} = \sum_{j=1}^{\infty} \frac{1}{q_j} \Big(a_{2j} \mathcal{B}_{\mathcal{I}1}(q_j r) + b_{2j} \mathcal{B}_{\mathcal{K}1}(q_j r) \Big) \cos(q_j z) + \frac{B_0 r}{2}, \tag{2.72}$$

where q_j is the spatial frequency in region II, given by

$$q_j = \frac{j2\pi}{\tau_m}. \tag{2.73}$$

Due to the choice of the coordinate system and the chosen spatial frequency forces the magnetic field strength to be zero at the boundaries of the pole pieces. A DC-term, $\frac{B_0 r}{2}$ has to be introduced in the vector potential in region III.

The vector potentials result in the following expressions for the magnetic flux density in the different regions

$$B_{I_r} = \sum_{n=1}^{\infty} \Big(a_{1n} \mathcal{B}_{\mathcal{I}1}(m_n r) + b_{1n} \mathcal{B}_{\mathcal{K}1}(m_n r) \Big) \sin(m_n z) \tag{2.74}$$

$$B_{I_z} = \sum_{n=1}^{\infty} \Big(a_{1n} \mathcal{B}_{\mathcal{I}0}(m_n r) - b_{1n} \mathcal{B}_{\mathcal{K}0}(m_n r) \Big) \cos(m_n z) \tag{2.75}$$

$$B_{II_r} = \sum_{j=1}^{\infty} \Big(a_{2j} \mathcal{B}_{\mathcal{I}1}(q_j r) + b_{2j} \mathcal{B}_{\mathcal{K}1}(q_j r) \Big) \sin(q_j z) \tag{2.76}$$

$$B_{II_z} = \sum_{j=1}^{\infty} \Big(a_{2j} \mathcal{B}_{\mathcal{I}0}(q_j r) - b_{2j} \mathcal{B}_{\mathcal{K}0}(q_j r) \Big) \cos(q_j z) + B_0 \tag{2.77}$$

$$B_{III_r} = \sum_{n=1}^{\infty} \Big(a_{3n} \mathcal{B}_{\mathcal{I}1}(m_n r) + b_{3n} \mathcal{B}_{\mathcal{K}1}(m_n r) \Big) \sin(m_n z) \tag{2.78}$$

$$B_{III_z} = \sum_{n=1}^{\infty} \Big(a_{3n} \mathcal{B}_{\mathcal{I}0}(m_n r) - b_{3n} \mathcal{B}_{\mathcal{K}0}(m_n r) \Big) \cos(m_n z). \tag{2.79}$$

$$\tag{2.80}$$

To solve these equations and find expressions for $a_{1n}, b_{1n}, a_{2j}, b_{2j}$, B_0, a_{3n} and b_{3n}, the follow-

ing boundary conditions have to be applied

$$B_{I_z}\Big|_{r=R_s} = 0, \tag{2.81}$$

$$B_{III_r}\Big|_{r=0} = 0, \tag{2.82}$$

$$B_{II_r}\Big|_{|z|=\frac{\tau_m}{2}} = 0, \tag{2.83}$$

$$B_{I_r}\Big|_{r=R_m,|z|<\frac{\tau_m}{2}} = B_{II_r}\Big|_{r=R_m,|z|<\frac{\tau_m}{2}}, \tag{2.84}$$

$$H_{I_z}\Big|_{r=R_m,|z|<\frac{\tau_m}{2}} = H_{II_z}\Big|_{r=R_m,|z|<\frac{\tau_m}{2}}, \tag{2.85}$$

$$\int_{R_r}^{R_m} 2\pi r B_{II_z}\Big|_{z=\frac{\tau_m}{2}} dr = \int_{\frac{\tau_m}{2}}^{\frac{\tau_p}{2}} 2\pi R_m B_{I_r}\Big|_{r=R_m} dz - \int_{\frac{\tau_m}{2}}^{\frac{\tau_p}{2}} 2\pi R_r B_{III_r}\Big|_{r=R_r} dz, \tag{2.86}$$

$$B_{II_r}\Big|_{r=R_r,|z|<\frac{\tau_m}{2}} = B_{III_r}\Big|_{r=R_r,|z|<\frac{\tau_m}{2}}, \tag{2.87}$$

$$H_{II_z}\Big|_{r=R_r,|z|<\frac{\tau_m}{2}} = H_{III_z}\Big|_{r=R_r,|z|<\frac{\tau_m}{2}}. \tag{2.88}$$

1. Boundary condition 1 (2.81):

$$B_{I_z}\Big|_{r=R_s} = \sum_{n=1}^{\infty} \Big(a_{1n}\mathcal{B}_{\mathcal{I}0}(m_n R_s) - b_{1n}\mathcal{B}_{\mathcal{K}0}(m_n R_s) \Big) \cos(m_n z) = 0 \tag{2.89}$$

This should hold for all z and n, therefore this reduces to

$$a_{1n}\mathcal{B}_{\mathcal{I}0}(m_n R_s) - b_{1n}\mathcal{B}_{\mathcal{K}0}(m_n R_s) = 0. \tag{2.90}$$

2. Boundary condition 2 (2.82):

$$B_{III_r}\Big|_{r=0} = \sum_{n=1}^{\infty} \Big(a_{3n}\mathcal{B}_{\mathcal{I}1}(0) + b_{3n}\mathcal{B}_{\mathcal{K}1}(0) \Big) \sin(m_n z) = 0 \tag{2.91}$$

This should hold for all z and n which gives

$$a_{3n}\mathcal{B}_{\mathcal{I}1}(0) + b_{3n}\mathcal{B}_{\mathcal{K}1}(0) = 0, \tag{2.92}$$

and since $\mathcal{B}_{\mathcal{I}1}(0) = 0$ and $\mathcal{B}_{\mathcal{K}1}(0) = \infty$ this implies that $b_{3n} = 0$ which reduces the expression of the magnetic field in region III to

$$B_{III_r} = \sum_{n=1}^{\infty} a_{3n}\mathcal{B}_{\mathcal{I}1}(m_n r)\sin(m_n z) \tag{2.93}$$

$$B_{III_z} = \sum_{n=1}^{\infty} a_{3n}\mathcal{B}_{\mathcal{I}0}(m_n r)\cos(m_n z) \tag{2.94}$$

3. Boundary condition 3 (2.83):

$$B_{II_r}\Big|_{|z|=\frac{\tau_m}{2}} = \sum_{j=1}^{\infty}\Big((a_{2j}\mathcal{B}_{\mathcal{I}1}(q_j r)+b_{2j}\mathcal{B}_{\mathcal{K}1}(q_j r)\Big)\sin(\pm q_j\frac{\tau_m}{2}) \tag{2.95}$$

$$= \sum_{j=1}^{\infty}\Big((a_{2j}\mathcal{B}_{\mathcal{I}1}(q_j r)+b_{2j}\mathcal{B}_{\mathcal{K}1}(q_j r)\Big)\sin(\pm j\pi) = 0. \tag{2.96}$$

This boundary condition is therefore automatically fulfilled by choosing the proper solution for the magnetic field in region II.

4. Boundary condition 4 (2.84):

$$B_{I_r}\Big|_{r=R_m,|z|<\frac{\tau_m}{2}} = B_{II_r}\Big|_{r=R_m,|z|<\frac{\tau_m}{2}} \tag{2.97}$$

If we consider for now that $|z|<\frac{\tau_m}{2}$ then the above expression becomes

$$\sum_{n=1}^{\infty}\Big(a_{1n}\mathcal{B}_{\mathcal{I}1}(m_n R_m)+b_{1n}\mathcal{B}_{\mathcal{K}1}(m_n R_m)\Big)\sin(m_n z) = \sum_{j=1}^{\infty}\Big(a_{2j}\mathcal{B}_{\mathcal{I}1}(q_j R_m)+b_{2j}\mathcal{B}_{\mathcal{K}1}(q_j R_m)\Big)\sin(q_j z) \tag{2.98}$$

Following the strategy given in appendix (A), the expression becomes

$$a_{2j}\mathcal{B}_{\mathcal{I}1}(q_j R_m)+b_{2j}\mathcal{B}_{\mathcal{K}1}(q_j R_m) = \sum_{n=1}^{\infty}\Big(a_{1n}\mathcal{B}_{\mathcal{I}1}(m_n R_m)+b_{1n}\mathcal{B}_{\mathcal{K}1}(m_n R_m)\Big)\varepsilon(n,j) \tag{2.99}$$

where $\varepsilon(n,j)$ is given by

$$\varepsilon(n,j) = \frac{2}{\tau_m}\int_{-\tau_p}^{\tau_p}\sin(m_n z)\sin(q_j z)dz. \tag{2.100}$$

However since we assumed that $|z|<\frac{\tau_m}{2}$, the integral limits change to

$$\varepsilon(n,j) = \frac{2}{\tau_m}\int_{-\frac{\tau_m}{2}}^{\frac{\tau_m}{2}}\sin(m_n z)\sin(q_j z)dz. \tag{2.101}$$

Solving this integral leads to

$$\varepsilon(n,j) = \frac{\sin v}{v}-\frac{\sin u}{u} \tag{2.102}$$

where

$$u = j\pi+\frac{(2n-1)\pi\alpha_p}{2} \tag{2.103}$$

$$v = j\pi-\frac{(2n-1)\pi\alpha_p}{2} \tag{2.104}$$

5. Boundary condition 5 (2.85):

$$H_{I_z}\Big|_{r=R_m,|z|<\frac{\tau_m}{2}} = H_{II_z}\Big|_{r=R_m,|z|<\frac{\tau_m}{2}} \tag{2.105}$$

$$\Downarrow$$

$$\frac{B_{I_z}}{\mu_0}\Big|_{r=R_m,|z|<\frac{\tau_m}{2}} = \frac{B_{II_z}}{\mu_0\mu_r} - \frac{M_z}{\mu_r}\Big|_{r=R_m,|z|<\frac{\tau_m}{2}} \tag{2.106}$$

If we consider for now that $|z| < \frac{\tau_m}{2}$ then the above expression becomes

$$\begin{aligned}&\frac{1}{\mu_0}\sum_{n=1}^{\infty}\Big(a_{1n}\mathcal{B}_{\mathcal{I}0}(m_nR_m) - b_{1n}\mathcal{B}_{\mathcal{K}0}(m_nR_m)\Big)\cos(m_nz)\\ &= \frac{1}{\mu_0\mu_r}\Bigg(\sum_{j=1}^{\infty}\Big(a_{2j}\mathcal{B}_{\mathcal{I}0}(q_jR_m) - b_{2j}\mathcal{B}_{\mathcal{K}0}(q_jR_m)\Big)\cos(q_jz) + B_0\Bigg) - \frac{1}{\mu_r}\sum_{n=1}^{\infty}M_n\cos(m_nz)\end{aligned} \tag{2.107}$$

rearranging gives

$$\begin{aligned}&\sum_{n=1}^{\infty}\left[\Big(a_{1n}\mathcal{B}_{\mathcal{I}0}(m_nR_m) - b_{1n}\mathcal{B}_{\mathcal{K}0}(m_nR_m)\Big) + \frac{\mu_0}{\mu_r}M_n\right]\cos(m_nz)\\ &\qquad = \frac{1}{\mu_r}\sum_{j=1}^{\infty}\Big(a_{2j}\mathcal{B}_{\mathcal{I}0}(q_jR_m) - b_{2j}\mathcal{B}_{\mathcal{K}0}(q_jR_m)\Big)\cos(q_jz) + \frac{B_0}{\mu_r}\end{aligned} \tag{2.108}$$

Following the strategy given in appendix (A), the expression becomes

$$\begin{aligned}&\Big(a_{1n}\mathcal{B}_{\mathcal{I}0}(m_nR_m) - b_{1n}\mathcal{B}_{\mathcal{K}0}(m_nR_m)\Big) + \frac{\mu_0}{\mu_r}M_n\\ &\qquad = \frac{1}{\mu_r}\sum_{j=1}^{\infty}\Big(a_{2j}\mathcal{B}_{\mathcal{I}0}(q_jR_m) - b_{2j}\mathcal{B}_{\mathcal{K}0}(q_jR_m)\Big)\eta(n,j) + \frac{B_0}{\mu_r}\sigma(n)\end{aligned} \tag{2.109}$$

where $\eta(n,j)$ is given by

$$\eta(n,j) = \frac{1}{\tau_p}\int_{-\tau_p}^{\tau_p}\cos(m_nz)\cos(q_jz)dz. \tag{2.110}$$

However since we assumed that $|z| < \frac{\tau_m}{2}$, the integral limits change to

$$\eta(n,j) = \frac{1}{\tau_p}\int_{-\frac{\tau_m}{2}}^{\frac{\tau_m}{2}}\cos(m_nz)\cos(q_jz)dz. \tag{2.111}$$

Solving this integral leads to

$$\eta(n,j) = \alpha_p\left(\frac{\sin u}{u} + \frac{\sin v}{v}\right) \tag{2.112}$$

The function $\sigma(n)$ is given by

$$\sigma(n) = \frac{1}{\tau_p} \int_{-\frac{\tau_m}{2}}^{\frac{\tau_m}{2}} \cos(m_n z) dz. \tag{2.113}$$

Solving this integral leads to

$$\sigma(n) = \frac{4}{(2n-1)\pi} \sin\left(\frac{(2n-1)\pi\alpha_p}{2}\right). \tag{2.114}$$

6. Boundary condition 6 (2.86):

$$\int_{R_r}^{R_m} 2\pi r B_{II_z} dr = \int_{\frac{\tau_m}{2}}^{\frac{\tau_p}{2}} 2\pi R_m B_{I_r} dz - \int_{\frac{\tau_m}{2}}^{\frac{\tau_p}{2}} 2\pi R_r B_{III_r} dz \tag{2.115}$$

Inserting the equations for the magnetic field gives

$$\begin{aligned} \int_{R_r}^{R_m} r\left[\sum_{j=1}^{\infty}\left(a_{2j}\mathcal{B}_{\mathcal{I}0}(q_j r) - b_{2j}\mathcal{B}_{\mathcal{K}0}(q_j r)\right)\cos(q_j\frac{\tau_m}{2}) + B_0\right]dr \\ = \int_{\frac{\tau_m}{2}}^{\frac{\tau_p}{2}} R_m \sum_{n=1}^{\infty}\left(a_{1n}\mathcal{B}_{\mathcal{I}1}(m_n R_m) + b_{1n}\mathcal{B}_{\mathcal{K}1}(m_n R_m)\right)\sin(m_n z)dz - \\ \int_{\frac{\tau_m}{2}}^{\frac{\tau_p}{2}} R_r \sum_{n=1}^{\infty}(a_{3n}\mathcal{B}_{\mathcal{I}1}(m_n R_r))\sin(m_n z)dz. \end{aligned} \tag{2.116}$$

Since the summation and the integral are linear operators, we may switch them which results in

$$\begin{aligned} \sum_{j=1}^{\infty}\int_{R_r}^{R_m} r\left(a_{2j}\mathcal{B}_{\mathcal{I}0}(q_j r) - b_{2j}\mathcal{B}_{\mathcal{K}0}(q_j r)\right)\cos\left(q_j\frac{\tau_m}{2}\right)dr + \int_{R_r}^{R_m} rB_0 dr \\ = \sum_{n=1}^{\infty}\int_{\frac{\tau_m}{2}}^{\frac{\tau_p}{2}}\left[R_m\left(a_{1n}\mathcal{B}_{\mathcal{I}1}(m_n R_m) + b_{1n}\mathcal{B}_{\mathcal{K}1}(m_n R_m)\right)\sin(m_n z) - \right. \\ \left. R_r(a_{3n}\mathcal{B}_{\mathcal{I}1}(m_n R_r))\sin(m_n z)\right]dz. \end{aligned} \tag{2.117}$$

Solving the integrals leads to

$$\begin{aligned} \sum_{j=1}^{\infty}\frac{1}{q_j}\left[a_{2j}\left(R_m\mathcal{B}_{\mathcal{I}1}(q_j R_m) - R_r\mathcal{B}_{\mathcal{I}1}(q_j R_r)\right) + b_{2j}\left(R_m\mathcal{B}_{\mathcal{K}1}(q_j R_m) - R_r\mathcal{B}_{\mathcal{K}1}(q_j R_r)\right)\right]\cos\left(q_j\frac{\tau_m}{2}\right) \\ + \frac{R_m^2 - R_r^2}{2}B_0 \\ = \sum_{n=1}^{\infty}\left[\frac{R_m}{m_n}\left(a_{1n}\mathcal{B}_{\mathcal{I}1}(m_n R_m) + b_{1n}\mathcal{B}_{\mathcal{K}1}(m_n R_m)\right) - \frac{R_r}{m_n}(a_{3n}\mathcal{B}_{\mathcal{I}1}(m_n R_r))\right]\cos\left(\frac{m_n\tau_m}{2}\right). \end{aligned} \tag{2.118}$$

7. Boundary condition 7 (2.87):

$$B_{II_r}\Big|_{r=R_r,|z|<\frac{\tau_m}{2}} = B_{III_r}\Big|_{r=R_r,|z|<\frac{\tau_m}{2}} \tag{2.119}$$

If we consider for now that $|z| < \frac{\tau_m}{2}$ then the above expression becomes

$$\sum_{j=1}^{\infty}\Big(a_{2j}\mathcal{B}_{\mathcal{I}1}(q_jR_r) + b_{2j}\mathcal{B}_{\mathcal{K}1}(q_jR_r)\Big)\sin(q_jz) = \sum_{n=1}^{\infty} a_{3n}\mathcal{B}_{\mathcal{I}1}(m_nR_r)\sin(m_nz) \tag{2.120}$$

Following the strategy given in appendix (A), the expression becomes

$$a_{2j}\mathcal{B}_{\mathcal{I}1}(q_jR_r) + b_{2j}\mathcal{B}_{\mathcal{K}1}(q_jR_r) = \sum_{n=1}^{\infty} a_{3n}\mathcal{B}_{\mathcal{I}1}(m_nR_r)\varepsilon(n,j) \tag{2.121}$$

where $\varepsilon(n,j)$ is given in (2.102).

8. Boundary condition 8 (2.88):

$$H_{II_z}\Big|_{r=R_r,|z|<\frac{\tau_m}{2}} = H_{III_z}\Big|_{r=R_r,|z|<\frac{\tau_m}{2}} \tag{2.122}$$

$$\Downarrow$$

$$\frac{B_{II_z}}{\mu_0\mu_r} - \frac{M_z}{\mu_r}\Big|_{r=R_r,|z|<\frac{\tau_m}{2}} = \frac{B_{III_z}}{\mu_0}\Big|_{r=R_r,|z|<\frac{\tau_m}{2}} \tag{2.123}$$

If we consider for now that $|z| < \frac{\tau_m}{2}$ then the above expression becomes

$$\frac{1}{\mu_0\mu_r}\left(\sum_{j=1}^{\infty}\Big(a_{2j}\mathcal{B}_{\mathcal{I}0}(q_jR_r) - b_{2j}\mathcal{B}_{\mathcal{K}0}(q_jRr)\Big)\cos(q_jz) + B_0\right) - \frac{1}{\mu_r}\sum_{n=1}^{\infty} M_n\cos(m_nz) = \frac{1}{\mu_0}\sum_{n=1}^{\infty} a_{3n}\mathcal{B}_{\mathcal{I}0}(m_nR_r)\cos(m_nz) \tag{2.124}$$

rearranging gives

$$\sum_{n=1}^{\infty}\left[a_{3n}\mathcal{B}_{\mathcal{I}0}(m_nR_r) + \frac{\mu_0}{\mu_r}M_n\right]\cos(m_nz) = \frac{1}{\mu_r}\sum_{j=1}^{\infty}\Big(a_{2j}\mathcal{B}_{\mathcal{I}0}(q_jR_r) - b_{2j}\mathcal{B}_{\mathcal{K}0}(q_jR_r)\Big)\cos(q_jz) + \frac{B_0}{\mu_r} \tag{2.125}$$

Following the strategy given in appendix (A), the expression becomes

$$a_{3n}\mathcal{B}_{\mathcal{I}0}(m_nR_r) + \frac{\mu_0}{\mu_r}M_n = \frac{1}{\mu_r}\sum_{j=1}^{\infty}\Big(a_{2j}\mathcal{B}_{\mathcal{I}0}(q_jR_r) - b_{2j}\mathcal{B}_{\mathcal{K}0}(q_jR_r)\Big)\eta(n,j) + \frac{B_0}{\mu_r}\sigma(n) \tag{2.126}$$

where $\eta(n,j)$ is given by (2.112), and $\sigma(n)$ is given by (2.114).

From now on, the Bessel functions are replaced by other variables to simplify the equations as given in Appendix B. A summary of the equations gathered from the boundary conditions is given below

$$
\begin{aligned}
a_{1n}C_{17n} - b_{1n}C_{18n} &= 0,\\
a_{2j}C_{15j} + b_{2j}C_{16j} - \sum_{n=1}^{\infty}(a_{1n}C_{11n} + b_{1n}C_{12n})\varepsilon(n,j) &= 0,\\
\left(a_{1n}C_{9n} - b_{1n}C_{10n}\right) - \frac{1}{\mu_r}\sum_{j=1}^{\infty}\left(a_{2j}C_{13j} - b_{2j}C_{14j}\right)\eta(n,j) - \frac{B_0}{\mu_r}\sigma(n) &= -\frac{\mu_0}{\mu_r}M_n,\\
\sum_{j=1}^{\infty}\frac{1}{q_j}\left[a_{2j}\left(R_mC_{15j} - R_rC_{7j}\right) + b_{2j}\left(R_mC_{16j} - R_rC_{8j}\right)\right]\cos\left(q_j\frac{\tau_m}{2}\right) + & \qquad (2.127)\\
\frac{R_m^2 - R_r^2}{2}B_0 - \sum_{n=1}^{\infty}\left[\frac{R_m}{m_n}\left(a_{1n}C_{11n} + b_{1n}C_{12n}\right) - \frac{R_r}{m_n}a_{3n}C_{3n}\right]\cos\left(m_n\frac{\tau_m}{2}\right) &= 0,\\
a_{2j}C_{7j} + b_{2j}C_{8j} - \sum_{n=1}^{\infty}a_{3n}C_{3n}\varepsilon(n,j) &= 0,\\
a_{3n}C_{1n} - \frac{1}{\mu_r}\sum_{j=1}^{\infty}\left(a_{2j}C_{5j} - b_{2j}C_{6j}\right)\eta(n,j) - \frac{B_0}{\mu_r}\sigma(n) &= -\frac{\mu_0}{\mu_r}M_n
\end{aligned}
$$

Elimination of b_{1n} leads to

$$
a_{1n} = \frac{C_{18n}}{C_{17n}}b_{1n} \qquad (2.128)
$$

$$
\begin{aligned}
a_{2j}C_{15j} + b_{2j}C_{16j} - \sum_{n=1}^{\infty}b_{1n}\left(\frac{C_{18n}}{C_{17n}}C_{11n} + C_{12n}\right)\varepsilon(n,j) &= 0,\\
b_{1n}\left(\frac{C_{18n}}{C_{17n}}C_{9n} - C_{10n}\right) - \frac{1}{\mu_r}\sum_{j=1}^{\infty}\left(a_{2j}C_{13j} - b_{2j}C_{14j}\right)\eta(n,j) - \frac{B_0}{\mu_r}\sigma(n) &= -\frac{\mu_0}{\mu_r}M_n,\\
\sum_{j=1}^{\infty}\frac{1}{q_j}\left[a_{2j}\left(R_mC_{15j} - R_rC_{7j}\right) + b_{2j}\left(R_mC_{16j} - R_rC_{8j}\right)\right]\cos\left(q_j\frac{\tau_m}{2}\right) + & \qquad (2.129)\\
\frac{R_m^2 - R_r^2}{2}B_0 - \sum_{n=1}^{\infty}\left[\frac{R_m}{m_n}b_{1n}\left(\frac{C_{18n}}{C_{17n}}C_{11n} + C_{12n}\right) - \frac{R_r}{m_n}a_{3n}C_{3n}\right]\cos\left(m_n\frac{\tau_m}{2}\right) &= 0,\\
a_{2j}C_{7j} + b_{2j}C_{8j} - \sum_{n=1}^{\infty}a_{3n}C_{3n}\varepsilon(n,j) &= 0,\\
a_{3n}C_{1n} - \frac{1}{\mu_r}\sum_{j=1}^{\infty}\left(a_{2j}C_{5j} - b_{2j}C_{6j}\right)\eta(n,j) - \frac{B_0}{\mu_r}\sigma(n) &= -\frac{\mu_0}{\mu_r}M_n.
\end{aligned}
$$

To eliminate the summations, the equations are rewritten into matrices as given in appendix B. As the boundary of the summation, infinity, is not possible to implement, the summations is calculated from $j = 1$ to $j = J$ and $n = 1$ to $n = N$. Now the complete set of equations contains $2J + 2N + 1$ equations and can be written as a matrix multiplication

$$\mathbf{X} = \begin{bmatrix} \begin{bmatrix} -\varepsilon_{JN}\mathbf{C}_{NNa} \end{bmatrix} & \begin{bmatrix} \mathbf{C}_{JJ15} \end{bmatrix} & \begin{bmatrix} \mathbf{C}_{JJ16} \end{bmatrix} & \begin{bmatrix} \mathbf{0}_{JN} \end{bmatrix} & \begin{bmatrix} \mathbf{0}_{J} \end{bmatrix} \\ \begin{bmatrix} \mathbf{C}_{NNb} \end{bmatrix} & \begin{bmatrix} -\frac{1}{\mu_r}\boldsymbol{\eta}_{JN}^T\mathbf{C}_{JJ13} \end{bmatrix} & \begin{bmatrix} \frac{1}{\mu_r}\boldsymbol{\eta}_{JN}^T\mathbf{C}_{JJ14} \end{bmatrix} & \begin{bmatrix} \mathbf{0}_{NN} \end{bmatrix} & \begin{bmatrix} \frac{-1}{\mu_r}\boldsymbol{\sigma}_N^T \end{bmatrix} \\ \begin{bmatrix} -R_m\mathbf{m}_N^T\mathbf{C}_{NNa} \end{bmatrix} & \begin{bmatrix} \mathbf{q}_J\left(R_m\mathbf{C}_{JJ15} - R_\tau\mathbf{C}_{JJ7}\right) \end{bmatrix} & \begin{bmatrix} \mathbf{q}_J\left(R_m\mathbf{C}_{JJ16} - R_\tau\mathbf{C}_{JJ8}\right) \end{bmatrix} & \begin{bmatrix} R_\tau\mathbf{m}_N^T\mathbf{C}_{NN3} \end{bmatrix} & \begin{bmatrix} \frac{R_m^2 - R_\tau^2}{2} \end{bmatrix} \\ \begin{bmatrix} \mathbf{0}_{JN} \end{bmatrix} & \begin{bmatrix} \mathbf{C}_{JJ7} \end{bmatrix} & \begin{bmatrix} \mathbf{C}_{JJ8} \end{bmatrix} & \begin{bmatrix} -\varepsilon_{JN}\mathbf{C}_{NN3} \end{bmatrix} & \begin{bmatrix} \mathbf{0}_{J} \end{bmatrix} \\ \begin{bmatrix} \mathbf{0}_{NN} \end{bmatrix} & \begin{bmatrix} -\frac{1}{\mu_r}\boldsymbol{\eta}_{JN}^T\mathbf{C}_{JJ5} \end{bmatrix} & \begin{bmatrix} \frac{1}{\mu_r}\boldsymbol{\eta}_{JN}^T\mathbf{C}_{JJ6} \end{bmatrix} & \begin{bmatrix} \mathbf{C}_{NN1} \end{bmatrix} & \begin{bmatrix} -\frac{1}{\mu_r}\boldsymbol{\sigma}_N^T \end{bmatrix} \end{bmatrix} \tag{2.130}$$

where

$$\begin{bmatrix} \begin{bmatrix} \mathbf{b}_{N1}^T \end{bmatrix} \\ \begin{bmatrix} \mathbf{a}_{J2} \end{bmatrix} \\ \begin{bmatrix} \mathbf{b}_{J2} \end{bmatrix} \\ \begin{bmatrix} \mathbf{a}_{N3}^T \end{bmatrix} \\ B_0 \end{bmatrix} = \mathbf{X}^{-1} \cdot \begin{bmatrix} \begin{bmatrix} \mathbf{0}_J \end{bmatrix} \\ \begin{bmatrix} -\frac{\mu_0}{\mu_r}\mathbf{M}_N^T \end{bmatrix} \\ 0 \\ \begin{bmatrix} \mathbf{0}_J \end{bmatrix} \\ \begin{bmatrix} -\frac{\mu_0}{\mu_r}\mathbf{M}_N^T \end{bmatrix} \end{bmatrix} \tag{2.131}$$

This matrix is implemented in Matlab and the flux density in the middle of the coil is calculated for $N = 60$ and $J = 60$. The resulting waveform is compared to a FE model and the two methods show very good agreement as shown in Fig. 2.21.

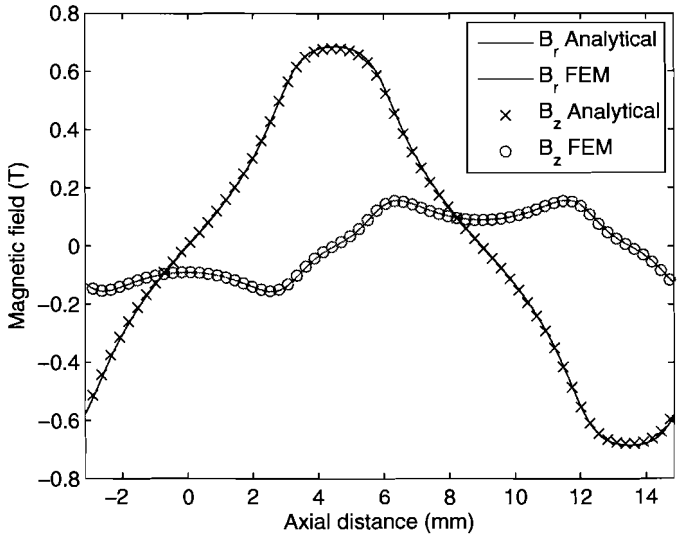

Figure 2.21: Magnetic flux density of the magnets calculated in the middle of the coil ($r = R_s - \frac{l_{coil}}{2}$). Both analytical and FEM results are shown.

2.1.10 Parametric search on the axially magnetized topology

The same approach as presented in the previous section for the quasi-Halbach magnet array is used here. In the first analysis, the effect of both the pole pitch, τ_p, and the ratio of τ_m to τ_p, α_p, on the flux density in the coil are analyzed. The radial magnet length is fixed. The dimensions of the actuator in this analysis are shown in Table 2.7.

Table 2.7: Fixed parameters in analysis

R_{out} (mm)	9.00
l_{stator} (mm)	1.00
l_{coil} (mm)	1.45
l_g (mm)	0.25
l_m (mm)	4.30

In Fig. 2.22 the results of the simulation are shown. In Fig. 2.22a and Fig. 2.22c it can be seen that an optimum exists at $\tau_p \approx 9$mm and $\alpha_p \approx 0.9$. However, the flux density in the pole pieces and in the armature are above 1.5 T at this working point. To avoid saturation in the pole pieces, $\alpha_p < 0.8$. A lower α_p results in less harmonic distortion as well.

The second analysis investigates the effects of τ_p and l_m on the flux density. The sizes as shown in 2.7 are used, and $\alpha_p = 0.75$. Fig. 2.23 shows the results. The main conclusion is that the flux density increases when l_m is enlarged, and the pole pitch optimum is 7mm $< \tau_p <$ 8mm. As can be seen from Fig. 2.23e,f, the soft-magnetic parts are not saturated for $l_m < 4.3$mm

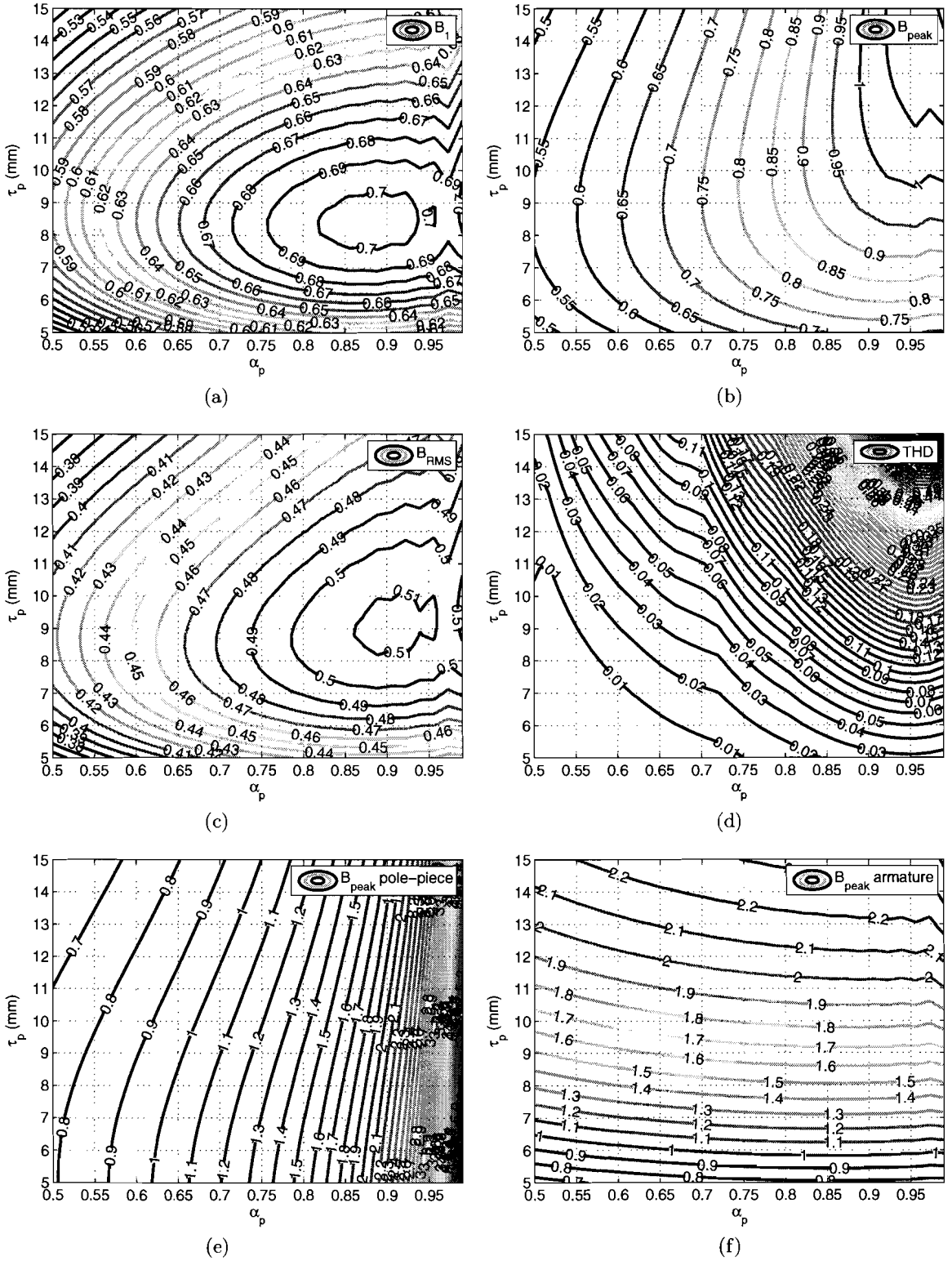

Figure 2.22: Magnetic flux density versus pole pitch τ_p and magnet pitch to pole pitch ratio α_p.(a) to (d) show the flux density in the middle of the coil, (e) shows the peak flux density in the pole pieces and (f) shows the peak flux density in the armature

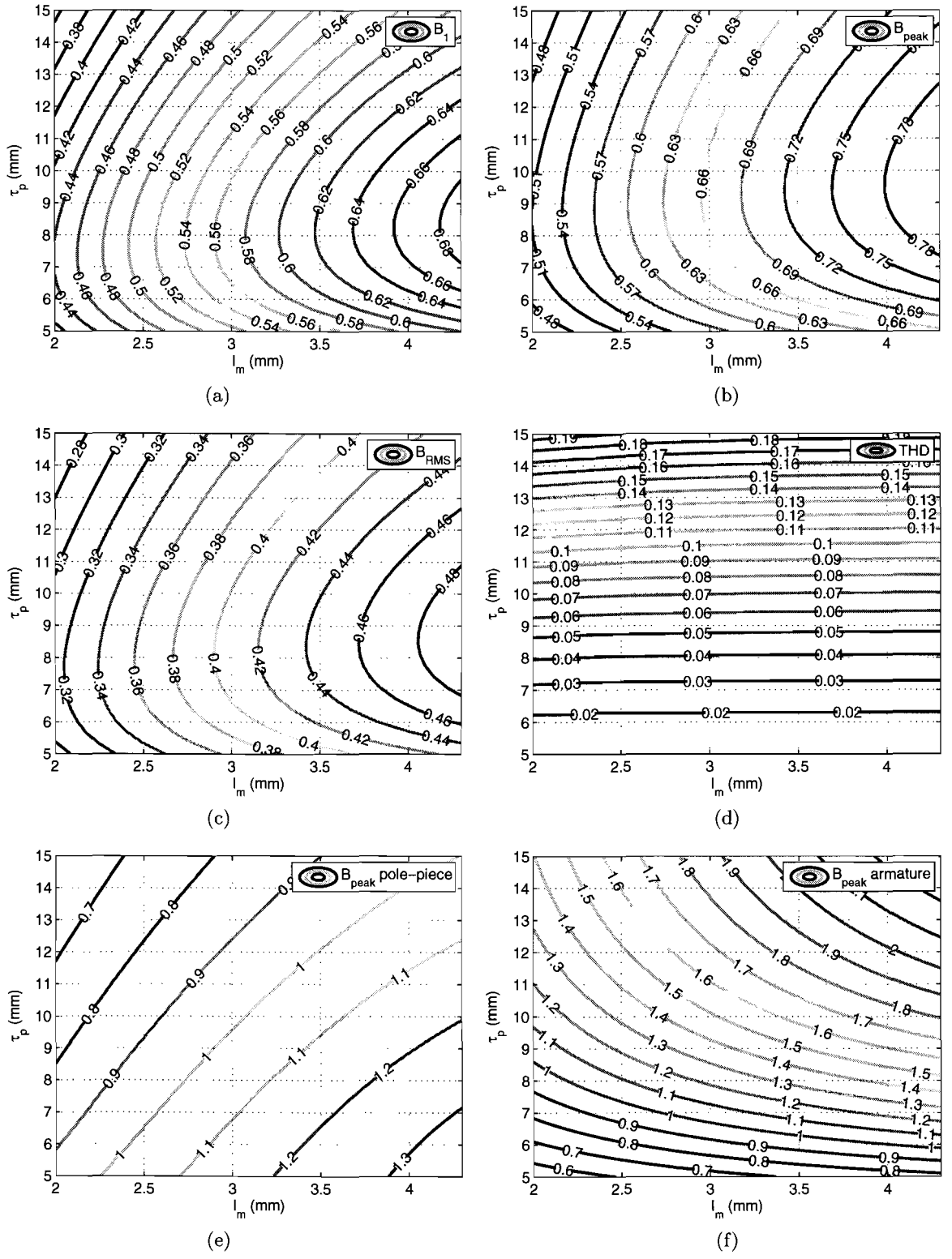

Figure 2.23: Magnetic flux density versus pole pitch τ_p and radial magnet length l_m.(a) to (d) show the flux density in the middle of the coil, (e) shows the peak flux density in the pole pieces and (f) shows the peak flux density in the armature

2.1.11 Conclusions magnetic loading

In the previous parts, four different topologies of the tubular actuator are analyzed. A parametric search is performed on the magnet length, the pole pitch, the radial to axial pole pitch ratio for the Halbach magnet array, and the magnet to pole pitch ration in the axially magnetized topology. The flux density in the coil is calculated in all situations as well as the flux density in the stator and the core.

The first analyzed topology was a tubular actuator with radially magnetized magnets. The main conclusion drawn from the analysis was that the radially magnetized topology is not suitable in this application. Due to the relative small core radius and its minimum inner radius, saturation of the core occurs in all calculations.

To avoid this saturation, a second topology is introduced. The quasi-Halbach magnetized topology concentrates the flux in the airgap and only a small amount of flux flows through the core. This topology gives good results. However, when a high flux density in the coil is desired, the radial stator length of 1.0 mm is too small.

The first and the second topology use a soft-magnetic core. This implies that iron or steel has to be used in these topologies. A non-magnetic core, e.g. aluminium, is favorable due to its lower mass. Therefore, a third topology is introduced, a quasi-Halbach magnet array with non-magnetic core. The magnetic performance of this topology is lower than the for topology of the magnetic core but when the saturation in the stator is taken into account this topology shows better performance.

A fourth topology is introduced in the last section. The axially magnetized topology has the advantage of a non-magnetic core. In the analysis was found that the performance of this topology is comparable to the performance of the quasi-Halbach topology with non-magnetic core. Another advantage of this topology is the manufacturability. All magnets can be magnetized in the same direction, no radially magnetized magnets are necessary.

From the results of the parametric search, a TPMA of the axially magnetized topology, and a TPMA of the quasi-Halbach topology with non-magnetic core are designed. The parameters are chosen such that saturation in the soft-magnetic parts is avoided, the peak value of the fundamental of the flux density is at its maximum, and the total harmonic distortion is low. The geometric parameters for these two designs are shown in Table 2.8.

In Fig. 2.24, the magnetic loading of the two designs are shown. As can be seen, the axially magnetized topology has a higher peak value of the flux density, however, as was shown before, the fundamental and the RMS value of the flux density are approximately the same for both topologies, which will result in comparable forces.

Table 2.8: Geometric parameters for the optimized models

Parameter	quasi-Halbach	Axially magnetized
R_{out} (mm)	9.00	9.00
l_{stator} (mm)	1.00	1.00
l_{coil} (mm)	1.45	1.45
l_g (mm)	0.25	0.25
l_m (mm)	4.30	4.30
τ_p (mm)	8.33	8.33
α_p	0.40	0.75

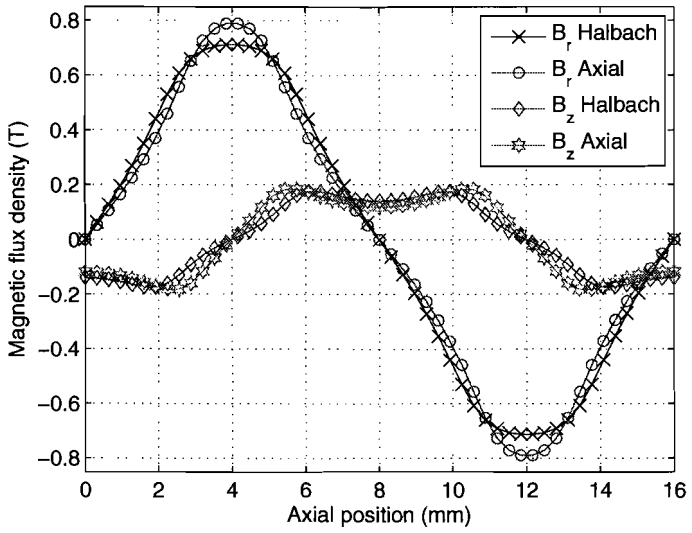

Figure 2.24: Flux density waveforms of the optimized models of the quasi-Halbach magnetized topology with non-magnetic core, and the axially magnetized topology.

2.2 Electrical loading in the z-actuator

The magnetic loading, presented in the previous section, determines only one part of the force. The second part which characterizes the force is the electrical loading. In this section the electrical loading of the z-actuator is presented.

From electrical point of view, the four topologies presented in the previous section belong to two different classes. The two quasi-Halbach topologies and the axially magnetized topology have in principle sinusoidal flux density waveforms in the airgap and a corresponding sinusoidal EMF, and belong to the brushless AC-machines. The radial magnetized topology produces in principle a trapezoidal flux density waveform in the airgap and corresponding trapezoidal EMF. Therefore, this topology is a brushless DC-machine. However, the relative large effective airgap to pole pitch ratio due to the slotless structure, results in a more sinusoidal EMF which makes this topology suitable for sinusoidal excitation as well.

In this section different aspects of the electrical loading are discussed. One of the most important aspect of the electrical loading is the current density in the coils. This is discussed in the next section about thermal issues.

2.2.1 Winding arrangement

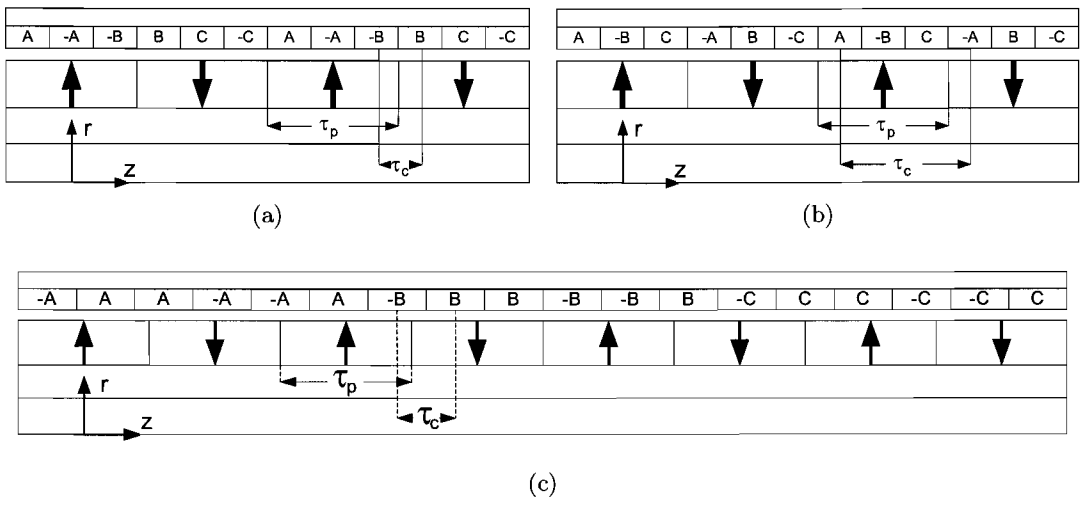

Figure 2.25: Winding arrangements for slotless three phase tubular actuators. (a) Brushless DC winding (short-pitch). (b) Brushless AC winding (full-pitch). (c) Example of a modular winding (18 coil / 8 pole combination).[6]

Three commonly used winding arrangements are shown in Fig. 2.25. A brushless DC (BLDC) winding as shown in Fig. 2.25a is a short-pitched winding with two coils per phase per pole pair. The coil pitch, τ_c, is one third of the pole pitch, τ_p. In rotary actuators, the short-pitched winding has the advantage of a short end winding, which results in a high efficiency. However, since a tubular actuator has no end windings, this advantage does not exist. The disadvantage of this short pitched winding is the lower winding factor for the fundamental EMF.

The short pitched winding is often used to reduce the EMF harmonics and the force ripple. In a slotted structure, the BLDC winding could be more favorable than the BLAC winding as it has three slots per pole pair instead of six slots per pole pair in a BLAC winding. This increased number of slots can be a significant disadvantage from manufacturing point of view. However, in the slotless structure the size of the coils is the same for BLDC and BLAC windings.

The brushless AC-winding, shown in Fig. 2.25b, is a full pitched coil with three coils per pole. This winding configuration has a winding factor of one, however higher MMF harmonics are not reduced in the EMF and will produce a force ripple.

The third winding arrangement shown in Fig. 2.25c is the modular winding. This winding arrangement offers significant advantages over conventional tubular BLAC and BLDC windings in a slotted actuator. Each phase winding contains three adjacent concentrated coils. This results in a high winding factor and a smaller number of coils for a given number of poles. The coil width in this winding is $\frac{4}{9}\tau_p$ compared to a coil width of $\frac{3}{9}\tau_p$ in conventional windings. In a slotted actuator, this results in a smaller number of slots and a fractional number of slots per pole. This reduces the cogging force due to stator slotting and the manufacturing cost since less slots are necessary. In a slotless actuator the main advantage of this winding arrangement is the lower number of connections in the actuator.

Slotless actuators exhibit no cogging force due to stator slotting, and as shown in the previous section, the flux density in the coil contains a negligible amount of higher harmonics. Therefore, there is no need for fractional coil pitch to pole pitch ratio to reduce EMF harmonics. To obtain a high winding factor without disturbances due to higher MMF harmonics, simple full pitch BLAC windings, as shown in Fig. 2.25b, can be used in this design. While using this winding arrangement, the force is only produced by the fundamental of the flux density and the current.

Fig. 2.26 shows the EMF induced by the winding arrangement shown in Fig. 2.25b. The waveform is calculated using a FE model of the quasi-Halbach topology with non-magnetic core. The velocity of the translator during the calculation is $v = 1.0$ m/s. The optimized parameters found in the previous section are used in this model. The design of the axially magnetized topology shows a very similar EMF.

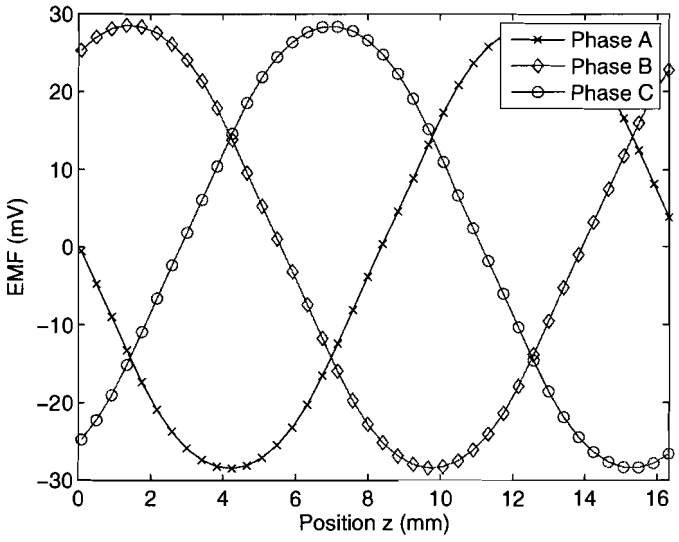

Figure 2.26: EMF calculated by FEM per turn per coil at a velocity of $v = 1.0$ m/s. The optimized quasi-Halbach topology with non-magnetic core shown in Table 2.8 is used.

2.2.2 Inductances

The self-inductances and mutual inductances of the full-pitch AC windings are calculated using the FEM package FLUX2D for both the axially magnetized topology and the quasi-Halbach topology. The inductances are defined from magnetic point of view by the flux linkage divided by the current through the coil

$$L_{ph} = \frac{\Psi_{ph}}{I_{ph}}, \tag{2.132}$$

$$M_{ph_i,ph_j} = \frac{\Psi_{ph_i,ph_j}}{I_{ph_j}}, \tag{2.133}$$

where L_{ph} is the phase inductance, Ψ_{ph} is the flux linked by the phase coil and I_{ph} is the current through the coil. M_{ph_i,ph_j} is the mutual inductance of phase i due to current in phase j, Ψ_{ph_i,ph_j} is the flux linkage of phase i due to current in phase j. From electrical point of view, the inductances are defined as

$$L_{ph} = \frac{U_{ph}}{\omega I_{ph}}, \tag{2.134}$$

$$M_{ph_i,ph_j} = \frac{U_{ph_i,ph_j}}{\omega I_{ph_j}}, \tag{2.135}$$

where U_{ph} is the voltage at the terminals of the coil when the coil is not moving in an external field and the voltage drop due to the resistance of the windings is neglected.

Both Ψ_{ph} and U_{ph} can be obtained from FLUX2D results, however for the calculation of U_{ph} a time stepping simulation is required whereas for the calculation of Ψ_{ph} a simple magneto-static analysis is sufficient. Here, the inductance is calculated with both methods

and the results were in agreement. In the models the magnet sources were set to zero to be able to calculate only the flux linkage, or voltage, produced by the coils. This is valid when the influence of saturation of the stator part by the magnets is negligible. As the windings are mainly surrounded by other windings and magnets, with a permeability close to one, the possible saturation of the iron parts by the magnets can be neglected.

The dimensions stated in Table 2.8 are used in the FE model. The stator back-iron in the model is two pole pitches longer than the active stator length. Therefore, the end effects due to the finite length of the stator back-iron are not taken into account. In the next section about end-effects, the final length of the stator back-iron will be obtained which can result in a small deviation of the inductances. The found coil self- and mutual-inductances per turn for the quasi-Halbach topology with non-magnetic core are

$$\begin{bmatrix} L_A & M_{A,B} & M_{A,C} \\ M_{B,A} & L_B & M_{B,C} \\ M_{C,A} & M_{C,B} & L_C \end{bmatrix} = \begin{bmatrix} 18.6 & 7.0 & 6.3 \\ 7.0 & 18.6 & 7.0 \\ 6.3 & 7.0 & 18.6 \end{bmatrix} \text{nH} \tag{2.136}$$

The mutual inductances $M_{C,A}$ and $M_{A,C}$ are lower as the coils of phases C and A are placed at the ends of the coil array as can be seen in Fig. 2.25b.

In a second model, the inductances of the axially magnetized topology are calculated. Due to the soft-magnetic pole pieces, the reluctance is position dependent. Therefore, the inductance is position dependent as well, the minimum and maximum values of the inductance are shown in (2.137) and (2.138)

$$\begin{bmatrix} L_A & M_{A,B} & M_{A,C} \\ M_{B,A} & L_B & M_{B,C} \\ M_{C,A} & M_{C,B} & L_C \end{bmatrix} = \begin{bmatrix} 21 & 8.2 & 8.0 \\ 8.2 & 21 & 8.2 \\ 8.0 & 8.2 & 21 \end{bmatrix} \text{nH} \tag{2.137}$$

$$\begin{bmatrix} L_A & M_{A,B} & M_{A,C} \\ M_{B,A} & L_B & M_{B,C} \\ M_{C,A} & M_{C,B} & L_C \end{bmatrix} = \begin{bmatrix} 25 & 9.3 & 9.0 \\ 9.3 & 25 & 9.3 \\ 9.0 & 9.3 & 25 \end{bmatrix} \text{nH} \tag{2.138}$$

2.2.3 Number of turns

The number of turns, N_{turns}, of each coil is an important quantity in the electrical design of the actuator as it defines the amplitude of the induced voltage, the inductance, the coil resistance and the necessary input current. The coil voltage, e.g. a coil of phase A, u_A, as function of the number of turns, N_{turns}, the coil self inductance per turn, L_A, the mutual inductances per turn, $M_{A,B}$ and $M_{A,C}$, and the current, i_A, is

$$u_A = \underbrace{N_{turns}\frac{d\phi_A}{dt}}_{\text{EMF}} + \underbrace{N_{turns}^2 L_A \frac{di_A}{dt} + N_{turns}^2 M_{A,B}\frac{di_B}{dt} + N_{turns}^2 M_{A,C}\frac{di_C}{dt}}_{\text{inductive part}} + \underbrace{R_{wire} i_A}_{\text{resistive part}}, \tag{2.139}$$

where R_{wire} is the resistance of the coil

$$R_{wire} = \rho_{Cu}\frac{l_{wire}}{A_{wire}}. \tag{2.140}$$

In Fig. 2.27a, the relation between the number of turns, N_{turns}, and the peak value of the coil voltage, U_A, and the peak value of the phase current, I_A, is plotted for a velocity of 1.0 m/s

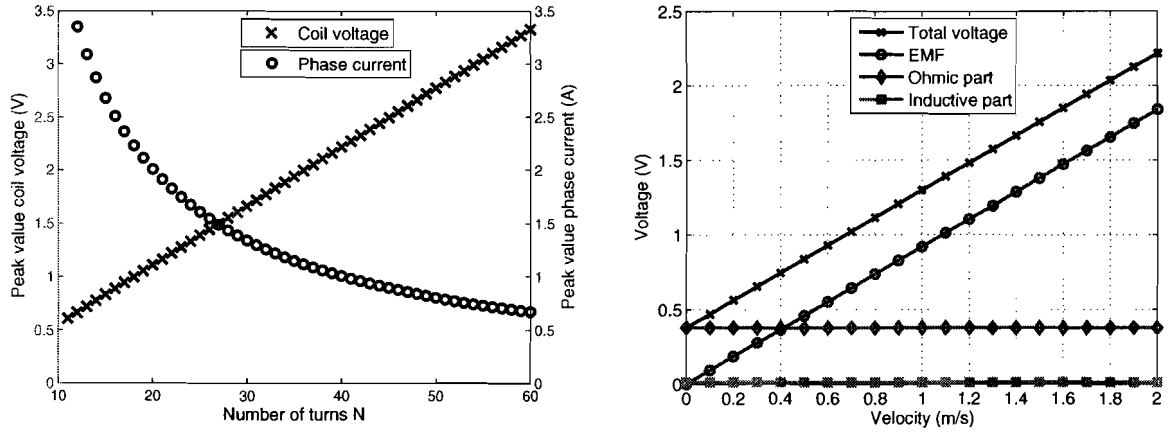

(a) (b)

Figure 2.27: (a) Coil voltage and current per coil vs the number of turns at a velocity of $v = 1$ m/s, and (b) different components of coil voltage versus velocity for $N_{turns} = 40$, calculated using the results from Fig. 2.26, (2.136) and (2.138). The given values are calculated with a current density of $J_{RMS} = 5\text{A/mm}^2$ and a fill factor of 0.6.

and a current density in the coil area of $J_{RMS} = 3.3$ A/mm^2. Fig. 2.27b shows the different components of the coil voltage for $N_{turns} = 15$ and $J_{RMS} = 5$ A/mm^2. The inductive part of the voltage is negligible compared to the resistive part during constant velocity. However, during the change of the acceleration, jerk, the $\frac{di}{dt}$ term will be significantly higher. As the inductance per turn per coil is very low, as shown in (2.136), the inductive part of the voltage is only significant for an very high jerk.

The EMF from Fig. 2.26 and the inductances from (2.136) and (2.138) are used to calculate the coil voltage. The phase voltage and current are restricted by the inverter specifications shown in Section 1.2. Therefore, a suitable number of turns has to be chosen.

2.3 Force calculations

In this section, the results of the magnetic loading and the electrical loading are combined to calculate the force produced by the actuator. As is stated in the requirements in Chapter 1, the main action of the z-actuator is accelerate and decelerate at 150 m/s^2. An additional action is the static force of 40N. The friction is neglected in the calculations.

The acceleration of the translator in the z-direction, a_z, is restricted by the mass of the translator and the load, m, and the force produced by the actuator in the z-direction, F_z,

$$F_z = ma_z. \tag{2.141}$$

As the mass of the load is negligible in this application, only the mass of the translator is considered here. The translator consists of two parts, the active part which is inside the stator and interacting with the coils, and the stroke which is outside the stator. The force of the actuator is proportional to the active length of the translator, the mass of the translator is

proportional to the active length and the stroke

$$F_z \propto l_{active}, \tag{2.142}$$

$$m \propto l_{active} + l_{stroke}. \tag{2.143}$$

Therefore, the acceleration of the translator is not directly proportional to the stator length (active length), this is depicted in Fig. 2.28. As can be seen, the acceleration increases rapidly

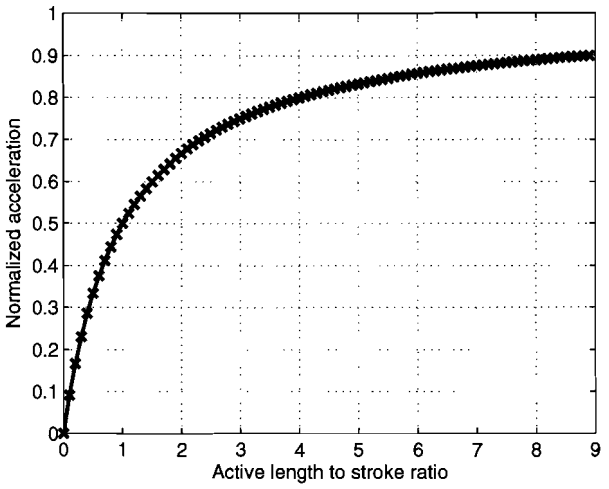

Figure 2.28: Force produced by the z-actuator and the maximum acceleration of the translator for several values of active length. The length of the translator is the length of the stroke, $l_{stroke} = 35mm$ and the active length of the translator.

when the ratio between the active length and the stroke is small, and converges when the active length becomes much larger than the stroke.

2.3.1 Force model

The analytical field equations obtained in Section 2.1 are implemented in Matlab to calculate the force produced by the actuator. Two models have been made with the optimized dimensions shown in Table 2.8. In the calculations in this section the active length of the actuator is set to $12\tau_p = 100$mm. This results in twelve coils of each phase. As the length of the stroke is 35 mm, and the translator has to contain an even number of radially magnetized magnets, the translator length is 145.0 mm $(17\tau_p + \tau_{mr})$ for the quasi-Halbach topology, and 143.7 mm for the axially magnetized topology. The actuator can simply be extended by more pole-pairs on the translator and coils in the stator to provide more force.

As the z-actuator is a slotless structure, the force can be calculated using the Lorentz force equation. [8]

$$\vec{F} = -\int_V \vec{J} \times \vec{B}\, dV \tag{2.144}$$

where $\vec{J}$ is the current density and $\vec{B}$ the magnetic flux density. Although both $\vec{J}$ and $\vec{B}$ can be described analytically, the integral is difficult, if not impossible, to solve analytically. Therefore, the integral is approximated by modeling multiple current sheets in the coil region.

The coil is split into several slices where in each slice the magnetic flux density, $\vec{B}$ is calculated and multiplied by the current in the current sheet, which is put in the middle of the slice. Fig. 2.29 shows the effect of increasing the number of slices in the coil region on the calculated force. Although the radial length of the coil is large with respect to the total radius of the

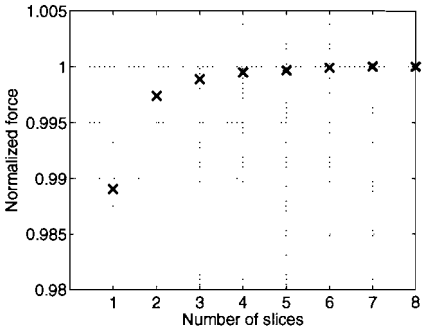

Figure 2.29: Effect of splitting the coil area into multiple slices for force calculation.

actuator, which results in a relatively large deviation of the flux density over the coil area, the effect of multiple slices for the force calculation is very small. The force converges for a small number of slices to a fixed value and the force calculated with one slice deviates less than two percent from the final value. Therefore, time can be saved by using a small number of slices without reduction of accuracy. Note that this figure shows only the effect of the slices on the resulting mean value of the force and not the force waveform. In all calculations in this section, the number of slices in the calculations is set to eight.

The results of the analytical model created in Matlab are compared with a time-stepping FE model. As in the Matlab model the end effects are neglected, the stator part of the actuator in the FE model is made longer than the length of the translator plus the length of the stroke. Fig. 2.30 shows the results of both models of the quasi-Halbach topology. The results are in good agreement, the difference in mean value is less than two percent.

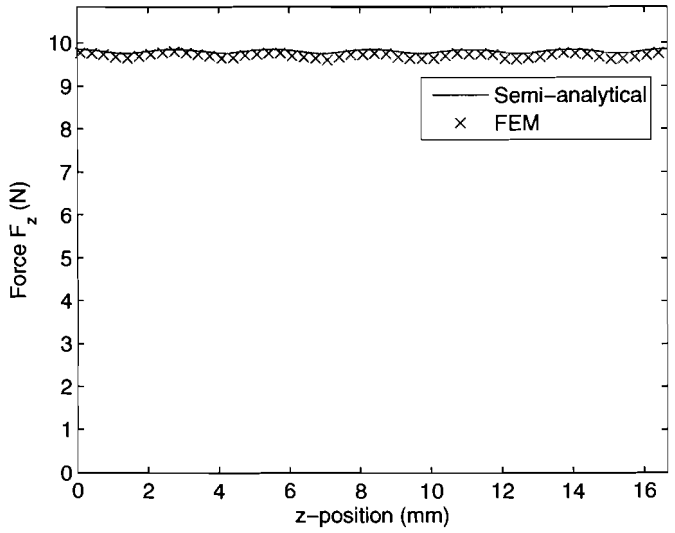

Figure 2.30: Force calculated for the quasi-Halbach topology by the semi-analytical model and the FE model and a current density of 2.8 A/mm^2.

2.3.2 Thermal constraints

As stated in (2.144), the force of the actuator proportional to the current. Therefore, a high current density is desirable to increase the force and the acceleration. However, the copper losses in the coil increase quadratically with the current

$$P_{Cu} = I^2 R. \tag{2.145}$$

This power is converted to heat in the coil and causes a temperature rise of the actuator. Therefore, the current has to be limited to prevent overheating and a low efficiency of the actuator.

The heat is removed from the actuator by radiation, convection and conduction. The amount of heat that can be removed depends on the ambient temperature and the structure of the actuator. Usually most heat is removed by convection. However, the amount of heat removed by radiation can be enlarged by e.g. painting the actuator black. The heat transfer coefficient, h, is used to express the amount of energy that can be removed from an surface while there is a temperature difference between the surface and the ambient of ΔT,

$$h \left[\frac{\mathrm{W}}{\mathrm{m^2K}}\right]. \tag{2.146}$$

The assumption is made that the thermal resistance of the actuator is negligible, this implies that in the calculation the outer temperature of the actuator is equal to the temperature of the coils. This results in the following restriction of the current density

$$\Delta T = J^2 l_{coil} \rho_{\mathrm{Cu}} \left(R_s - \frac{l_{coil}}{2}\right) \frac{1}{k_p R_{out} h}, \tag{2.147}$$

The heat transfer coefficient has values of approximately 20 $W/m^2/K$ when only natural cooling and convection is used for cooling, up to 70 $W/m^2/K$ when forced air cooling is used [9].

In the requirements in Section 1.2 is stated that the worst case duty cycle is 34%. In this calculation is assumed that during the maximum acceleration and deceleration the maximum current is applied to the windings, and during the remaining time of the cycle no current is applied to the windings. This duty cycle is used to calculate the continuous power dissipated in the coils. The semi-analytical models in Matlab are extended with the thermal restriction and the force and acceleration are calculated for several values of h and ΔT. The results of the calculation are shown in Fig. 2.31. As can be seen, for a $\Delta T = 40°C$ an acceleration of

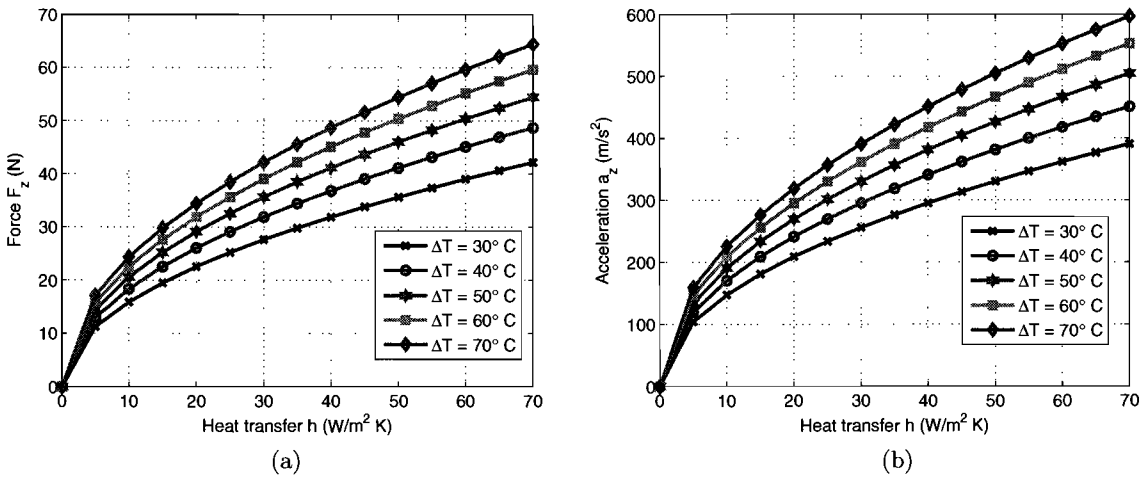

Figure 2.31: The influence of the heat transfer coefficient, h, on the (a) force and (b) the acceleration plotted for several values of ΔT for a duty cycle of 34%.

150 m/s^2 can be achieved with a heat transfer coefficient of $h = 10$.

2.3.3 Parametric analysis

In Section 2.1, a parametric search is performed with the aim to obtain the highest flux density in the coil region. However, the highest acceleration is not always achieved in that optimum as the mass of the translator has to be taken into account as well. Therefore, additional simulations with the analytical model of the quasi-Halbach topology with non-magnetic core and the axially magnetized topology are performed to obtain the influence of several parameters on the acceleration of the translator.

The magnetic loading of actuator is almost linear with respect to the radial magnet length within the possible range of the requirements. Thus, for constant current, the force is linear with the radial magnet length as well. However, the magnetic material used in most high-performance PM actuators, NdFeB, has a significant mass density of 7600 kg/m^3, thus more magnet material results in a higher translator mass and therefore a lower acceleration. In Fig. 2.32, the results of the simulation are shown. For both topologies, the force increases when the radial magnet length is enlarged. However, for the quasi-Halbach topology the

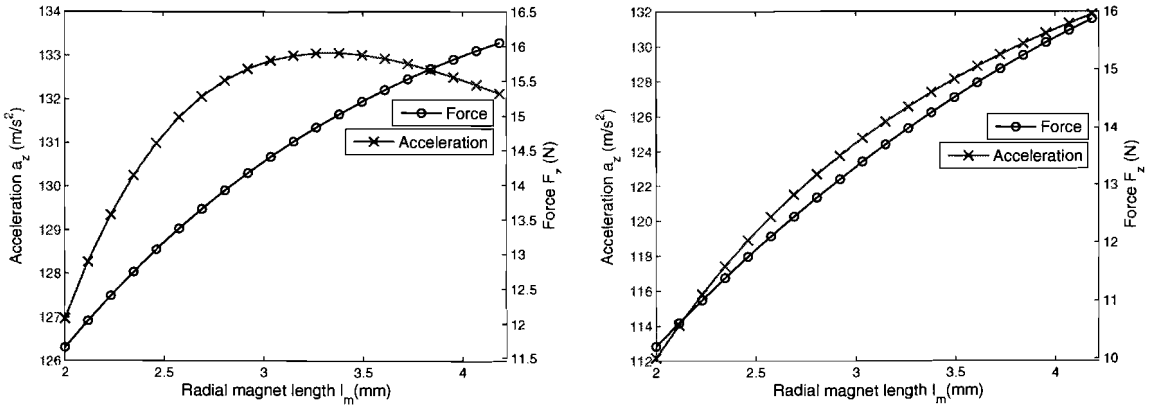

Figure 2.32: Force and acceleration versus radial magnet length for constant R_m. (a) quasi-Halbach topology with non-magnetic core, (b) axially magnetized topology.

acceleration start to decrease for $l_m > 3.3$ mm, the mass increases faster than the force. As the decrease of the acceleration is less than 1%, the larger radial magnet length is probably favorable because the force is increased with 7%.

A second analysis is performed to find the best ratio of magnetic and electrical loading. The acceleration and force are calculated for several combinations of radial coil length, l_{coil}, and radial magnet length, l_m. As the temperature of the actuator is an important constraint, in the first simulation, the current in the coils varies to have a constant ΔT. As a result of the changing outer area due to a changing l_m+l_{coil}, the power dissipated in the coil varies while ΔT is constant (see (2.147)). In Fig 2.33a and Fig. 2.33b, the results of the simulation are shown for quasi-Halbach topology and the axially magnetized topology respectively. The dashed lines show values of constant the force, the solid lines values of constant the acceleration. The thick line marks the flux density in the armature, and for the axially magnetized topology the flux density in the pole pieces. To avoid saturation, a working point above this line is required. The cross-marks show the best combinations of values for l_{coil} and l_m.

As can be seen, increasing the magnet length results in a higher force capability. However, the increased magnet length causes a rise of the translator mass resulting in a lower acceleration. Therefore, a trade-off has to be made as both high acceleration and high peak force are required. Note that increasing the active length results in a higher force as well, without affecting the acceleration negatively.

A second important aspect in actuator design is efficiency. Therefore, a second simulation is done with varying current to have a constant power dissipation in the coils. Fig 2.34a and Fig. 2.34b show the results of the simulation for the quasi-Halbach topology and the axially magnetized topology respectively. The main difference between these results and the results for a constant ΔT are the shifted optima.

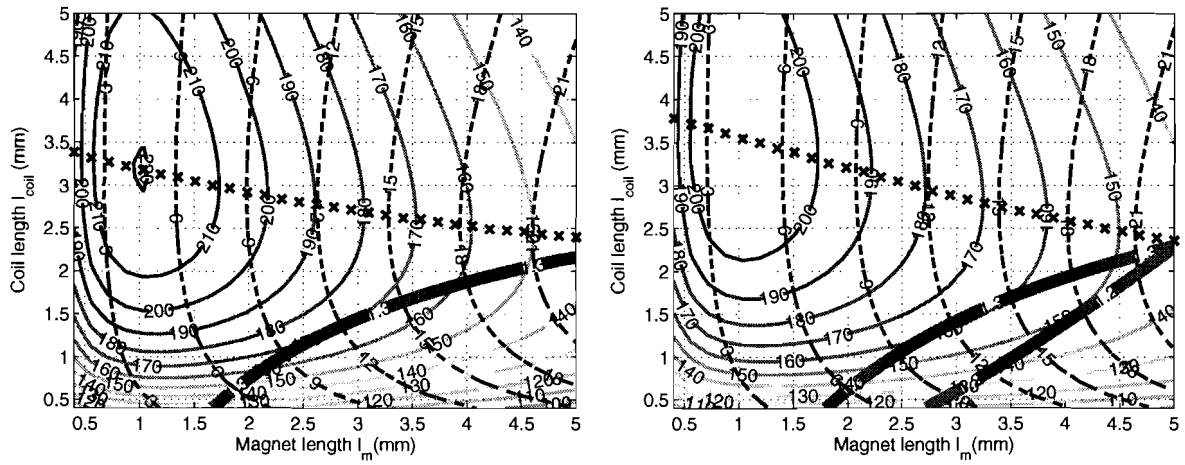

Figure 2.33: Force (dashed line) and acceleration (solid line) versus coil length, l_{coil}, and magnet length, l_m. The current in the coils changes to have a constant $\Delta T = 40°C$ in all cases for a duty cycle of 34%. (a) Quasi-Halbach topology, (b) axially magnetized topology.

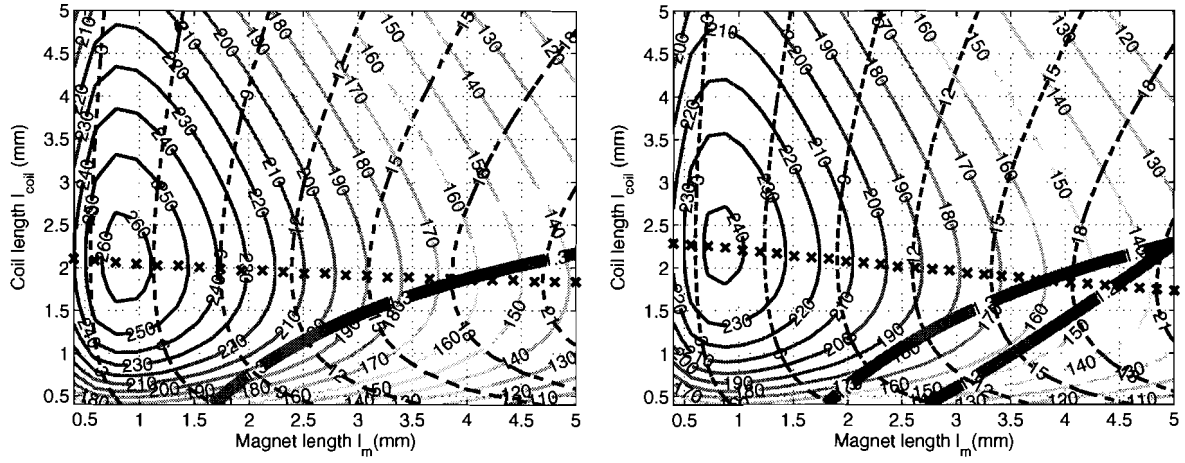

Figure 2.34: Force (dashed line) and acceleration (solid line) versus coil length, l_{coil}, and magnet length, l_m. The current in the coils changes to have a constant copper loss in all cases. (a) Quasi-Halbach topology, (b) axially magnetized topology.

2.3.4 End-effects

Due to the abrupt change in permeance of the magnetic circuit at the ends of the tubular actuator, a cogging component arises in the force. This force component contaminates the resultant force of the actuator and therefore has to be minimized. In literature, several

papers describe methods to minimize these end-effects [24],[25], [26]. However, in the papers the translator is assumed to be much longer than the stator, which implies that only the effect of the finite length of the armature is taken into account. In this application a second end-effect has to be taken into account, the finite length of the translator. As the acceleration has to be maximized, the translator length has to be minimized, which results in a translator length of the active length plus the stroke. This implies that the end of the translator reaches the stator end.

In the papers different methods to minimize the end-effects are presented. In order to save time and simplify the design, the end-effects for the quasi-Halbach topology are minimized using a FE model as described in [26]. The translator is only at one side of the actuator outside the armature as shown in Fig. 2.35. This results in end-effects at only one side of

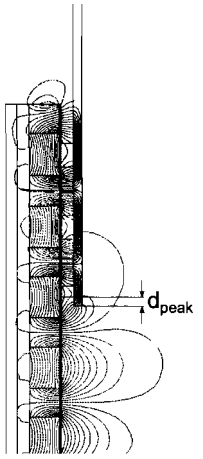

Figure 2.35: FE model of the quasi-Halbach topology to obtain the end-effects of one side of the translator.

the armature. As the end-effects are the same at both sides of the translator only shifted by an angle which depends on the length of the armature, the armature length can now be optimized to minimize the resulting end-effects. As described in [26], the translator is moved out the armature until position where the cogging force is maximum. At that position, the value of d_{peak} is obtained. Now the optimal armature length for minimum cogging force is

$$l_{ax} = k\tau_p + 2d_{peak}, \tag{2.148}$$

where k is an integer. A new FE model is made with an armature length where the cogging force is minimized and the results are compared with the cogging force of a model with $l_{ax} = k\tau_p$. In the model, on both sides of the actuator at least one pole pair of the translator is outside the armature to neglect the effect of the finite length of the translator. The results are shown in Fig. 2.36. The fundamental of the cogging force, which has a period of one pole-pitch, τ_p, is reduced by a factor 68. The effect on the higher harmonics is negligible and the second harmonic becomes dominant. Other techniques, i.e. end-skewing as described in [25], can be used to reduce other harmonics. Further research on this topic is necessary to minimize the cogging force using these techniques, and to minimize the cogging force of the axially magnetized topology.

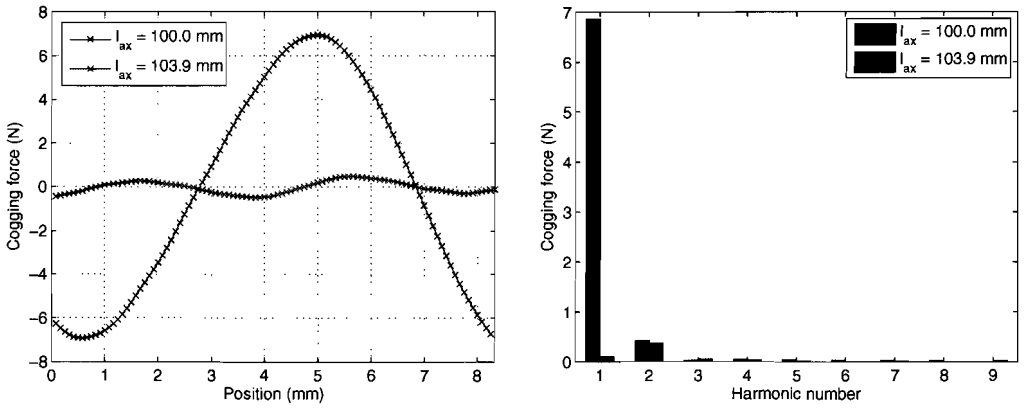

Figure 2.36: (a) Cogging force waveform of the quasi-Halbach topology for an armature length of $l_{ax} = 100$ mm ($k\tau_p$) and for an optimized armature length of $l_{ax} = k\tau_p + 2d_{peak}$ (b) Cogging force spectrum for an armature length of $l_{ax} = 100$ mm ($k\tau_p$) and for an optimized armature length of $l_{ax} = k\tau_p + 2d_{peak}$.

To show the effect of the changing armature length on the resulting cogging force of both ends of the armature, five FE models with different armature length are made with an armature length close to the length with minimum cogging force. In a time-stepping simulation the harmonics in the resulting force are calculated and shown in Fig. 2.37.

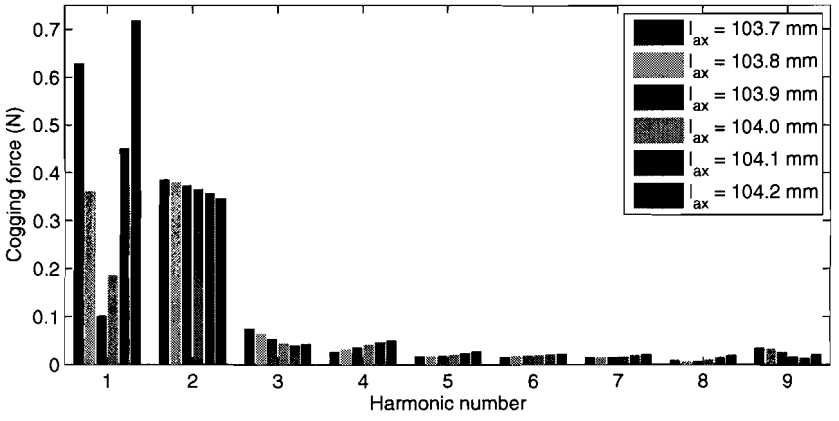

Figure 2.37: Harmonic spectrum of the cogging force due to finite armature length, l_{ax}, for several values of armature length of the quasi-Halbach topology.

Note that all results above do not show the end effect of the finite length of the translator. Taking this effect into account by moving the translator to both ends of the armature results in the force waveform shown in Fig. 2.38. As can be seen an additional symmetric cogging force is introduced due to the finite length of the translator. As the translator mass of this model is 114 g, a acceleration of 150 m/s^2 requires a force of 17 N. Thus the amplitude of

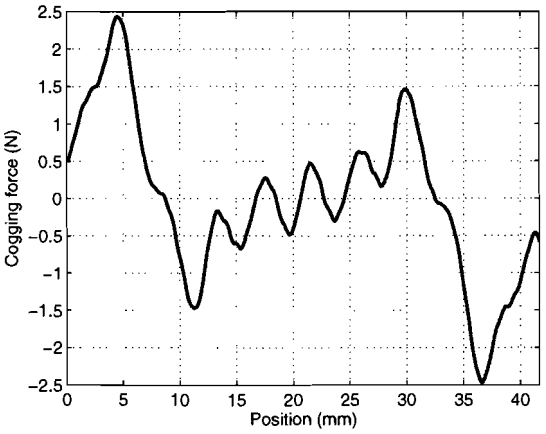

Figure 2.38: Cogging force waveform obtained by FEA by moving the translator to both ends of the armature for an armature length $l_{ax} = k\tau_p + 2d_{peak}$.

the force ripple due to end-effects as shown in Fig. 2.38 is 7%. More research is necessary to minimize all the end-effects.

2.4 Losses

The losses in the tubular actuator can be split in two main parts. The ohmic losses, P_{ohmic}, in the windings and the eddy current losses, P_{eddy}, caused by the changing magnet field in conducting parts of the actuator. The friction losses are neglected here.

2.4.1 Ohmic losses

The ohmic losses in the windings are proportional to the current squared.

$$P_{ohmic} = I_{wire}^2 R_{wire} N_{coils}. \tag{2.149}$$

However the current through a wire, I_{wire}, and the resistance of a wire, R_{wire}, depend on the number of turns, N, the ohmic losses do not depend on the number of turns. Thus the ohmic losses depend on the current density in the coil, J_{coil}, the coil area A_{coil}, the fill factor and the resistance of copper. As the force is proportional to the current the copper losses are proportional to the force squared. The ohmic losses and the force versus the current density are shown in Fig. 2.39. The losses are the total losses calculated for 36 coils with a radial coil length, $l_{coil} = 1.75$ mm, and a coil width of $\tau_p/3$.

In the previous section, a translator mass of 114 g was found. Therefore a force of 17 N is required to accelerate with 150 m/s^2 which result in an ohmic loss of approximately 6.5 W.

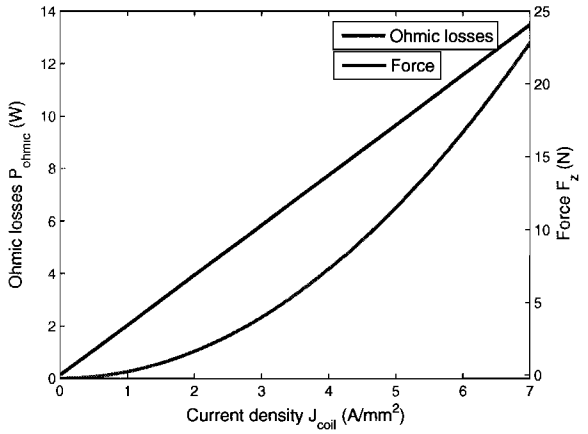

Figure 2.39: Ohmic losses and force versus the RMS value of the current density in the coil with a fill factor of 0.6.

2.4.2 Eddy current losses

The eddy current losses in the armature are dominant. Therefore, only the eddy current losses are calculated using a FE model. The armature in the model is modeled as AI1010 mild steel with a resistivity of $\rho = 2\text{x}10^{-7}\Omega m$. As the eddy current losses are proportional to the frequency of the magnetic field in the iron squared, and therefore to the velocity of the translator squared, the mean value of the velocity squared during one pick action as specified in Section 1.2 is calculated. The imposed velocity of the translator in the FE model is set to this value of 1.0 m/s. The calculated value of the eddy current losses induced in the armature is

$$P_{eddy} = 1.5\text{W}. \tag{2.150}$$

This power is dissipated as heat and causes therefore an additional heat source to the 6.5 W power due to ohmic losses. As the eddy current losses causes damping as well, the required force during acceleration is increased.

Consider the first 23 ms of the motion profile of the linear motion shown in Fig. 1.3, which describes half of the pick action. With the assumption that the mass of the translator is 115 g, the required thrust force is calculated from the acceleration. The mechanical power is defined as

$$P_{mech} = F_{thrust}v, \tag{2.151}$$

where v is the velocity of the translator. Using the eddy current loss power calculated in the previous section, the mechanical, ohmic, and eddy current power can be calculated for the motion profile.

As the eddy current loss has to be considered as a damping force, the eddy current power is added to the mechanical power to calculate the required power for constant force. Fig. 2.40 shows the required power and the resulting total ohmic losses. The dashed line shows the power and losses when the eddy current term is not taken into account. As can be seen, during acceleration, the eddy current losses cause extra ohmic losses, and during deceleration, the ohmic losses are lower due to the eddy current damping effect. This results in a very small increase of the mean ohmic losses of less than 1% to overcome the eddy current damping.

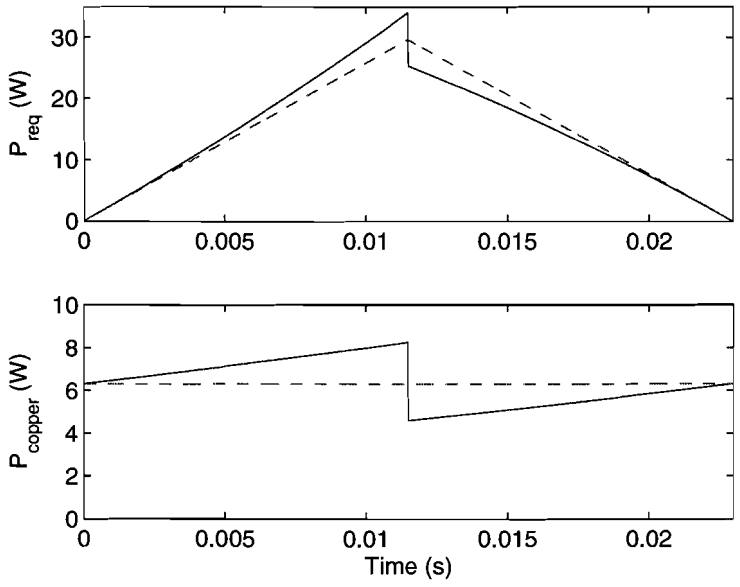

Figure 2.40: Mechanical power and ohmic loss power. The solid line shows the required power when eddy current damping is taken into account.

2.5 Final design

From the results of the previous sections, two designs are derived. A prototype of model (B) is being built and tested.

Table 2.9: Geometric parameters final design (A) quasi-Halbach topology, (B) axially magnetized topology.

Geometric parameter	Design A	Design B	Description
R_{out} (mm)	9.00	9.00	Outer radius
l_{stator} (mm)	1.00	1.00	Radial stator length
l_{coil} (mm)	1.75	1.75	Radial coil length
l_g (mm)	0.25	0.25	Radial airgap length
l_m (mm)	4.00	4.00	Radial magnet length
τ_p (mm)	8.33	8.33	Pole pitch
α_p	0.40	0.75	Radial to axial magnet ratio
l_{active} (mm)	100.00	100.00	Axial active length
l_{ax} (mm)	103.90	103.90	Axial armature length
$l_{translator}$ (mm)	144.39	144.39	Translator length

Table 2.10: Electrical parameters final design (A) quasi-Halbach topology, (B) axially magnetized topology.

Electric parameter	Design A	Design B	Description
N_{coils}	36	36	Number of coils
N_{turns}	39	39	Number of turns per coil
EMF (V)	10.7	11.2	Electro motive force @ 1 m/s
L_s (μH)	339	420	Total self inductance 12 coils
M_s (μH)	128	146	Total mutual inductance 12 coils
$\hat{I}_{max}$ (A)	2.3	2.4	Maximum phase current (41N)
$\hat{U}_{max}$ (V)	33.4	34.8	Maximum phase voltage (@1.8 m/s)

Chapter 3

Rotary actuator

As presented in the introduction, the 2-DoF system consists of a linear and a rotary actuator with one common translator. In the first part of this chapter, the existing rotary actuator in the placement module is analyzed. The analysis is focussed on the feasibility of solid back-iron instead of laminated back-iron from eddy current loss point of view.

In the second part of this chapter, a permanent magnet rotary is analyzed using semi-analytical equations, and a parametric search is performed to find optimal geometric parameters.

3.1 Currently used rotary actuator

In the current placement module, a two-pole slotless permanent magnet actuator as shown in Fig. 3.1 is used. The magnet in the actuator is parallel magnetized. The dimensions of the actuator are listed in Table 3.1.

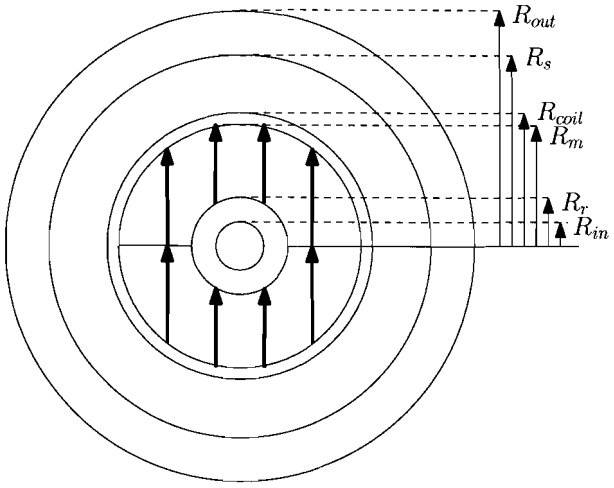

Figure 3.1: Geometry rotary actuator.

Table 3.1: Dimensions rotary actuator.

Parameter	22BS	Description
R_{in} (mm)	1.25	Inner radius
R_r (mm)	2.00	Rotor radius
R_m (mm)	5.25	Magnet radius
R_{coil} (mm)	5.50	Coil radius
R_s (mm)	6.95	Stator radius
R_{out} (mm)	8.75	Outer radius
l_{ax} (mm)	15.00	Axial length

In this section, the eddy current loss in this actuator is analyzed using a 2D FEA. The results are compared with measurements.

3.1.1 Eddy current losses

To decrease the costs of the rotary actuator, it can be beneficial to use solid steel instead of laminated steel. A major drawback of using solid steel for the back iron are the iron losses. The iron losses contains hysteresis losses, excess losses and eddy current losses. In solid steel, the eddy current losses are the most important. The current loop caused by the induced voltage will be much larger than in laminated back iron resulting in higher eddy current losses. The eddy currents will cause an extra heat source additional to the windings, and a damping torque T_{damp}.

The eddy current losses are proportional to frequency squared and flux density squared:

$$P_{eddy} \propto f^2 B^2, \tag{3.1}$$

where B is the flux density and f its frequency. As the maximum speed of the rotary actuator in this application is only 1200 rpm, i.e. 20Hz for a two pole machine, it can be feasible to use solid steel back iron.

3.1.2 Assumptions for eddy current calculations

To calculate the eddy current losses, the rotary actuator as described in Fig. 3.1 and Table 3.1 is used. Instead of using a non-conducting magnetic region in the FE package FLUX2D, a solid conductor region is assigned to the back iron. The magnetic properties are described by the BH-curve in Fig. 2.2b unless stated otherwise.

In order to simplify the modeling of the eddy-current loss within the 2D finite element (FE) analysis, the machine is assumed to be infinitely long. This means that instead of eddy-current loops, the induced currents are assumed to flow in the axial direction. This assumption is reasonable in brushless permanent magnet machines, where the axial length is much larger than the diameter. It needs noting that 2D, compared to 3D, FE modeling provides a total eddy-current loss that is overestimated, hence is a useful approximation due to its ease of implementation.

Eddy current losses occur in all conducting parts of the machine. In this section only eddy current losses in the back-iron are calculated as the major part of the losses arise here when solid steel is used. All simulations are performed at the maximum speed in this application. This is the worst case situation, the losses increase quadratically with the speed of the rotor therefore, the duty cycle has a big effect on the total losses.

Both simulations for eddy current losses at no-load and with current applied to the windings are performed. The conclusion from these simulations is that the extra eddy current losses caused by the armature reaction are negligible. Therefore, all results presented here are without taking into account the armature reaction.

3.1.3 Calculation method

As said before, the eddy current losses are calculated using 2D FEM. When a resistivity is given to the back-iron, and the rotor turns at a certain speed, a current is induced in the back-iron. Figure 3.2 shows the current density induced in the back-iron at 1200 rpm.

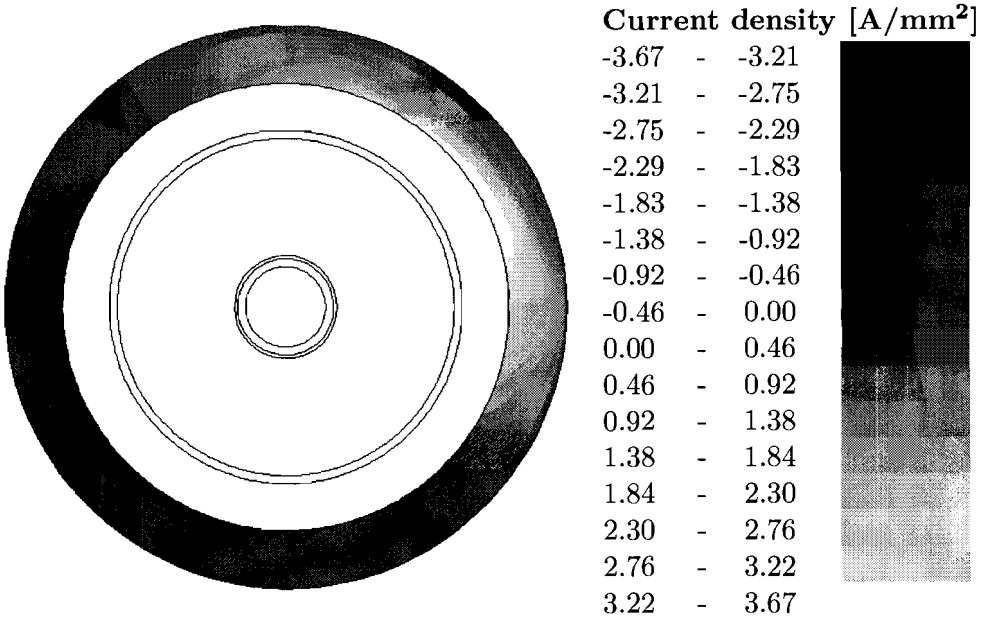

Figure 3.2: Induced current density in the back-iron of the adjusted 22BS. The back-iron has a resistivity $\rho = 1.4\text{x}10^{-7}$ Ωm. The rotor speed n is 1200 rpm.

To calculate the total losses, the back-iron is split into 20 rings. In each ring, the current density is assumed to be constant in the radial direction. Figure 3.3 shows the current density versus angle in the rings of the back-iron. The inner ring has the highest current density and the outer ring the lowest current density. The losses are calculated using the RMS value of the current density in one ring, integrated over the surface of that ring. This gives the total current flowing in the axial direction in each ring. The current through the ring squared times the resistivity of the ring gives the eddy current loss in each ring. The sum of all rings gives the total eddy current loss in the back-iron.

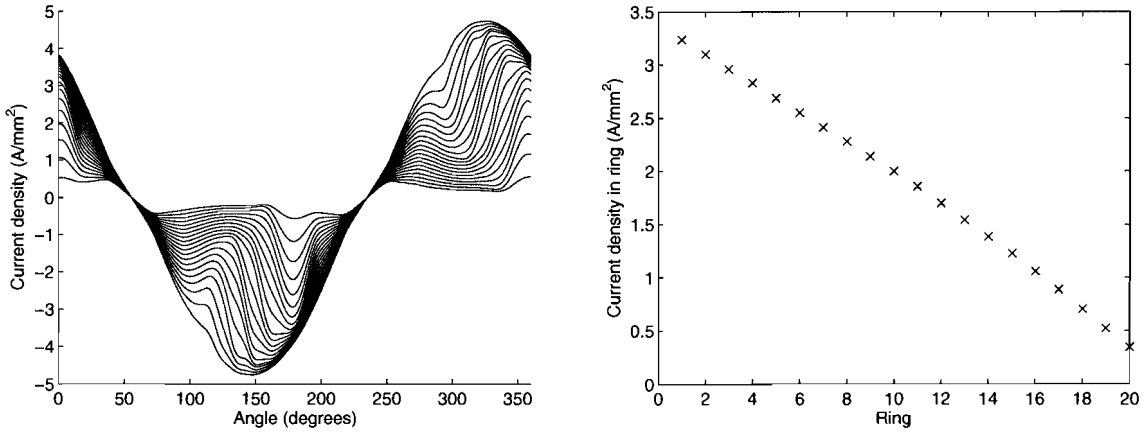

(a) (b)

Figure 3.3: Current density in the back-iron divided into 20 rings. The line indicating the lowest current density represents the outer ring of the back-iron, the line indicating the highest current density represents the inner ring of the back-iron. The current density waveform versus angle is shown in (a), the current density RMS value in each ring is shown in (b).

3.1.4 Resistivity of the solid steel back-iron

Table 3.2 shows the eddy current losses at no-load for different values of resistivity for solid steel. The resistivity is increased from 1.4x10^{-7} Ωm the resistivity of steel AI1010 (mild steel), up to 6.0x10^{-7} Ωm, the resistivity for improved electrical steels [27].

Table 3.2: Solid steel eddy current losses P_{eddy} and torque T_{damp} for different values of resistivity ρ. The torque is produced by the eddy-currents in the back-iron at no-load.

ρ (Ωm)	P_{eddy} (mW)	T_{damp} (Nmm)
1.4x10^{-7}	360	3.2
2.0x10^{-7}	252	2.4
3.0x10^{-7}	164	1.6
4.0x10^{-7}	121	1.2
5.0x10^{-7}	96	0.9
6.0x10^{-7}	80	0.8

Compared to the actuator power and torque, the eddy current losses are significant for a resistivity of 1.4x10^{-7} Ωm. The maximum torque for this application is

$$T_{total} = J_m\alpha + T_{friction} \tag{3.2}$$

where J_m is the inertia of the rotor and the load, α the maximum angular velocity and $T_{friction}$ the mechanical friction torque from the specifications provided by Assembléon. The load of the actuator is a nozzle and a component. The mass and inertia of this load are very small compared to the inertia and mass of the rotor and therefore neglected. For an inertia J_m of 5x10^{-7} kg m^2 and a peak acceleration α of 3500 rad/s^2, the total torque is:

$$T_{total} = 1.75mNm + 2.0mNm \tag{3.3}$$

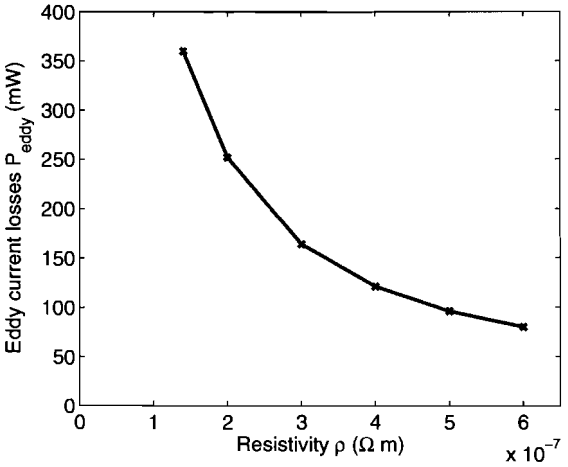

Figure 3.4: Solid steel eddy current losses P_{eddy} and torque T for various values of resistivity ρ.

And the maximum power of this application is

$$P_{max} = \omega_{max} T_{total} = 470mW \tag{3.4}$$

The mechanical power and torque for this application are in the same range as the eddy current losses in Table 3.2 for a low resistivity. Therefore, using solid steel back-iron is not feasible unless improved steel is used.

3.1.5 Different speed

As shown in Eq. (3.1), the eddy current losses are proportional to the frequency squared. Therefore, decreasing the speed of the actuator gives lower eddy current losses. Table 3.3 and Fig. 3.5 shows the eddy current losses versus the rotor speed n for a constant resistivity $\rho = 1.4\text{x}10^{-7}$ Ωm.

Table 3.3: Solid steel eddy current losses P_{eddy} at various speeds n for constant resistivity $\rho = 1.4\text{x}10^{-7}$ Ωm.

n (rpm)	P_{eddy} (mW)	T_{damp} (mNm)
400	37	1.1
600	85	1.6
800	150	2.2
1000	240	2.8
1200	**360**	**3.2**
1600	650	4.6

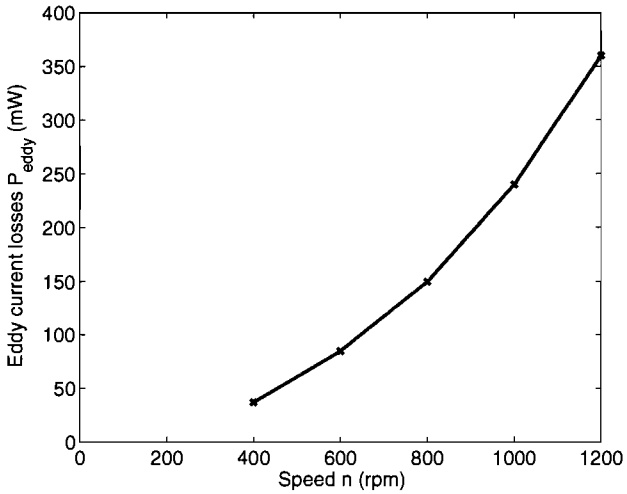

Figure 3.5: Solid steel eddy current losses P_{eddy} versus speed n for constant resistivity $\rho = 1.4\text{x}10^{-7}$ Ωm.

3.1.6 Lamination thickness

Table 3.4 shows the results of the eddy current losses P_{eddy} for various values of lamination thickness t and resistivity ρ at a constant speed of 1200 rpm. As can be concluded from Table 3.3, the iron losses decreases when laminated steel is used.

Table 3.4: Eddy current losses P_{eddy} for different values of lamination thickness t and resistivity ρ all at a constant speed of 1200 rpm.

t (mm)	$2\text{x}10^{-7}$ Ωm	$3\text{x}10^{-7}$ Ωm	$4\text{x}10^{-7}$ Ωm	$5\text{x}10^{-7}$ Ωm	$6\text{x}10^{-7}$ Ωm
0.35	2.4 mW	1.6 mW	1.2 mW	1.0 mW	0.8 mW
0.50	4.9 mW	3.3 mW	2.4 mW	1.9 mW	1.6 mW
0.65	8.3 mW	5.5 mW	4.1 mW	3.3 mW	2.7 mW

The original *22BS* actuator is designed for high speeds therefore, a simulation at rated speed of the *22BS* is made. The simulation is performed at 13000 rpm with a lamination thickness of 0.35 mm and a resistivity of $4\text{x}10^{-7}$ Ωm. The calculated eddy current losses are 94 mW.

3.1.7 Different material properties

One simulation is performed for a model with solid steel back-iron made of *Vacoflux 50*, a material with a high level of saturation (about 2 Tesla) and a resistivity of $4.4\text{x}10^{-7}$ Ωm. The simulation results in more eddy current losses. Due to the higher flux density in the iron, the eddy current losses are increased. However, the higher flux density results in a higher torque for the same current as well. Another disadvantage of using this material is the price, it is more expensive than steel AI1010.

3.1.8 Outer radius back iron

The influence of the outer radius is shown in Table 3.5. The eddy current losses increase for increasing outer radius. Due to the increasing outer radius, the flux density in the iron

Table 3.5: Solid steel eddy current losses P_{eddy} for different values of the outer radius, a constant resistivity equal to 4x10^{-7} Ωm, and a constant speed of 1200 rpm.

R_{out} (mm)	P_{eddy} (mW)	T_{damp} (mNm)
16.5	86	0.75
17.5	121	1.15
18.5	157	1.60
19.5	191	2.00

decreases, but the amount of iron increases quadratically. Therefore, the eddy current decreases, but the losses increases because the current flows through a larger amount of iron. The disadvantage of a smaller outer radius of the back-iron is the decrease of the flux density in the airgap which results in a lower torque.

This conclusion is a contradiction with the influence of the outer radius for machines with laminated steel. As can be seen in Table 3.6, the eddy current losses decrease in laminated steel when the outer radius of the motor increases.

Table 3.6: Laminated steel eddy current losses P_{eddy} for different values of outer radius, a constant resistivity equal to 4x10^{-7} Ωm, and a constant speed of 1200 rpm. The lamination thickness t is 0.50 mm.

R_{out} (mm)	P_{eddy} (mW)
16.5	2.1
17.5	2.4
18.5	2.4
19.5	2.1

3.1.9 Measurements

Measurements on a prototype of the adapted 22BS are performed by another company to validate the simulation results. The losses are measured by driving the rotary actuator by a DC motor. First, only the rotor of the rotary actuator is attached to the external DC motor to calculate the rotational losses of the DC-motor. At various speeds the current and voltage of the DC-motor are measured to calculate the losses. Now the same measurement is done with the DC-motor coupled to the rotor inside the solid steel stator. The difference between these losses are the iron losses in the adapted 22BS rotary actuator. The material properties of the back-iron in the measurements is not given. Therefore, the measurements can give different results than the simulations. To compare both results, it is assumed that the material used for the back-iron has the properties of AI1010, and a resistivity of 1.4x10^{-6}.

Table 3.7 gives the results from measurements. Figure 3.6 shows both the measured iron losses and the eddy current losses calculated from FE simulations. The measured iron losses include the hysteresis losses and excess losses which do not depend on the frequency squared but only frequency. Therefore the curve of the measurements is more linear. As can be seen,

Table 3.7: Measured solid steel iron losses P_{iron} at various speeds n.

n (rpm)	P_{eddy} (mW)	T_{damp} (mNm)
285	90	1.7
555	157	1.9
967	266	2.1
1190	346	2.3
1562	497	2.6

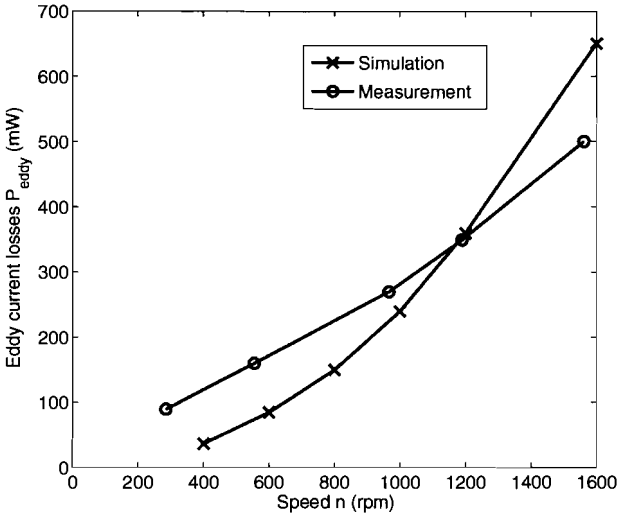

Figure 3.6: Measurements of iron losses and simulations of solid steel eddy current losses P_{eddy} versus speed n.

the simulations and the measurements are in the same order, the simulations give a good approximation of the losses in the back-iron

3.1.10 Conclusions

All conclusions are drawn for a constant speed of 1200 rpm.

- The eddy current losses in solid steel back-iron differ from 80 mW for a resistivity of $6.0\text{x}10^{-7}$ Ωm to 360 mW for a resistivity of $1.4\text{x}10^{-7}$. This is 17% up to 77% of the maximum mechanical power needed.
- The torque produced by the eddy currents differ from 20% up to 85% of the maximum required torque.
- For laminated steel, the eddy current losses are between 0.8 mW and 8.3 mW, depending on the lamination thickness and the resistivity.
- A smaller outer radius results in less eddy current losses but decreases the torque density as well.

The mechanical power and torque for this application are in the same range as the eddy current losses in Table 3.2 for a low resistivity. Therefore, using solid steel back-iron is not feasible unless improved steel is used.

3.2 Magnetic loading rotary actuator

In this section, general expressions are used to describe the magnetic field produced by the both radial and parallel magnetized magnets in slotless actuators having surface-mounted magnet rotors. [7, 3, 4] This type of actuator is particularly interesting for precision applications as it exhibits almost zero torque ripple due to the absence of slots [28]. These semi analytical equations are used to develop fast and accurate design tools for rotary actuators.

The field vectors $\vec{B}$ and $\vec{H}$ are coupled by

$$\vec{B}_I = \mu_0 \vec{H}_I \quad \text{in vacuum,} \tag{3.5}$$

and

$$\vec{B}_{II} = \mu_0 \mu_r \vec{H}_{II} + \mu_0 \vec{M} \quad \text{in permanent magnets,} \tag{3.6}$$

where $\vec{M}$ is the magnetization, μ_0 the permeability of vacuum, and μ_r is the relative permeability of the permanent magnet. For permanent magnets having a linear second-quadrant demagnetization characteristic, the amplitude of the magnetization vector $\vec{M}$ is

$$M = \frac{B_{rem}}{\mu_0}, \tag{3.7}$$

where B_{rem} is the remanent flux density of the permanent magnet. The direction of the magnetization $\vec{M}$ is different for radial and parallel magnetized permanent magnets as can be seen in Fig. 3.7. In polar coordinates, the direction of $\vec{M}$ is given by

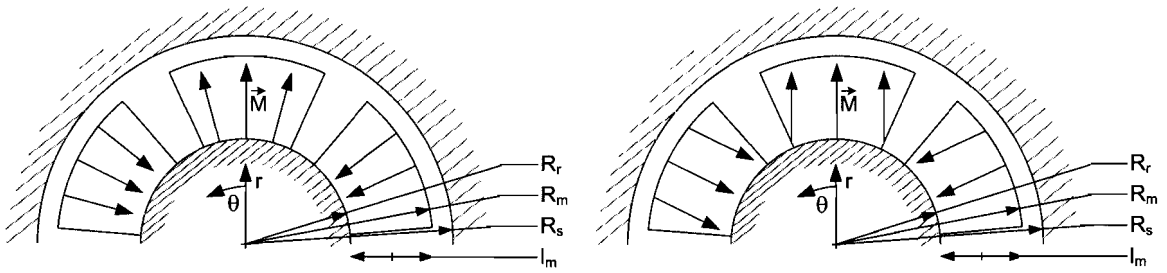

Figure 3.7: Magnetization in (a) radial magnetized permanent magnet (b) parallel magnetized permanent magnet actuator.

$$\vec{M} = M_r \vec{r} + M_\theta \vec{\theta}. \tag{3.8}$$

The components M_r and M_θ over one pole pair for both radial and parallel magnetized magnets can be described as Fourier series,

$$M_r = \sum_{n=1,3,5,\ldots}^{\infty} M_{rn} \cos(np\theta), \tag{3.9}$$

$$M_\theta = \sum_{n=1,3,5,\ldots}^{\infty} M_{\theta n} \sin(np\theta), \tag{3.10}$$

where for radial magnetization

$$M_{rn} = 2\frac{B_{rem}}{\mu_0}\alpha_p \frac{\sin\left(\frac{n\pi\alpha_p}{2}\right)}{\frac{n\pi\alpha_p}{2}}, \tag{3.11}$$

$$M_{\theta n} = 0, \tag{3.12}$$

and for parallel magnetization

$$M_{rn} = \frac{B_{rem}}{\mu_0}\alpha_p \left(d_{1n} + d_{2n}\right), \tag{3.13}$$

$$M_{\theta n} = \frac{B_{rem}}{\mu_0}\alpha_p \left(d_{1n} - d_{2n}\right) \tag{3.14}$$

$$, \tag{3.15}$$

where

$$d_{1n} = \frac{\sin\left[(np+1)\alpha_p\frac{\pi}{2p}\right]}{(np+1)\alpha_p\frac{\pi}{2p}} \quad \forall\ np, \tag{3.16}$$

$$d_{2n} = 1 \quad \text{for } np = 1, \tag{3.17}$$

$$d_{2n} = \frac{\sin\left[(np-1)\alpha_p\frac{\pi}{2p}\right]}{(np-1)\alpha_p\frac{\pi}{2p}} \quad \text{for } np \neq 1, \tag{3.18}$$

where α_p is the magnet pole-arc to pole-pitch ratio.

In order to obtain an analytical solution for the magnetic field distribution in the airgap and the magnets, the following assumptions are made:

1. The permanent magnets have a linear demagnetization characteristic, and are fully magnetized in the direction of magnetization.
2. The rotor is assumed to be infinitely long, the end effects are neglected
3. The stator and rotor back-iron are infinitely permeable.

To solve the magnetic field equations, the magnetic scalar potential, φ, is used here which is defined as

$$\vec{H} = -\nabla\varphi. \tag{3.19}$$

Combining (3.5), (3.6), (3.19) with Maxwell's equation leads to

$$\nabla^2\varphi_I = 0 \quad \text{in vacuum,} \tag{3.20}$$

$$\nabla^2\varphi_{II} = \frac{\nabla\cdot\vec{M}}{\mu_r} \quad \text{in the magnets.} \tag{3.21}$$

The (Laplacian) equation for the magnetic scalar potential in vacuum expressed in the polar coordinate system is

$$\frac{1}{r}\frac{\partial}{\partial r}\left(r\frac{\partial\varphi_I}{\partial r}\right) + \frac{1}{r^2}\frac{\partial^2\varphi_I}{\partial\theta^2} = 0. \tag{3.22}$$

The (quasi-Poissonian) equation for the magnetic scalar potential in magnets expressed in the polar coordinate system is

$$\frac{1}{r}\frac{\partial}{\partial r}\left(r\frac{\partial \varphi_{II}}{\partial r}\right)+\frac{1}{r^2}\frac{\partial^2 \varphi_{II}}{\partial \theta^2}=\frac{\nabla\cdot\vec{M}}{\mu_r}. \tag{3.23}$$

From (3.9) and (3.10)

$$\nabla\cdot\vec{M} = \frac{M_r}{r}+\frac{\partial M_r}{\partial r}+\frac{1}{r}\frac{\partial M_\theta}{\partial \theta} \tag{3.24}$$

$$= \sum_{n=1,3,5,..}^{\infty}\frac{1}{r}M_n\cos(np\theta), \tag{3.25}$$

where

$$M_n = M_{rn}+npM_{\theta n}. \tag{3.26}$$

General solutions for (3.22) and (3.23) are obtained from [4]

$$\varphi_I(r,\theta)=\sum_{n=1,3,5,..}^{\infty}\left(a_{n1}r^{np}+b_{n1}r^{-np}\right)\cos(np\theta), \tag{3.27}$$

in the airgap and

$$\varphi_{II}(r,\theta) = \sum_{n=1,3,5,..}^{\infty}\left(a_{n2}r^{np}+b_{n2}r^{-np}\right)\cos(np\theta) + \sum_{n=1,3,5,..}^{\infty}\frac{M_n}{\mu_r\left[1-(np)^2\right]}r\cos(np\theta), \tag{3.28}$$

for $np\neq 1$, and

$$\varphi_{II}(r,\theta)=\left(a_{12}r+b_{12}r^{-1}\right)\cos(\theta)+\frac{1}{2}\frac{M_1}{\mu_r}r\ln(r)\cos(\theta), \tag{3.29}$$

for $np=1$. The constant $a_{n1}, b_{n1}, a_{n2}, b_{n2}, a_{12}, b_{12}$ are found by applying the boundary conditions:

$$H_{\theta 1}(r,\theta)\big|_{r=R_s} = 0, \tag{3.30}$$

$$H_{\theta 2}(r,\theta)\big|_{r=R_r} = 0, \tag{3.31}$$

$$B_{r1}(r,\theta)\big|_{r=R_m} = B_{r2}(r,\theta)\big|_{r=R_m}, \tag{3.32}$$

$$H_{\theta 1}(r,\theta)\big|_{r=R_m} = H_{\theta 1}(r,\theta)\big|_{r=R_m}, \tag{3.33}$$

where the dimensions R_s, R_r, R_m are defined in Fig. 3.7. This gives with (3.19)

$$-\frac{1}{r}\frac{\partial\varphi_I}{\partial\theta}\bigg|_{r=R_s} = 0, \tag{3.34}$$

$$-\frac{1}{r}\frac{\partial\varphi_{II}}{\partial\theta}\bigg|_{r=R_r} = 0, \tag{3.35}$$

$$-\frac{\partial\varphi_{II}}{\partial\theta}\bigg|_{r=R_m} = -\mu_r\frac{\partial\varphi_{II}}{\partial\theta}\bigg|_{r=R_m} + \sum_{n=1,3,5,..}^{\infty} M_n\cos(np\theta), \tag{3.36}$$

$$-\frac{1}{r}\frac{\partial\varphi_I}{\partial\theta}\bigg|_{r=R_m} = -\frac{1}{r}\frac{\partial\varphi_{II}}{\partial\theta}\bigg|_{r=R_m}. \tag{3.37}$$

Using Mathematica, the complete solutions for the $\vec{r}$ and $\vec{\theta}$ component of the flux density in the airgap are equations:

$$B_{r1}(r,\theta) = \sum_{n=1,3,5,..}^{\infty} K_B(n) f_{B_r}(r)\cos(np\theta), \tag{3.38}$$

$$B_{\theta 1}(r,\theta) = \sum_{n=1,3,5,..}^{\infty} K_B(n) f_{B_\theta}(r)\sin(np\theta), \tag{3.39}$$

where for $np = 1$

$$K_B(n) = \frac{\mu_0 M_n}{2\mu_r}\left\{\frac{d_{3n}\left(\frac{R_m}{R_s}\right)^2 - d_{3n}\left(\frac{R_r}{R_s}\right)^2 + \left(\frac{R_r}{R_s}\right)^2\ln\left(\frac{R_m}{R_r}\right)^2}{\frac{\mu_r+1}{\mu_r}\left[1-\left(\frac{R_r}{R_s}\right)^2\right] - \frac{\mu_r-1}{\mu_r}\left[\left(\frac{R_m}{R_s}\right)^2 - \left(\frac{R_r}{R_m}\right)^2\right]}\right\}, \tag{3.40}$$

$$f_{B_r}(r) = 1 + \left(\frac{R_s}{r}\right)^2, \tag{3.41}$$

$$f_{B_\theta}(r) = -1 + \left(\frac{R_s}{r}\right)^2, \tag{3.42}$$

$$d_{3n} = \begin{cases} 2\frac{M_{r1}}{M_1} + 1 & \text{for parallel magnetization} \\ 1 & \text{for radial magnetization} \end{cases} \tag{3.43}$$

When $np \neq 1$,

$$K_B(n) = \frac{\mu_0 M_n}{2\mu_r}\frac{np}{(np)^2-1}\left\{\frac{(d_{3n}-1) + 2\left(\frac{R_r}{R_m}\right)^{np+1} - (d_{3n}+1)\left(\frac{R_r}{R_m}\right)^{2np}}{\frac{\mu_r+1}{\mu_r}\left[1-\left(\frac{R_r}{R_s}\right)^{2np}\right] - \frac{\mu_r-1}{\mu_r}\left[\left(\frac{R_m}{R_s}\right)^{2np} - \left(\frac{R_r}{R_m}\right)^{2np}\right]}\right\}, \tag{3.44}$$

$$f_{B_r}(r) = \left(\frac{r}{R_s}\right)^{np-1}\left(\frac{R_m}{R_s}\right)^{np+1} + \left(\frac{R_m}{r}\right)^{np+1}, \tag{3.45}$$

$$f_{B_\theta}(r) = -\left(\frac{r}{R_s}\right)^{np-1}\left(\frac{R_m}{R_s}\right)^{np+1} + \left(\frac{R_m}{r}\right)^{np+1}, \tag{3.46}$$

$$d_{3n} = \begin{cases} \left(np - \frac{1}{np}\right)\frac{M_{rn}}{M_n} + \frac{1}{np} & \text{for parallel magnetization} \\ np & \text{for radial magnetization} \end{cases}. \tag{3.47}$$

3.2.1 Parametric search magnetic loading theta-actuator

The equations derived in the previous section, (3.38) and (3.39), are implemented in Matlab to calculate the flux density in the airgap. The results of both models are compared to results of a FEA and show very good agreement as can be seen in Fig. 3.8. In this section is started

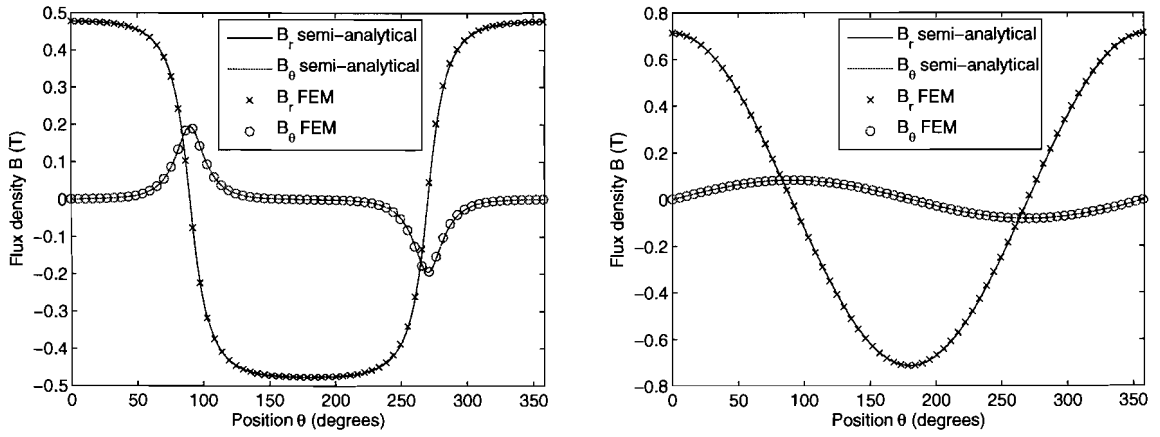

Figure 3.8: Flux density calculated in the middle of the coil for an actuator having one pole pair of (a) radially magnetized magnets, and (b) parallel magnetized magnets.

to design the rotary part of rotary-linear system. The torque of the rotary actuator can be expressed by rudimental equations for an initial sizing. The load of the rotary actuator is

$$T_{load} = J_m \alpha, \tag{3.48}$$

where α is the angular acceleration, and J_m is the moment of inertia of the translator and the load. As the load is only a very small SMD, this component is neglected. The translator can be described as a cylinder, which has an inertia

$$J_m = mR^2, \tag{3.49}$$

where R is the radius of the translator, and m is the mass of the translator

$$m \propto R^2. \tag{3.50}$$

The produced torque of the actuator can be expressed as

$$T_{actuator} = \frac{\pi D_g^2 L B_g Q}{2}, \tag{3.51}$$

where B_g is the magnetic loading in the airgap, Q the electric loading, D_g the airgap diameter, and L the axial length of the actuator. Therefore, a translator with a small radius is favorable as the load torque is

$$T_{load} \propto R^4, \tag{3.52}$$

and the actuator torque is

$$T_{actuator} \propto R^2. \tag{3.53}$$

This is the same conclusion as presented in the introduction of the linear actuator. Therefore, the geometric parameters of the tubular actuator presented in Table 2.9 are used as initial values for the parametric search.

3.2.2 Magnet length versus flux density

Using Matlab, the mean value and the peak value of the flux density in the middle of the coil for an actuator with one pole-pair is calculated. This calculation is performed for different values of magnet length, l_m, while the outer radius of the magnets is fixed, the geometric parameters of this analysis are shown in Table 3.8. This implies that the rotor radius, R_r,

Table 3.8: Geometric parameters of rotary actuator for analysis.

Geometric parameter	Value	Description
R_{out} (mm)	9.00	Outer radius
l_{stator} (mm)	1.00	Radial stator length
l_{coil} (mm)	1.75	Radial coil length
l_g (mm)	0.25	Radial airgap length
R_m (mm)	6.00	Magnet radius
α_p	1.00	Magnet to pole pitch ratio
p	1	Number of pole pairs

changes. In Fig. 3.9, the results are plotted for both radial and parallel magnetized magnets. As the modeled magnets have a relative permeability close to 1, the internal reluctance of

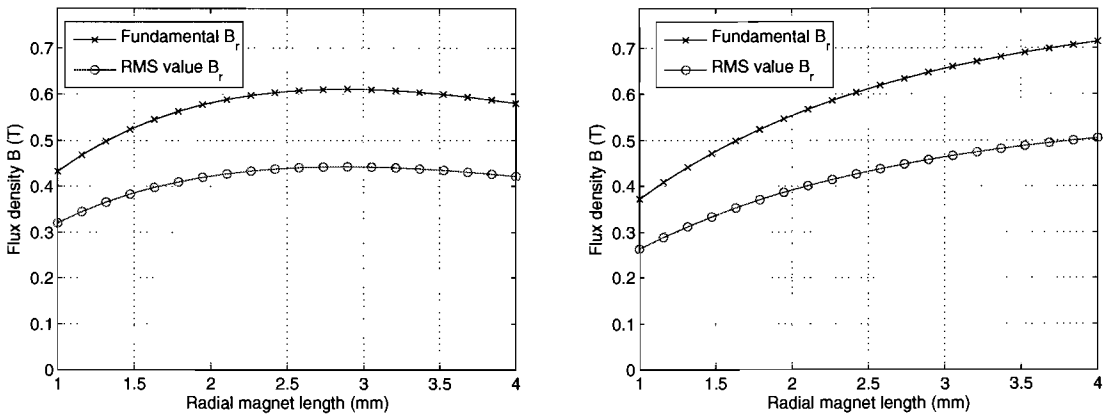

Figure 3.9: Radial component of the flux density in the middle of the coil versus magnet length, l_m, for an actuator with (a) radially magnetized magnets (b) parallel magnetized magnets. Both the peak value of the fundamental of the flux density and the RMS value are shown.

magnet becomes larger when the magnet length increases. Therefore, increasing the magnet length does not imply a linear increase of flux density in the coil.

As can be seen in Fig. 3.9, for radial magnetization there is an optimum magnet length while for the parallel magnetization the maximum flux density is reached at the maximum magnet length possible for this magnet radius. Reduction of the radial magnet length has the extra advantage of a decreasing translator mass.

3.2.3 Flux density in the armature

In the previous section, the flux density is calculated for several values of magnet length for one pole pair. The effect of saturation of the armature is not taken into account. As the geometry of the theta-actuator is slot-less, it is easy to make a good approximation of the maximum flux density in the armature

$$\hat{B}_{arm} = \hat{B}_{R_s} \frac{\pi R_s}{2pl_s}, \tag{3.54}$$

where $\hat{B}_{R_s}$ is the peak flux density at $r = R_s$, and p is the number of pole-pairs and l_s is the radial stator length. As can be seen, increasing the number of pole pairs or the radial stator length result in a lower flux density in the armature. However, increasing the number of pole pairs results in a lower magnetic flux density in the coil as well. Fig. 3.10a and 3.10b shows the influence of the number of pole pairs on the flux density in the armature and in the center of the coil. The flux density is calculated for the model as given in Table 3.8 with a magnet length optimized for the highest flux density in the coil. The flux density in the stator is

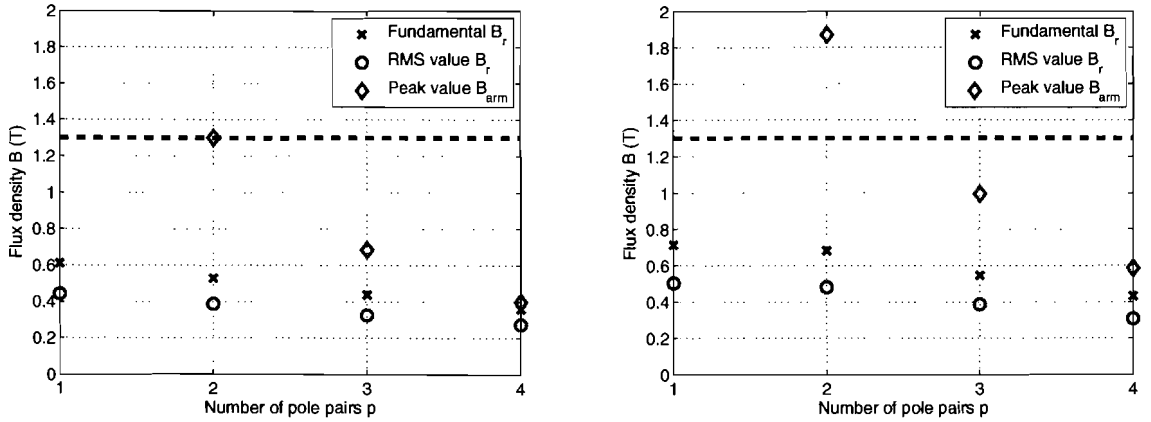

Figure 3.10: Flux density in the center of the coil and in the armature for several number of pole pairs. (a) Shows the results for radially magnetized magnets and (b) the results for parallel magnetized magnets.

limited at 1.3 T to prevent errors in the analytical model due to saturation. Although the higher number of pole pairs can prevent saturation in the armature, the eddy current losses in the armature will increase due to the increased frequency of the flux density. Therefore, both eddy current losses and saturation have to be taken into account by choosing the number of pole pairs.

3.3 Electrical loading

Several winding topologies can be used in the rotary actuator. However, in this researched a simple full-pitch three phase winding as shown in Fig. 3.11 is used to calculate the torque. The torque is calculated using the Lorentz force equation as described in Section 2.3.1. The

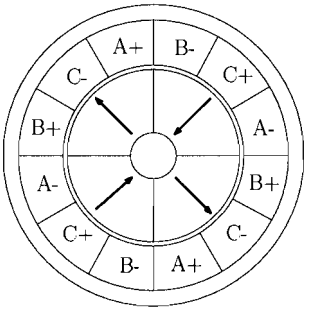

Figure 3.11: Full pitch three phase winding arrangement.

same method is applied to this actuator to calculate the force on the windings. Consequently, the torque can be calculated by

$$\vec{T} = \vec{r} \times \vec{F}. \tag{3.55}$$

3.3.1 Thermal model

The semi-analytical model derived in the previous section is combined with equations describing the thermal behavior. The assumptions for the thermal model are the same as in the previous section, the coil region and the armature are perfect heat conductors and all the heat is removed from the actuator via the armature. The heat produced by eddy currents is neglected, only copper losses are taken into account

$$P_{Cu} = I_{coil}^2 R_{coil}, \tag{3.56}$$

where I_{coil} is the coil current defined by

$$I_{coil} = \frac{J_{RMS}\pi \left(R_s^2 - R_{coil}^2\right)}{N_{turns}}, \tag{3.57}$$

and R_{coil} is the coil resistance per axial length,

$$R_{coil} = \rho_{Cu} \frac{N_{turns}}{\pi \left(R_s^2 - R_{coil}^2\right) \frac{1}{N_{turns}} k_p}. \tag{3.58}$$

This results in

$$P_{Cu} = J_{RMS}^2 \pi \left(R_s^2 - R_{coil}^2\right) \rho_{Cu} \frac{1}{k_p}. \tag{3.59}$$

Using the assumptions mentioned before, the temperature difference between the armature and the ambient (ΔT) is

$$\Delta T = P_{Cu} \frac{1}{h 2\pi R_{out}} D, \tag{3.60}$$

where h is the heat transfer coefficient, and D is the duty cycle.

3.3.2 Torque

First the torque of the parallel magnetized topology is calculated for a constant current density for several number of pole pairs. The geometric parameters are shown in Table. 3.9 and the results are depicted in Fig. 3.12. As can be seen, a higher number of pole pairs results in a

Table 3.9: Geometric parameters of rotary actuator for analysis.

Geometric parameter	Value	Description
R_{out} (mm)	9.00	Outer radius
l_{stator} (mm)	1.00	Radial stator length
l_{coil} (mm)	1.75	Radial coil length
l_g (mm)	0.25	Radial airgap length
R_m (mm)	6.00	Magnet radius
l_{ax} (mm)	15.00	Axial length
α_p	1.00	Magnet to pole pitch ratio

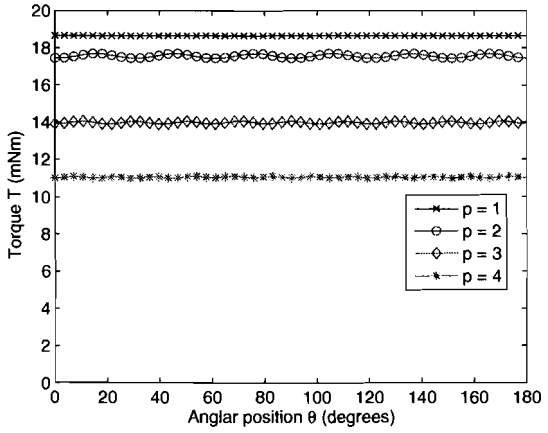

Figure 3.12: Torque, T, versus number of pole pairs, p, for the parallel magnetized topology. The torque is calculated for a current density of $J_{RMS} = 4.5$ A/mm^2, and an axial lenghth of $l_{ax} = 15$ mm.

decrease of the torque. However, to avoid saturation for a small number of poles can only be obtained by a larger radial stator length, which will consequently result in less torque.

As the radial coil length used in the previous calculations is the same as for the tubular actuator and not optimized, a second analysis is performed to find the optimal coil length. One model is created to calculate the optima for a constant ΔT, where the results are shown in Fig. 3.13. In a second model, the current density is varied to maintain constant copper losses. The results of this calculation are shown in Fig. 3.14. As can be seen in Fig. 3.13, for $p = 1$ and $p = 2$, the coil length has no optimum for $l_{coil} < 4.5$mm. In general, the optimal coil length decreases with the number of pole pairs, mainly because the magnetic flux density decays faster within the airgap [29]. This is valid for both models as shown in Fig. 3.13, and Fig. 3.14.

However, as the outer radius, R_{out} has an upper limit, and R_m is chosen to be the same

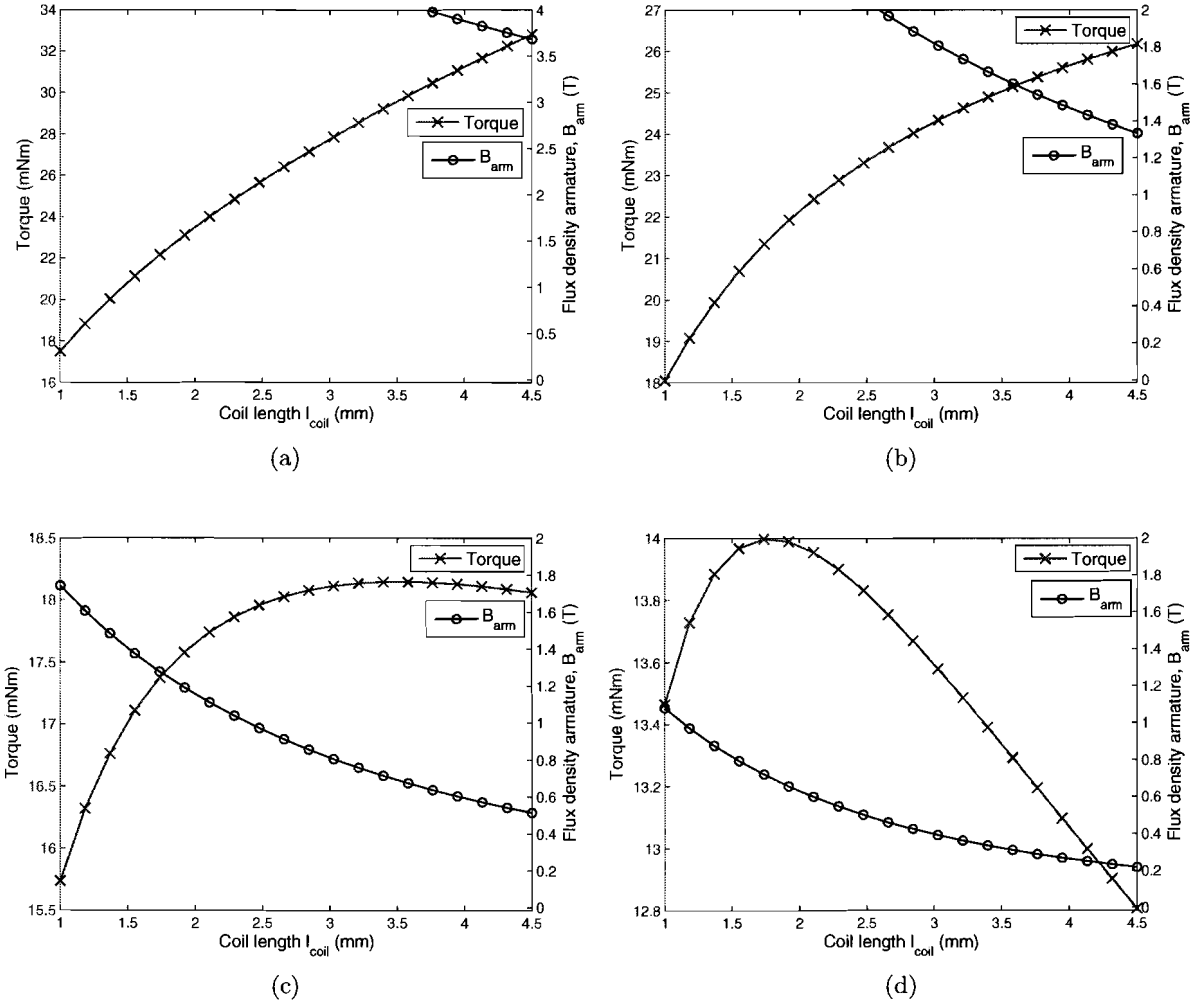

Figure 3.13: Torque and flux density in the armature calculated for several values of coil length, l_{coil}. The current density is varied to maintain $\Delta T = 40°C$ for $h = 10$ $Wm^{-2}K^{-1}$. (a) one pole pair, $p = 1$, (b) $p = 2$, (c) $p = 3$, (d) $p = 4$.

for the rotary and linear actuator, the optimum l_{coil} cannot be selected for $p < 4$. The best performance, without saturation in the armature, is achieved for $p = 3$ and $l_{coil} = 1.75$ mm.

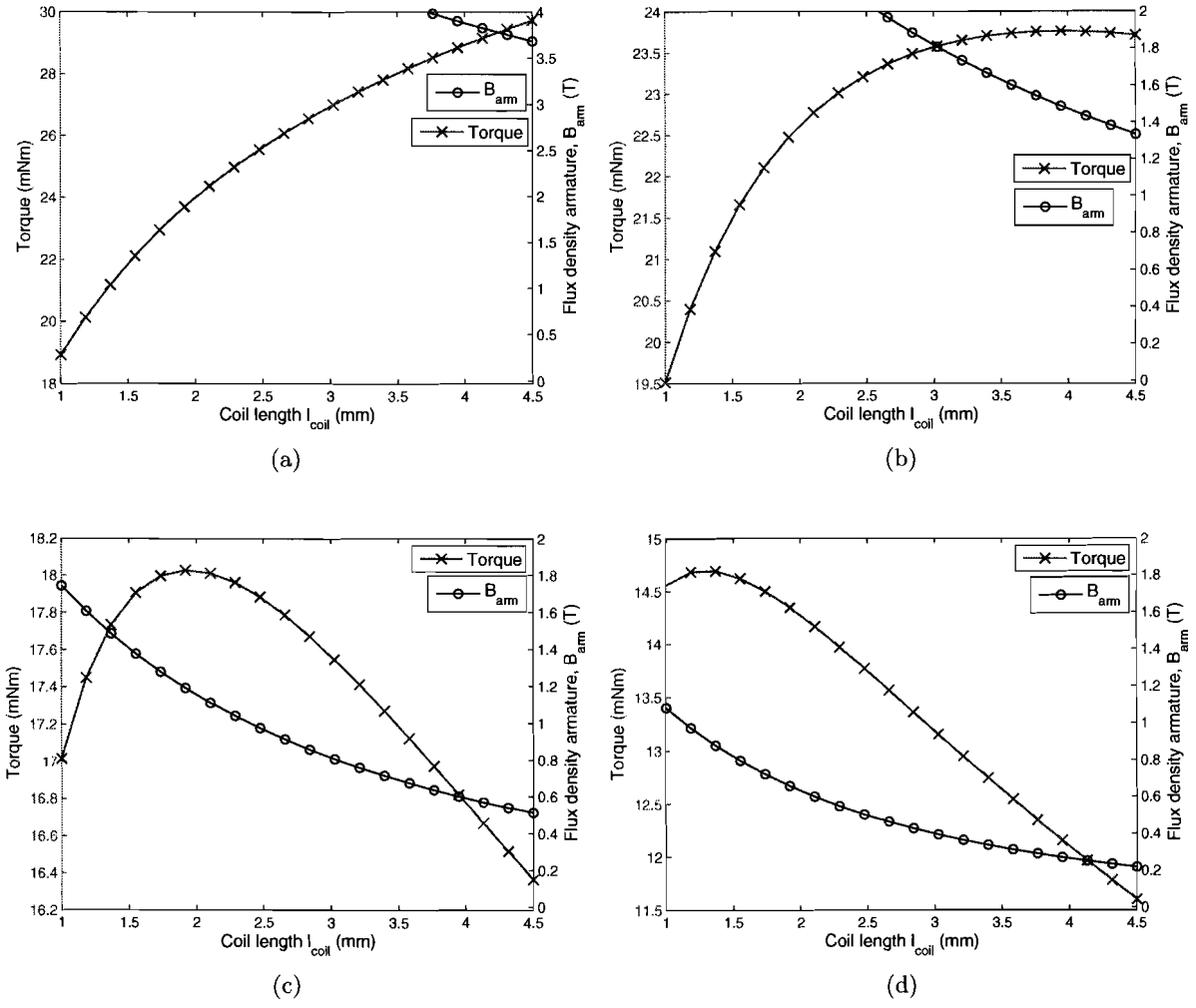

Figure 3.14: Torque and flux density in the armature calculated for several values of coil length, l_{coil}. The current density is varied to maintain a constant copper loss. (a) one pole pair, $p = 1$, (b) $p = 2$, (c) $p = 3$, (d) $p = 4$.

Note that increasing the stator length will allow a lower number of pole pairs and possibly higher performance with a smaller coil length. A more extensive analysis is required to create a final design.

3.4 Conclusions

In the first part of this chapter, the eddy-current losses in the existing rotary actuator are calculated and compared with measurements. The results show that a solid steel back-iron results in a damping torque as large as the load torque. Therefore, using solid steel back-iron is not feasible unless improved steel is used.

In the second part, semi-analytical models are presented for two topologies of slotless

rotary actuators, i.e. a radially magnetized rotor and a parallel magnetized rotor. A parametric search on geometric parameter is performed to investigate the effect of varying the number of pole pairs and the radial coil length. The parallel magnetized topology shows better performance, and the requirements of the system can be met without forced cooling.

Although the magnetic loading and electrical for the rotary actuator are calculated, more research on e.g. losses is required to present a design. As the models presented in this Chapter have a soft-magnetic core, which has a significant mass, it can be interesting to investigate the performance when a non-magnetic core is applied. Due to the limited time for this research, this is not included in this research.

Conclusions and recommendations

Conclusions

In this thesis, the multi-physical analysis and design of a linear and a rotary actuator is presented to apply in a rotary-linear motion system. Both the linear and rotary actuator are designed as two separated actuators with one common translator for P&P applications. In this application, very high linear acceleration is required. Therefore, this research is mainly focussed on the linear part of the system by means of the design of a tubular permanent magnet actuator.

In the first part, slotless tubular permanent magnet actuators with different translator topologies are investigated. A novel unified mathematical description of the magnetic field in the form of semi-analytical equations is proposed for the different researched topologies. The semi-analytical mathematical field description is obtained by applying sets of axisymmetric boundary conditions to the general field equations in the different regions of the actuator. The boundary conditions depend on the permanent magnet structure, the material of the different regions, and the magnetization pattern of the actuator. The advantage of this semi-analytical description is the time-efficient and accurate prediction of the magnetic fields in the actuator which can be used for both design and control.

The unified electro-magnetic models are implemented and coupled with multi-physical models describing electrical and thermal behavior resulting in a time-efficient analysis tool. Using these models, an extensive analysis is performed to synthesize the best structure according to the requested motion profiles and highest acceleration.

The axially magnetized topology and the quasi-Halbach topology with non-magnetic core show the best performance in terms of acceleration. The highest acceleration is achieved when the translator has a very small radius. The quasi-Halbach topology shows the highest acceleration capability. However, the axially magnetized topology is favorable from manufacturing point of view.

To validate the models used in this analysis, a prototype of the axially magnetized topology is being built and tested.

The second part of this research concerns the analysis of the rotary part of the system. As preliminary study, the eddy current losses in the currently used rotary actuator are investigated using FEA and measurements, considering solid steel back-iron. The damping torque created by the eddy-currents is observed to be as high as the required propulsion torque. Therefore, using solid steel back-iron is only feasible when improved steel or lamination is used.

An initial research has been made to design the rotary actuator for the 2-DoF system. As for the linear actuator, semi-analytical models are derived for two rotor topologies of a rotary

slotless permanent magnet actuator, i.e. a radially magnetized rotor and a parallel magnetized rotor. A parametric search on the magnetic loading of both topologies is performed based on the dimensions of the final design of the linear actuator.

The magnetostatic models are extended with thermal models and the Lorentz force equation to calculate the torque performance The parallel magnetized topology shows the best performance in terms of maximum torque.

Recommendations

This research is a preparation on a future PhD-project, Integrated Electromechanical Actuator. In this project, the aim is to design a 2-DoF single-body actuator where both linear motion and rotation are realized by one stator and one translator.

In the semi-analytical models of the TPMA, axial symmetry is used which implies no possibility to include axial end-effects. However, in practice, these end-effects can be significant. By means of additional axial boundary conditions, it is possible to include these end-effects in a semi-analytical model. This derivation will be a point of consideration in future work.

The semi-analytical models of the rotary actuator describe a rotor with a soft-magnetic core, with a significant mass density. In order to decrease the mass of the complete translator, a non-magnetic core, e.g. an aluminium core, can be favorable, albeit that the magnetic loading will decrease as well. In an additional analysis with models of such actuators, the effect can be investigated.

In order to have a design tool for a 2-DoF system with certain requirements, it is necessary to couple the models of the rotary and linear actuator in one model. Due to the limited time of the MSc. project, this tool is not developed in this research. As this work is mainly focussed on the magneto-static analysis, no mechanical and transient behavior is considered. However, for high acceleration levels, these mechanical stresses can become a dominant design constraint. Additional research is required to investigate these phenomena.

References

[1] J. Wang, G. W. Jewell, and D. Howe, "A general framework for the analysis and design of tubular linear permanent magnet machines," *IEEE Transactions on Magnetics*, vol. 35, pp. 1986–2000, May 1999.

[2] K. Halbach, "Design of permanent multipole magnets with oriented rare earth cobalt material," *Nuclear Instruments and Methods*, vol. 69, no. 1, pp. 1–10, 1980.

[3] Z. Q. Zhu, D. Howe, and C. C. Chan, "Improved analytical model for predicting the magnetic field distribution in brushless permanent-magnet machines," *IEEE Transactions on Magnetics*, vol. 38, pp. 229–238, January 2001.

[4] Z. Q. Zhu, D. Howe, E. Bolte, and B. Ackermann, "Instantaneous magnetic field distribution in brushless permanent magnet dc motors, part I: Open-circuit field," *IEEE Transactions on Magnetics*, vol. 29, pp. 124–135, January 1993.

[5] J. Mallinson, "One-sided fluxes - a magnetic curiosity?," *IEEE Transactions on Magnetics*, vol. 9, pp. 678–682, December 1973.

[6] J. Wang and D. Howe, "Tubular modular permanent-magnet machines equipped with quasi-Halbach magnetized magnets - part I: Magnetic field distribution, emf, and thrust force," *IEEE Transactions on Magnetics*, vol. 41, pp. 2470–2478, September 2005.

[7] E. P. Furlani, *Permanent Magnet and Electromechanical Devices.* Academic Press, 2001.

[8] D. C. Hanselman, *Brushless Permanent-Magnet Motor Design.* McGraw-Hill, 1994.

[9] J. R. Hendershot and T. J. E. Miller, *Design Of Brushless Permanent-Magnet Motors.* Magna Physics Publishing and Clarendon Press, 1994.

[10] M. McCaig and A. G. Clegg, *Permanent Magnets in Theory and Practice.* Pentech Press, 1987.

[11] B. L. J. Gysen, "Analytical and numerical framework for extensice electromagnetic analysis of tubular permanent magnet actuators," Master's thesis, Eindhoven University of Technology, 2007.

[12] Coleman, W. Conrad, and Whittier, "Linear and rotary actuator." U.S. Patent 4,607,197, IMC Magnetics Corporation, September 1986.

[13] Y. Sato, "Development of a 2-degree-of-freedom rotational/linear switched reluctance motor," *IEEE Transactions on Magnetics*, vol. 43, pp. 2564–2566, June 2007.

[14] T. Onuki, W. J. Jeon, and M. Tanabiki, "Induction motor with helical motion by phase control," *IEEE Transactions on Magnetics*, vol. 33, pp. 4218–4220, September 1997.

[15] M. Rabiee and J. J. Cathey, "Verification of a field therory analysis applied to a helical motion induction motor," *IEEE Transactions on Magnetics*, vol. 24, pp. 2125–2132, July 1988.

[16] P. de Wit, J. van Dijk, T. Blomer, and P. Rutgers, "Mechatronic design of a z-ϕ induction actuator," *International Conference on Electrical Machines and Drives*, vol. 44, pp. 279–283, September 1997.

[17] G. L. Swift, "Rotary-linear actuator system method of manufacturing and method of using a rotary-linear actuator." U.S. Patent 6,798,087, Anorad Corporation, September 2004.

[18] A. Chitayat, "Rotary-linear actuator." U.S. Patent 5,982,053, Anorad Corporation, October 1998.

[19] J. M. A. M. van Geel, J. C. Compter, and V. Kessler, "Electromagnetic actuator having a cylindrical translation coil and a toroidal rotation coil, actuator unit comprising the actuator and a measurement system, and machine comprising the actuator or the actuator unit." U.S. Patent 5,600,189, U.S. Philips Corporation, July 1995.

[20] M. K. Liebman, *Rotary-Linear Axes for High Speed Machining.* PhD thesis, Massachusetts Institute of Technology, September 2001.

[21] M. R. Sogard, "Two-dimensional electric motor." U.S. Patent 6,455,956, Nikon Corporation, September 2002.

[22] N. Bianchi, S. Bolognani, and D. D. Corte, "Tubular linear permanent magnet motors: An overall comparison," *IEEE Transactions on Industry Applications*, vol. 39, pp. 466–475, March 2003.

[23] L. Encica, *Space-mapping based design strategies applied to novel automotive electromagnetic suspension systems.* PhD thesis, Eindhoven University of Technology, to be published in 2008.

[24] J. Wang, D. Howe, and G. W. Jewell, "Fringing in tubular permanent-magnet machines: Part II. cogging force and its minimization," *IEEE Transactions on Magnetics*, vol. 39, pp. 3517–3522, November 2003.

[25] J. Wang, M. Inoue, Y. Amara, and D. Howe, "Cogging-force-reduction techniques for linear permanent-magnet machines," *IEE Proc-Electr. Power Appl.*, vol. 152, pp. 731–739, May 2005.

[26] Z. Q. Zhu, Z. P. Xia, D. Howe, and P. H. Mellor, "Reduction of cogging force in slotless linear permanent magnet motors," *IEE Proc-Electr. Power Appl.,*, vol. 144, pp. 277–283, July 1997.

[27] Surahammars Bruk, www.sura.se, *Non-oriented fully processed electrical steels.*

[28] T. S. Low, M. A. Jabbar, and T. S. Tan, "Design aspects and performance of a slotless pm motor for hard disk drives," *Industry Applications Magazine, IEEE*, vol. 3, pp. 43–51, Nov-Dec 1997.

[29] J. Ofori-Tenkorrang and J. H. Lang, "A comparative analysis of torque production in halbach and conventional surface-mounted permanent-magnet synchronous motors," *Industry Applications Conference, 1995. Thirtieth IAS Annual Meeting, IAS '95., Conference Record of the 1995 IEEE*, vol. 1, pp. 657–663, Oct 1995.

Appendix A

Fourier

Consider two arbitrary functions $F(z)$ and $G(z)$ which can be written as a Fourier series with a fundamental period of T and L respectively

$$F(z) = \sum_{n=1}^{\infty} \left[K_{cn} \cos\left(\frac{n2\pi z}{T}\right) + K_{sn} \sin\left(\frac{n2\pi z}{T}\right) \right], \tag{A.1}$$

$$G(z) = \sum_{m=1}^{\infty} \left[P_{cm} \cos\left(\frac{m2\pi z}{L}\right) + P_{sm} \sin\left(\frac{m2\pi z}{L}\right) \right], \tag{A.2}$$

where the Fourier coefficients can be calculated as

$$K_{cn} = \frac{2}{T} \int_{-T/2}^{T/2} F(z) \cos\left(\frac{n2\pi z}{T}\right) dz, \tag{A.3}$$

$$K_{sn} = \frac{2}{T} \int_{-T/2}^{T/2} F(z) \sin\left(\frac{n2\pi z}{T}\right) dz, \tag{A.4}$$

$$P_{cm} = \frac{2}{L} \int_{-L/2}^{L/2} G(z) \cos\left(\frac{m2\pi z}{L}\right) dz, \tag{A.5}$$

$$P_{sm} = \frac{2}{L} \int_{-L/2}^{L/2} G(z) \sin\left(\frac{m2\pi z}{L}\right) dz. \tag{A.6}$$

In the case that $F(z)$ should equal $G(z)$, it is possible to write the fourier coefficients of

$F(z)$ as function of the coefficients of $G(z)$ given by

$$K_{cn} = \frac{2}{T}\int_{-T/2}^{T/2} F(z)\cos\left(\frac{n2\pi z}{T}\right)dz, \tag{A.7}$$

$$\Downarrow$$

$$K_{cn} = \frac{2}{T}\int_{-T/2}^{T/2} G(z)\cos\left(\frac{n2\pi z}{T}\right)dz, \tag{A.8}$$

$$\Downarrow$$

$$K_{cn} = \frac{2}{T}\int_{-T/2}^{T/2} \sum_{m=1}^{\infty}\left[P_{cm}\cos\left(\frac{m2\pi z}{L}\right) + P_{sm}\sin\left(\frac{m2\pi z}{L}\right)\right]\cos\left(\frac{n2\pi z}{T}\right)dz, \tag{A.9}$$

$$\Downarrow$$

$$K_{cn} = \sum_{m=1}^{\infty}\left[\frac{2}{T}P_{cm}\int_{-T/2}^{T/2}\cos\left(\frac{m2\pi z}{L}\right)\cos\left(\frac{n2\pi z}{T}\right)dz \right. \tag{A.10}$$

$$\left. + \frac{2}{T}P_{sm}\int_{-T/2}^{T/2}\sin\left(\frac{m2\pi z}{L}\right)\cos\left(\frac{n2\pi z}{T}\right)dz\right], \tag{A.11}$$

$$\Downarrow$$

$$K_{cn} = \sum_{m=1}^{\infty}\Big[P_{cm}\eta_c(m,n) + P_{sm}\eta_s(m,n)\Big], \tag{A.12}$$

where $\eta_c(m,n)$ and $\eta_s(m,n)$ are defined as

$$\eta_c(m,n) = \frac{2}{T}\int_{-T/2}^{T/2}\cos\left(\frac{m2\pi z}{L}\right)\cos\left(\frac{n2\pi z}{T}\right)dz, \tag{A.13}$$

$$\eta_s(m,n) = \frac{2}{T}\int_{-T/2}^{T/2}\sin\left(\frac{m2\pi z}{L}\right)\cos\left(\frac{n2\pi z}{T}\right)dz, \tag{A.14}$$

and in the same way all K_{sn} can be written in terms of P_{cm} and P_{sm} given by

$$K_{sn} = \frac{2}{T}\int_{-T/2}^{T/2} F(z)\sin\left(\frac{n2\pi z}{T}\right)dz, \tag{A.15}$$

$$\Downarrow$$

$$K_{sn} = \frac{2}{T}\int_{-T/2}^{T/2} G(z)\sin\left(\frac{n2\pi z}{T}\right)dz, \tag{A.16}$$

$$\Downarrow$$

$$K_{sn} = \frac{2}{T}\int_{-T/2}^{T/2}\sum_{m=1}^{\infty}\left[P_{cm}\cos\left(\frac{m2\pi z}{L}\right)+P_{sm}\sin\left(\frac{m2\pi z}{L}\right)\right]\sin\left(\frac{n2\pi z}{T}\right)dz, \tag{A.17}$$

$$\Downarrow$$

$$K_{sn} = \sum_{m=1}^{\infty}\left[\frac{2}{T}P_{cm}\int_{-T/2}^{T/2}\cos\left(\frac{m2\pi z}{L}\right)\sin\left(\frac{n2\pi x}{T}\right)dz\right. \tag{A.18}$$

$$\left.+\frac{2}{T}P_{sm}\int_{-T/2}^{T/2}\sin\left(\frac{m2\pi z}{L}\right)\sin\left(\frac{n2\pi z}{T}\right)dz\right], \tag{A.19}$$

$$\Downarrow$$

$$K_{sn} = \sum_{m=1}^{\infty}\left[P_{cm}\varepsilon_c(m,n)+P_{sm}\varepsilon_s(m,n)\right], \tag{A.20}$$

where $\varepsilon_c(m,n)$ and $\varepsilon_s(m,n)$ are defined as

$$\varepsilon_c(m,n) = \frac{2}{T}\int_{-T/2}^{T/2}\cos\left(\frac{m2\pi x}{L}\right)\sin\left(\frac{n2\pi x}{T}\right)dx, \tag{A.21}$$

$$\varepsilon_s(m,n) = \frac{2}{T}\int_{-T/2}^{T/2}\sin\left(\frac{m2\pi x}{L}\right)\sin\left(\frac{n2\pi x}{T}\right)dx. \tag{A.22}$$

Appendix B

Coefficients

$$
\begin{array}{rclrcl}
C_{1n} & = & \mathcal{B}_{\mathcal{I}0}(m_n R_r), & C_{2n} & = & \mathcal{B}_{\mathcal{K}0}(m_n R_r), \\
C_{3n} & = & \mathcal{B}_{\mathcal{I}1}(m_n R_r), & C_{4n} & = & \mathcal{B}_{\mathcal{K}1}(m_n R_r), \\
C_{5j} & = & \mathcal{B}_{\mathcal{I}0}(q_j R_r), & C_{6j} & = & \mathcal{B}_{\mathcal{K}0}(q_j R_r), \\
C_{7j} & = & \mathcal{B}_{\mathcal{I}1}(q_j R_r), & C_{8j} & = & \mathcal{B}_{\mathcal{K}1}(q_j R_r), \\
C_{9n} & = & \mathcal{B}_{\mathcal{I}0}(m_n R_m), & C_{10n} & = & \mathcal{B}_{\mathcal{K}0}(m_n R_m), \\
C_{11n} & = & \mathcal{B}_{\mathcal{I}1}(m_n R_m), & C_{12n} & = & \mathcal{B}_{\mathcal{K}1}(m_n R_m), \\
C_{13j} & = & \mathcal{B}_{\mathcal{I}0}(q_j R_m), & C_{14j} & = & \mathcal{B}_{\mathcal{K}0}(q_j R_m), \\
C_{15j} & = & \mathcal{B}_{\mathcal{I}1}(q_j R_m), & C_{16j} & = & \mathcal{B}_{\mathcal{K}1}(q_j R_m), \\
C_{17n} & = & \mathcal{B}_{\mathcal{I}0}(m_n R_s), & C_{18n} & = & \mathcal{B}_{\mathcal{K}0}(m_n R_s).
\end{array}
$$

$$
\mathbf{b}_{N1} = \left[\begin{array}{cccc} b_{1_1} & b_{1_2} & \cdots & b_{1_N} \end{array} \right], \tag{B.1}
$$

$$
\mathbf{a}_{J2} = \left[\begin{array}{c} a_{2_1} \\ a_{2_2} \\ \vdots \\ a_{2_J} \end{array} \right], \tag{B.2}
$$

$$
\mathbf{b}_{J2} = \left[\begin{array}{c} b_{2_1} \\ b_{2_2} \\ \vdots \\ b_{2_J} \end{array} \right], \tag{B.3}
$$

$$
\mathbf{a}_{N3} = \left[\begin{array}{cccc} a_{3_1} & a_{3_2} & \cdots & b_{3_N} \end{array} \right], \tag{B.4}
$$

$$
\mathbf{C}_{NNa} = \left[\begin{array}{cccc} \left(\frac{C_{18_1}}{C_{17_1}} C_{11_1} + C_{12_1}\right) & 0 & \cdots & 0 \\ 0 & \left(\frac{C_{18_2}}{C_{17_2}} C_{11_2} + C_{12_2}\right) & \cdots & 0 \\ \vdots & \vdots & \ddots & 0 \\ 0 & 0 & \cdots & \left(\frac{C_{18_N}}{C_{17_N}} C_{11_N} + C_{12_N}\right) \end{array} \right] \tag{B.5}
$$

$$\mathbf{C}_{NNb} = \begin{bmatrix} \left(\frac{C_{18_1}}{C_{17_1}}C_{9_1} - C_{10_1}\right) & 0 & \cdots & 0 \\ 0 & \left(\frac{C_{18_2}}{C_{17_2}}C_{9_2} - C_{10_2}\right) & \cdots & 0 \\ \vdots & \vdots & \ddots & 0 \\ 0 & 0 & \cdots & \left(\frac{C_{18_N}}{C_{17_N}}C_{9_N} - C_{10_N}\right) \end{bmatrix} \quad \text{(B.6)}$$

$$\mathbf{C}_{NN1} = \begin{bmatrix} C_{1_1} & 0 & \cdots & 0 \\ 0 & C_{1_2} & \cdots & 0 \\ \vdots & \vdots & \ddots & 0 \\ 0 & 0 & \cdots & C_{1_N} \end{bmatrix}, \quad \text{(B.7)}$$

$$\mathbf{C}_{NN3} = \begin{bmatrix} C_{3_1} & 0 & \cdots & 0 \\ 0 & C_{3_2} & \cdots & 0 \\ \vdots & \vdots & \ddots & 0 \\ 0 & 0 & \cdots & C_{3_N} \end{bmatrix}, \quad \text{(B.8)}$$

$$\mathbf{C}_{JJ5} = \begin{bmatrix} C_{5_1} & 0 & \cdots & 0 \\ 0 & C_{5_2} & \cdots & 0 \\ \vdots & \vdots & \ddots & 0 \\ 0 & 0 & \cdots & C_{5_J} \end{bmatrix}, \quad \text{(B.9)}$$

$$\mathbf{C}_{JJ6} = \begin{bmatrix} C_{6_1} & 0 & \cdots & 0 \\ 0 & C_{6_2} & \cdots & 0 \\ \vdots & \vdots & \ddots & 0 \\ 0 & 0 & \cdots & C_{6_J} \end{bmatrix}, \quad \text{(B.10)}$$

$$\mathbf{C}_{JJ7} = \begin{bmatrix} C_{7_1} & 0 & \cdots & 0 \\ 0 & C_{7_2} & \cdots & 0 \\ \vdots & \vdots & \ddots & 0 \\ 0 & 0 & \cdots & C_{7_J} \end{bmatrix}, \quad \text{(B.11)}$$

$$\mathbf{C}_{JJ8} = \begin{bmatrix} C_{8_1} & 0 & \cdots & 0 \\ 0 & C_{8_2} & \cdots & 0 \\ \vdots & \vdots & \ddots & 0 \\ 0 & 0 & \cdots & C_{8_J} \end{bmatrix}, \quad \text{(B.12)}$$

$$\mathbf{C}_{JJ13} = \begin{bmatrix} C_{13_1} & 0 & \cdots & 0 \\ 0 & C_{13_2} & \cdots & 0 \\ \vdots & \vdots & \ddots & 0 \\ 0 & 0 & \cdots & C_{13_J} \end{bmatrix}, \quad \text{(B.13)}$$

$$\mathbf{C}_{JJ14} = \begin{bmatrix} C_{14_1} & 0 & \cdots & 0 \\ 0 & C_{14_2} & \cdots & 0 \\ \vdots & \vdots & \ddots & 0 \\ 0 & 0 & \cdots & C_{14_J} \end{bmatrix}, \tag{B.14}$$

$$\mathbf{C}_{JJ15} = \begin{bmatrix} C_{15_1} & 0 & \cdots & 0 \\ 0 & C_{15_2} & \cdots & 0 \\ \vdots & \vdots & \ddots & 0 \\ 0 & 0 & \cdots & C_{15_J} \end{bmatrix}, \tag{B.15}$$

$$\mathbf{C}_{JJ16} = \begin{bmatrix} C_{16_1} & 0 & \cdots & 0 \\ 0 & C_{16_2} & \cdots & 0 \\ \vdots & \vdots & \ddots & 0 \\ 0 & 0 & \cdots & C_{16_J} \end{bmatrix}, \tag{B.16}$$

$$\boldsymbol{\varepsilon}_{JN} = \begin{bmatrix} \varepsilon(1,1) & \varepsilon(1,2) & \cdots & \varepsilon(1,N) \\ \varepsilon(2,1) & \varepsilon(2,2) & \cdots & \varepsilon(2,N) \\ \vdots & \vdots & \ddots & \vdots \\ \varepsilon(J,1) & \varepsilon(J,2) & \cdots & \varepsilon(J,N) \end{bmatrix}, \tag{B.17}$$

$$\boldsymbol{\eta}_{JN} = \begin{bmatrix} \eta(1,1) & \eta(1,2) & \cdots & \eta(1,N) \\ \eta(2,1) & \eta(2,2) & \cdots & \eta(2,N) \\ \vdots & \vdots & \ddots & \vdots \\ \eta(J,1) & \eta(J,2) & \cdots & \eta(J,N) \end{bmatrix}, \tag{B.18}$$

$$\boldsymbol{\sigma}_N = \begin{bmatrix} \sigma(1) & \sigma(2) & \cdots & \sigma(N) \end{bmatrix}, \tag{B.19}$$

$$\mathbf{M}_N = \begin{bmatrix} M_1 & M_2 & \cdots & M_N \end{bmatrix}, \tag{B.20}$$

$$\mathbf{m}_N = \begin{bmatrix} \dfrac{\cos\left(\frac{m_1 \tau_m}{2}\right)}{m_1} \\ \dfrac{\cos\left(\frac{m_2 \tau_m}{2}\right)}{m_2} \\ \vdots \\ \dfrac{\cos\left(\frac{m_N \tau_m}{2}\right)}{m_N} \end{bmatrix}. \tag{B.21}$$

$$\mathbf{q}_J = \begin{bmatrix} \dfrac{\cos\left(\frac{q_1 \tau_m}{2}\right)}{q_1} & \dfrac{\cos\left(\frac{q_2 \tau_m}{2}\right)}{q_2} & \cdots & \dfrac{\cos\left(\frac{q_J \tau_m}{2}\right)}{q_J} \end{bmatrix}. \tag{B.22}$$

Appendix C

Graduation paper

Multi-physical Analysis and Design of a Slotless Tubular PM Actuator for High Acceleration 2-DoF Applications

K.J. Meessen,
Electromechanics and Power Electronics group,
e-mail: k.j.meessen@student.tue.nl

***Abstract*—This paper presents the analysis of a linear actuator for a rotary-linear system. In the analysis, four different topologies of a slotless tubular permanent magnet actuator (TPMA) are investigated. A unified semi-analytical solution for the magnetic field equations of the four topologies is derived in a two-dimensional axisymmetric coordinate system. Using these semi-analytical field equations, a time efficient analysis is performed on the magnetic field in the actuator. Several magneto-static models are implemented and coupled to electrical and thermal equations to design a TPMA for a high acceleration motion profile. Two topologies showed to be favorable for high acceleration applications and one of the prototypes is being built to validate the model.**

LIST OF SYMBOLS

A	Vector potential	Wb m^{-1}
B	Magnetic flux density	T
B_g	Magnetic loading in the airgap	T
B_{rem}	Remanent flux density	T
F	Force	N
H	Magnetic field strength	A m^{-1}
J_m	Moment of inertia	kg m^2
J	Current density	A m^{-2}
L	Axial length	m
M	Magnetization	A m^{-1}
Q	Electrical loading	A
R	Radius	m
T	Torque	N m
a	Acceleration	m s^{-2}
a_i	Coefficient	-
b_i	Coefficient	-
h	Heat transfer coefficient	W m^{-2} K^{-1}
j	Harmonic number	-
l	Length	m
m	Mass	kg
m_n	Spatial frequency	m^{-1}
n	Harmonic number	-
q_j	Spatial frequency	m^{-1}
r	Radial position	m
z	Axial position	m
α	Angular acceleration	rad s^{-2}
α_p	Magnet pitch to pole pitch ratio	-
$\mathcal{B}_{I0}$	Bessel function of first kind of 0^{th} order	-
$\mathcal{B}_{I1}$	Bessel function of first kind of 1^{th} order	-
$\mathcal{B}_{K0}$	Bessel function of second kind of 0^{th} order	-
$\mathcal{B}_{K1}$	Bessel function of second kind of 1^{th} order	-
ΔT	Temperature gradient	K
θ	Rotation around z	rad
μ_0	Permeability of vacuum	H m^{-1}
μ_r	Relative permeability	-
τ_{mr}	Axial length of radially magnetized magnet	m
τ_{mz}	Axial length of axially magnetized magnet	m
τ_p	pole pitch	m

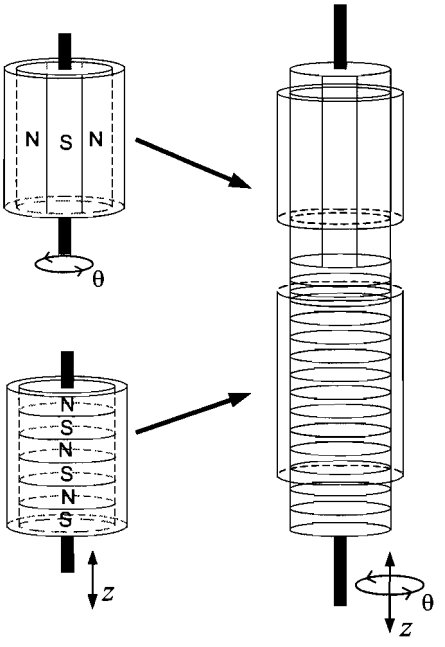

Fig. 1. Proposed rotary and a linear actuator on a single translator for 2-DoF applications.

I. INTRODUCTION

In robotic applications there is an increasing demand for high-speed actuation with high precision and high bandwidth capability. One particular application is the pick and place (P&P) robot to position surface mounted devices (SMD) on printed circuit boards (PCB), where components are picked from a feeder and placed on a PCB. The complete P&P action requires a four degrees of freedom (4-DoF) robotic motion, however this paper focusses on the 2-DoF (z, θ) placement module. More specifically, the combined rotary and linear actuator of Fig. 1, which, for the P&P application, combines a limited torque with a large linear force and acceleration requirement, as summarized in Table I. This paper concerns with the analysis needed to provide a system with a single translator which ameliorates both rotation and translation.

In literature, numerous combinations of linear and rotary actuators are presented. For example, in [1] and [2] multiple rotary induction machines are stacked in the axial direction to provide both motion in z- and θ- directions. A more specific

example for a pick and place module is presented in [3], where a 2-DoF system consisting of one translator and two stators is proposed. A different example is discussed in [4] and [5], where a switched reluctance machine (SRM) is proposed as a candidate to provide the 2-DoF. However, for both induction and switched reluctance machines, the power density is, in general, lower than for actuator systems utilizing permanent magnet materials.

Furthermore, for actuators using permanent magnets, numerous publications can be found, e.g. [6]–[9]. In general, these actuators can be separated into two classes: (a) with stacked z and θ magnetization patterns and (b) with checkerboard magnetization. Pattern (a) has the advantage of utilizing the stator field completely to produce both force and torque, however it increases the axial translator length and hence mass. When pattern (b) is used the stator coils are wound in the longitudinal direction to create torque, and in the circumferential direction to create linear force. However, pattern (b) covers only 50% of the translator surface with magnets, thus theoretically the force/torque capability is only 50% compared to a regular machine.

However, in [10] a third class of actuator topology is presented by means of an irregular magnetization pattern around the circumference. This actuator comprises two single-phase Lorentz force actuators, however, due to the large airgap, exhibits a low power density. The irregular magnetization pattern is achieved by a radially magnetized annular magnet (e.g. 90% of the circumference) interrupted by a segment magnetized in the opposite radial direction.

In this paper, a system as shown in Fig. 1 is proposed to provide both rotary and linear motion, i.e. utilizing the stacked magnetization pattern. Consequently, Section II and Section III present the rudimental equations for both rotary and linear actuators. To achieve a comprehensive design methodology, semi-analytical models of different topologies of the linear actuator are derived in Section IV, where Section VI implements these models to determine the achievable magnetic loading. In order to be able to determine the actuator performance Section VII introduces the electrical loading, since both magnetic and electrical loading are necessary to determine the force and acceleration for the extensive analysis presented in Section VIII.

II. Rotary Actuator

To provide the rotation in the 2-DoF system, a slotless permanent magnet actuator is proposed. This type of actuator is particularly interesting for precision applications as it exhibits almost zero torque ripple due to the absence of slots [11]. The load of the rotary actuator is

$$T_{load} = J_m \alpha, \tag{1}$$

TABLE I
SPECIFICATIONS OF THE ROTARY AND LINEAR ACTUATOR

Parameter	Rotary motion	Linear motion
Peak acceleration	3500 rad/s^2	150m/s^2
Stroke	> 360 °	35 mm
Peak force	-	40 N

where J_m is the moment of inertia of the complete 2-DoF translator and the load. As the load is only a tiny SMD, this component is neglected. The translator can be described as a cylinder, which has an inertia

$$J_m = mR^2, \tag{2}$$

where R is the radius of the translator, and m is the mass of the translator

$$m \propto R^2. \tag{3}$$

The produced torque of the actuator can be expressed as

$$T_{act} = 2\pi R_g^2 L B_g Q. \tag{4}$$

Therefore, a translator with a small radius is favorable as the load torque is

$$T_{load} \propto R^4, \tag{5}$$

and the actuator torque is

$$T_{act} \propto R^2. \tag{6}$$

Although this paper focusses on the design of the linear actuator, in this research, the performance of a rotary actuator for this application is investigated and presented in [12], [13].

III. Linear Actuator

For the linear motion, a tubular permanent magnet actuator (TPMA), as shown in Fig. 2, is proposed as they are particularly attractive linear machines due to the high force density and the absence of end-windings. A second obvious advantage is the round shaped translator which can easily be rotated without affecting the linear motion.

The thrust force of a TPMA can be expressed in the same form as the torque of a rotary actuator [14], by

$$F_z = 2B_g L \pi R_g Q. \tag{7}$$

When only the translator mass is considered as load, and the friction is neglected, the acceleration capability of the actuator is

$$a = \frac{F_z}{m_{tr}}, \tag{8}$$

where the mass of the cylindrical translator, is

$$m_{tr} \propto R^2. \tag{9}$$

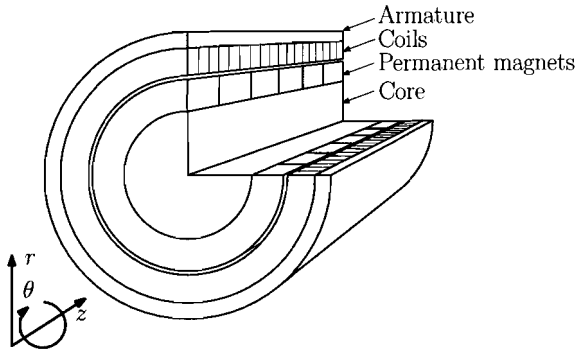

Fig. 2. A slotless tubular permanent magnet actuator.

As can be seen, the force increases linearly with the radius, while the mass increases with the radius squared. Therefore, the acceleration decreases linearly with the radius, thus as for the rotary actuator, a small radius is favorable for a high acceleration level.

The tubular actuator consists of a stator and a translator, where the moving magnet actuator is preferred since it does not require connections to the moving components. Further, the stator contains coils and is mostly either slotted or slotless, where the highest force density can be achieved when a slotted structure is used [15]. However, as mentioned for the rotary actuator, the slotted structure has some major disadvantages. e.g. the reluctance in the airgap is not uniform resulting in an extra force component called cogging force. This can be minimized by introducing typical pole-slot combination, albeit that this reduces the winding factor, and hence, the force capability. As the actuator is designed for a precision positioning application, a smooth force characteristic is desired. An additional disadvantage is the manufacturability of such a structure especially in low volume actuators. On the contrary, in a slotless structure, the stator consist solely of a soft-magnetic tube, hence, the actuator structure in this paper is chosen to be slotless.

In order to have a design tool which facilitates both the characteristic and the mean value of the force in a time-efficient way, semi-analytical descriptions of the magnetic field distribution are derived. These semi-analytical equations describe the magnetic field as a function of the geometric parameters of the actuator. The main advantage over using finite element analysis (FEA) to design an actuator is the time efficient calculation of the field distribution, and the ease of adding other physical behavior, e.g. thermal, to these models to create a powerful and very fast multi-physical design tool. Therefore, in this paper the design tools are based on these semi-analytical equations. Although this method provides an accurate and very fast prediction of the force waveform, the solution of the field equations becomes very complicated for more complex structures, i.e. slotted actuators and end-effects. As the actuator investigated in this paper has a slotless structure, the method based on the semi-analytical equations is very suitable.

IV. Semi-analytical description

Several papers have been written on the subject of designing tubular actuators using semi-analytical field equations. In [16]–[18] semi-analytical solutions for the magnetic fields in different tubular actuator topologies are presented, and [19] compares the force density of three different topologies. Although these papers are very extensive, the conclusions from [19] cannot be used in this research as the force is maximized instead of the acceleration. These two quantities are strongly connected but show different optima. The semi-analytical solutions presented in [16], and [17] show excellent agreement with FEA, however the resulting equations presented in the papers cannot be straightforwardly implemented. Therefore, this paper completely reconsiders the analysis and presents a novel unified semi-analytical description for four different translator topologies.

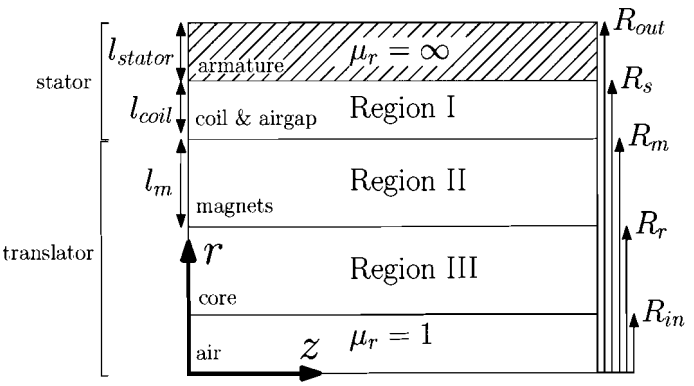

Fig. 3. Different regions in a slotless tubular actuator drawn in the r-z plane.

In order to apply the semi-analytical field-equations, the tubular actuator is divided in several regions as shown in Fig. 3. In the model, the following assumptions are made:

1) The soft-magnetic parts are infinitely permeable, which is valid for flux density levels below 1.3 T [12].
2) The actuator is infinitely long, the end-effects are neglected.
3) The permanent magnets have a linear demagnetization characteristic, and are fully magnetized in the direction of magnetization.

The semi-analytical description of the actuator is obtained by solving the magneto-static field equations using the vector potential, $\vec{A}$, defined as

$$\vec{B} = \nabla \times \vec{A}, \tag{10}$$

where $\vec{B}$ is the magnetic flux density [20]. Due to the symmetry in the circumferential direction in tubular actuators, the magnetic flux density, $\vec{B}$, has only an r- and a z-component. Therefore, the magnetic vector potential has only a circumferential, θ-component and the vector potential can be treated like a scalar potential. The two components of the magnetic field as function of A_θ are

$$B_r = -\frac{\partial}{\partial z} A_\theta, \tag{11}$$

$$B_z = \frac{\partial}{r \partial r} r A_\theta. \tag{12}$$

As only the magnetic field due to the permanent magnets in the actuator is calculated here, with no current in the windings, the magnetic vector potential has to be solved in two different regions. The regions are shown in Fig. 3, where the properties of region II and region III depend on the topology of the actuator. Region II has different magnet patterns, and region III can either be soft-magnetic or non-magnetic. In the source free regions, the Laplace equation has to be solved

$$\nabla^2 \vec{A}_{\mathrm{I,III}} = 0, \tag{13}$$

and in the magnet region, the Poisson equation has to be solved

$$\nabla^2 \vec{A}_{\mathrm{II}} = -\mu_0 \nabla \times \vec{M}, \tag{14}$$

where $\vec{M}$ is the magnetization vector describing the magnet array on the translator by a Fourier series.

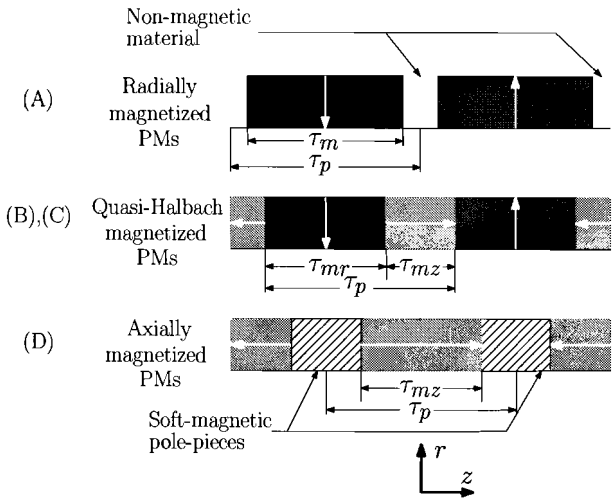

Fig. 4. Magnetization of region II for the different topologies drawn in the r-z plane.

V. Translator topologies

In this paper, four different TPMA translator topologies are investigated, comprising of, (A), radially magnetized permanent magnets on the translator, (B), quasi-Halbach magnet array mounted on a soft-magnetic core, (C), quasi-Halbach magnet array mounted on a non-magnetic core, and (D), axially magnetized magnets with a non-magnetic core. These four topologies have three different magnet patterns which are shown in Fig. 4.

Solving the Laplace equation, (13), and the Poisson equation, (14), results in a vector potential with a Bessel distribution in the $\vec{r}$-direction and a sinusoidal distribution in the $\vec{z}$-direction. Using the relations (11) and (12), the magnetic flux density, $\vec{B}$, in the different regions is

$$
\begin{aligned}
B_{\mathrm{I}r} &= \sum_{n=1}^{\infty}\Big(a_{1n}\mathcal{B}_{\mathcal{I}1}(m_n r)+b_{1n}\mathcal{B}_{\mathcal{K}1}(m_n r)\Big)\sin(m_n z),\\
B_{\mathrm{I}z} &= \sum_{n=1}^{\infty}\Big(a_{1n}\mathcal{B}_{\mathcal{I}0}(m_n r)-b_{1n}\mathcal{B}_{\mathcal{K}0}(m_n r)\Big)\cos(m_n z),\\
B_{\mathrm{II}r} &= \sum_{n=1}^{\infty}\Big[\Big(\mathcal{K}_{an}(m_n r)+a_{2n}\Big)\mathcal{B}_{\mathcal{I}1}(m_n r)\\
&\quad -\Big(\mathcal{K}_{bn}(m_n r)-b_{2n}\Big)\mathcal{B}_{\mathcal{K}1}(m_n r)\Big]\sin(m_n z),\\
B_{\mathrm{II}z} &= \sum_{n=1}^{\infty}\Big[\Big(\mathcal{K}_{an}(m_n r)+a_{2n}\Big)\mathcal{B}_{\mathcal{I}0}(m_n r)\\
&\quad +\Big(\mathcal{K}_{bn}(m_n r)-b_{2n}\Big)\mathcal{B}_{\mathcal{K}0}(m_n r)\Big]\cos(m_n z),\\
B_{\mathrm{III}r} &= \sum_{n=1}^{\infty}\Big(a_{3n}\mathcal{B}_{\mathcal{I}1}(m_n r)+b_{3n}\mathcal{B}_{\mathcal{K}1}(m_n r)\Big)\sin(m_n z),\\
B_{\mathrm{III}z} &= \sum_{n=1}^{\infty}\Big(a_{3n}\mathcal{B}_{\mathcal{I}0}(m_n r)-b_{3n}\mathcal{B}_{\mathcal{K}0}(m_n r)\Big)\cos(m_n z),
\end{aligned}
\tag{15}
$$

where $a_{1n}, b_{1n}, a_{2n}, b_{2n}, a_{3n}, b_{3n}$ are coefficients derived from the boundary conditions and given in the appendices together with the functions $\mathcal{K}_{an}$ and $\mathcal{K}_{bn}$, m_n is the spatial frequency which contains only odd harmonics

$$
m_n = \frac{(2n-1)\pi}{\tau_p}. \tag{16}
$$

The coefficients a_{1n} to b_{3n} are found by considering periodicity in the axial direction and by applying boundary conditions. General boundary conditions can be found by evaluating the integral form of the Maxwell equations over control volumes at material interfaces. [20] This results in

1) The tangential component of $\vec{H}$ is continuous if the surface current density at the interface is zero.
2) The normal component of $\vec{B}$ is continuous across an interface.

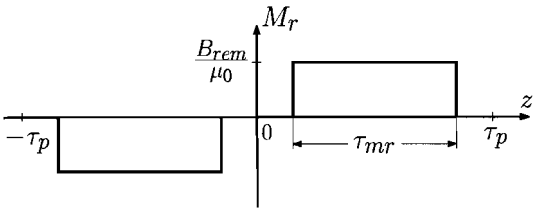

Fig. 5. Radial magnetization vector of PMs.

A. Radially magnetized topology

In Fig. 4A, the magnetization of region II (Fig. 3) of the radially magnetized topology is shown. As the core of this topology is soft-magnetic, region III has an infinite permeability as mentioned in section V. Therefore, the vector potential in region III, $\vec{A}_{\mathrm{III}}$, is not taken into account and a Dirichlet boundary condition on $r = R_r$ is added. This reduces the number of coefficients to be solved as a_{3n} and b_{3n} are not used. The magnetization vector, as shown in Fig. 5, is expressed as a Fourier series with only a component in the $\vec{r}$-direction

$$
\begin{aligned}
\vec{M} = M_r\vec{r} &= \sum_{n=1}^{\infty} M_{rn}\sin(m_n z)\,\vec{r},\\
M_{rn} &= \frac{4B_{rem}}{\mu_0\tau_p m_n}\sin\Big(\frac{m_n\tau_p}{2}\Big)\sin\Big(\frac{m_n\tau_p\alpha_p}{2}\Big),
\end{aligned}
\tag{17}
$$

where α_p is the magnet pitch τ_{mr} to pole pitch, τ_p, ratio.

The boundary conditions for this problem can be formulated as

$$
\begin{aligned}
B_{\mathrm{I}z}(r,z)\big|_{r=R_s} &= 0, &(18)\\
H_{\mathrm{II}z}(r,z)\big|_{r=R_r} &= 0, &(19)\\
B_{\mathrm{I}r}(r,z)\big|_{r=R_m} &= B_{\mathrm{II}r}(r,z)\big|_{r=R_m}, &(20)\\
H_{\mathrm{I}z}(r,z)\big|_{r=R_m} &= H_{\mathrm{II}z}(r,z)\big|_{r=R_m}. &(21)
\end{aligned}
$$

which should hold for all z. Solving these equations results in the solution given in appendix B.

B. Quasi-Halbach magnetized topology with soft-magnetic core

The second investigated topology has a quasi-Halbach magnetization and a soft-magnetic core, as shown in Fig. 4B. The advantage of a Halbach magnet array is the flux concentration at one side of the magnets and a more sinusoidal flux density in the airgap [21], [22]. In an ideal Halbach magnet array the magnets are sinusoidally magnetized. However, in practice it is relatively difficult to manufacture magnets with an ideal Halbach magnetization. Therefore, a simplified form, referred to as quasi-Halbach is used here. As can be seen in Fig. 6, the resulting magnetization vector has both a radial and an axial component and can be expressed as

$$\begin{aligned}\vec{M} &= M_r\vec{r} + M_z\vec{z} = \sum_{n=1}^{\infty} M_{rn}\sin(m_n z)\,\vec{r} \\ &\quad + \sum_{n=1}^{\infty} M_{zn}\cos(m_n z)\,\vec{z}, \\ M_{rn} &= \frac{4B_{rem}}{\mu_0\tau_p m_n}\sin\left(\frac{m_n\tau_p}{2}\right)\sin\left(\frac{m_n\tau_p\alpha_p}{2}\right), \quad (22) \\ M_{zn} &= \frac{4B_{rem}}{\mu_0\tau_p m_n}\sin\left(\frac{m_n(1-\alpha_p)\tau_p}{2}\right), \quad (23)\end{aligned}$$

where α_p is defined as τ_{mr}/τ_p. The regions and boundary conditions for this problem are the same as for the radially magnetized topology as shown in (18-21). The difference between the radially and quasi-Halbach topology is the magnetization vector as can be seen in Fig. 4. Solving the equations results in the solution given in appendix C.

C. Quasi-Halbach magnetized topology with non-magnetic core

The third topology is very similar to the second topology. However, due to the self-shielding properties of a Halbach magnet array, region III can be non-magnetic. This results in a translator with a lower mass and therefore probably higher acceleration levels. As region III is non-magnetic, the vector potential has to be solved in this region as well, resulting in two extra coefficients and other boundary conditions. The

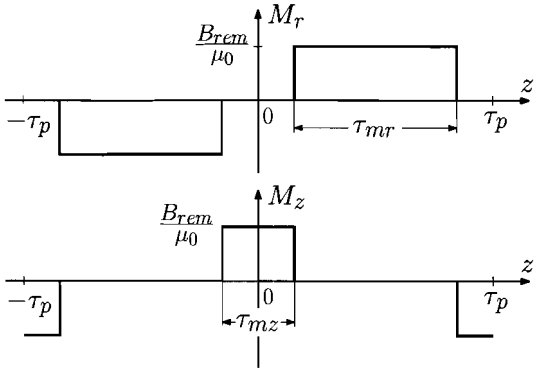

Fig. 6. Quasi-Halbach magnetization vector.

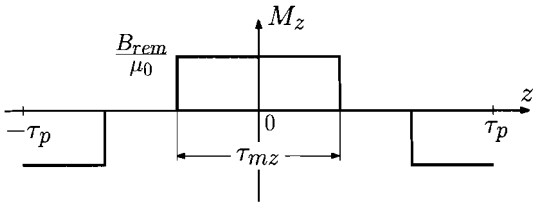

Fig. 7. Axial magnetization vector.

boundary conditions for this problem are

$$\begin{aligned}B_{\mathrm{I}z}(r,z)\big|_{r=R_s} &= 0, \quad (24) \\ A_{\mathrm{III}\theta}(r,z)\big|_{r=0} &= 0, \quad (25) \\ B_{\mathrm{I}r}(r,z)\big|_{r=R_m} &= B_{\mathrm{II}r}(r,z)\big|_{r=R_m}, \quad (26) \\ B_{\mathrm{II}r}(r,z)\big|_{r=R_r} &= B_{\mathrm{III}r}(r,z)\big|_{r=R_r}, \quad (27) \\ H_{\mathrm{I}z}(r,z)\big|_{r=R_m} &= H_{\mathrm{II}z}(r,z)\big|_{r=R_m}, \quad (28) \\ H_{\mathrm{II}z}(r,z)\big|_{r=R_r} &= H_{\mathrm{III}z}(r,z)\big|_{r=R_r}. \quad (29)\end{aligned}$$

The solution for these equations can be found in appendix D.

D. Axially magnetized topology with non-magnetic core

In the fourth topology the axially magnetized permanent magnets at the translator are separated by soft-magnetic pole pieces. This increases the complexity of this problem as the soft-magnetic pole pieces introduce axial boundary conditions in region II which consist of only the magnets. Therefore, the vector potential and the flux density in region II require another definition

$$\begin{aligned}B_{\mathrm{II}r} &= \sum_{j=1}^{\infty}\Big(a_{1n}\mathcal{B}_{\mathcal{I}1}(q_j r) + b_{1n}\mathcal{B}_{\mathcal{K}1}(q_j r)\Big)\sin(q_j z), \\ B_{\mathrm{II}z} &= \sum_{j=1}^{\infty}\Big(a_{1n}\mathcal{B}_{\mathcal{I}0}(q_j r) - b_{1n}\mathcal{B}_{\mathcal{K}0}(q_j r)\Big)\cos(q_j z),\end{aligned} \quad (30)$$

where q_j is the spatial frequency in this region defined as

$$q_j = \frac{2j\pi}{\tau_{mz}}. \quad (31)$$

The magnetization vector as shown in Fig. 7 for this topology is

$$\begin{aligned}\vec{M} = M_z\vec{z} &= \sum_{n=1,2,3,..}^{\infty} M_n\cos(m_n z)\,\vec{z}, \\ M_n &= \frac{4B_{rem}}{\mu_0\tau_p m_n}\sin\left(\frac{m_n\alpha_p\tau_p}{2}\right). \quad (32)\end{aligned}$$

Note that α_p is redefined as τ_{mz}/τ_p. The boundary conditions

TABLE II
DIMENSIONS OF THE TPMA IN THE PARAMETRIC ANALYSIS

R_{out} (mm)	9.00
R_s (mm)	8.00
R_m (mm)	6.25
R_r (mm)	2.25
R_{in} (mm)	1.25

for this problem are

$$B_{\mathrm{I}z}\big|_{r=R_s} = 0, \quad (33)$$

$$B_{\mathrm{III}r}\big|_{r=0} = 0, \quad (34)$$

$$B_{\mathrm{II}r}\big|_{|z|=\frac{\tau_{mz}}{2}} = 0, \quad (35)$$

$$B_{\mathrm{I}r}\big|_{r=R_m,|z|<\frac{\tau_{mz}}{2}} = B_{\mathrm{II}r}\big|_{r=R_m,|z|<\frac{\tau_{mz}}{2}}, \quad (36)$$

$$H_{\mathrm{I}z}\big|_{r=R_m,|z|<\frac{\tau_{mz}}{2}} = H_{\mathrm{II}z}\big|_{r=R_m,|z|<\frac{\tau_{mz}}{2}}, \quad (37)$$

$$\int_{R_r}^{R_m} 2\pi r B_{\mathrm{II}z}\big|_{z=\frac{\tau_{mz}}{2}}\,dr = \int_{\frac{\tau_{mz}}{2}}^{\frac{\tau_p}{2}} 2\pi R_m B_{\mathrm{I}r}\big|_{r=R_m}\,dz - \int_{\frac{\tau_{mz}}{2}}^{\frac{\tau_p}{2}} 2\pi R_r B_{\mathrm{III}r}\big|_{r=R_r}\,dz, \quad (38)$$

$$B_{\mathrm{II}r}\big|_{r=R_r,|z|<\frac{\tau_{mz}}{2}} = B_{\mathrm{III}r}\big|_{r=R_r,|z|<\frac{\tau_{mz}}{2}}, \quad (39)$$

$$H_{\mathrm{II}z}\big|_{r=R_r,|z|<\frac{\tau_{mz}}{2}} = H_{\mathrm{III}z}\big|_{r=R_r,|z|<\frac{\tau_{mz}}{2}}. \quad (40)$$

Appendix E includes the solution for the coefficients.

However, to design a permanent magnet actuator the force has to be calculated, defined by (7), and hence the magnetic and the electrical loading need to be determined as discussed in the next Sections.

VI. MAGNETIC LOADING

The solutions of the field equations in the previous section are implemented to perform a parametric research on geometric parameters. The analysis is started from a TPMA with dimensions as stated in Table II. The properties of the permanent magnets are shown in Table IV. Indirectly, saturation has been taken into account by applying a constraint to the flux density in both the core and the armature for topologies (A) and (B). The same constraint is applied to the flux density in the pole pieces in topology (D).

In the first analysis, the pole pitch, τ_p, and the magnet length, l_m, are varied while R_m is kept constant and R_r varies with l_m. The two parameters are varied in the range

$$5.0\text{mm} < \tau_p < 15.0\text{mm},$$
$$2.0\text{mm} < l_m < 4.3\text{mm},$$

in 40 steps. The magnetic flux density is calculated in the middle of the coil at $r = R_s - \frac{l_{coil}}{2}$ and in the armature and the core. The four topologies show similar maximum values. However, topologies (A) and (B) show very high flux densities in the soft-magnetic core. This will cause saturation and reduction of the flux density in a real machine.

The second analysis is performed only on topologies (B), (C), and (D). The pole pitch, τ_p, and the magnet pitch to pole pitch ratio, α_p, are varied considering the maximum magnet length (i.e. $l_m = 4.3mm$). The two parameters are varied in the range

$$5.0\text{mm} < \tau_p < 15.0\text{mm},$$
$$0.1 < \alpha_p < 0.9,$$

in 40 steps. The magnetic flux density is calculated in the middle of the coil at $r = R_s - \frac{l_{coil}}{2}$ and in the armature, core and the pole pieces for topology (D). Topology (B) shows an optimum for the flux density in the coil at $\alpha_p = 0.8$ for a pole pitch of $\tau_p = 15$mm. However, the flux density in the armature and the core are again very high. Topologies (C) and (D) show an optimum for the flux density in the coil at $\tau_p \approx 8$mm, $\alpha_p \approx 0.4$ and $\tau_p \approx 8.5$mm, $\alpha_p \approx 0.9$, respectively. As shown in Fig. 8 and Fig. 9, the maximum values are approximately the same. For topology (D) an increasing α_p results in a smaller width of the pole piece, resulting in a higher flux density in the pole piece which can cause saturation. Note that the highest value of the fundamental of the flux density in the coil results in the highest peak force.

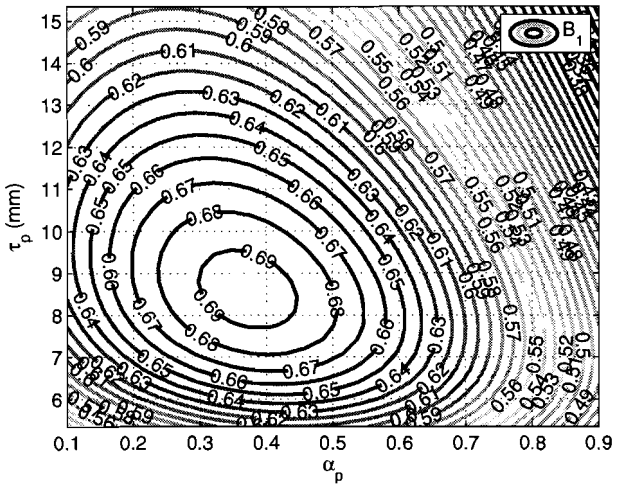

Fig. 8. Simulation results for topology (C). The amplitude of the fundamental of the flux density (B_1) in the middle of the coil, $r = Rs - \frac{l_{coil}}{2}$, versus pole pitch, τ_p, and α_p.

The main conclusion of the parametric search on the magnetic loading of the actuator is that all investigated topologies show similar maximum values of the magnetic field in the coil. However, the topologies with soft-magnetic core result in a very high flux density in the core, resulting in a decreased performance of the actuator. In addition, this soft-magnetic core increases the mass of the translator resulting in a lower acceleration at the same force level. Therefore, the quasi-Halbach topology with non-magnetic core, (C), and the axially magnetized topology, (D), are favorable over topologies (A) and (B).

VII. ELECTRICAL LOADING

The electrical loading of an actuator is defined by the geometric parameters of the windings and the electrical properties of these windings.

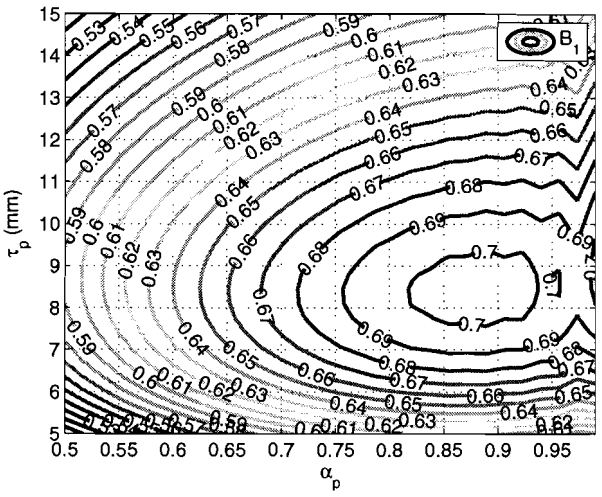

Fig. 9. Simulation results for topology (D). The amplitude of the fundamental of the flux density (B_1) in the middle of the coil, $r = Rs - \frac{l_{coil}}{2}$, versus pole pitch, τ_p, and α_p.

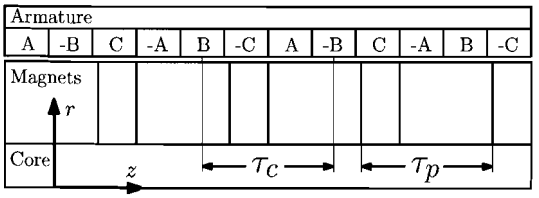

Fig. 10. TPMA BLAC winding topology for a slotless actuator.

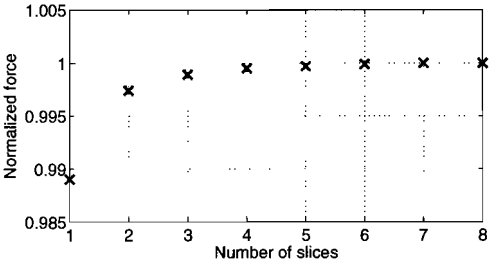

Fig. 11. number of slices in the coil area versus normalized force used for the force calculation.

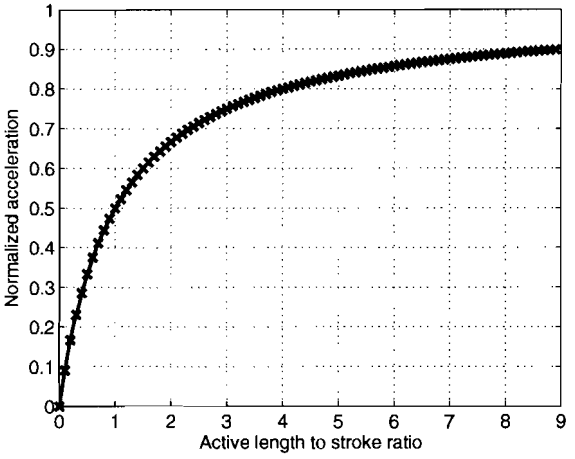

Fig. 12. Normalized acceleration versus the active length to stroke ratio.

A. Winding configuration

Slotless actuators exhibit no cogging force due to stator slotting, and the flux density in the coil in topologies (C) and (D) contains a negligible amount of higher harmonics. Therefore, there is no need for fractional coil pitch to pole pitch ratio to reduce EMF harmonics. To obtain a high winding factor, full pitch BLAC windings, as shown in Fig. 10, are implemented. While using this winding arrangement, the force is only produced by the fundamental of the flux density and the current.

B. Electrical configuration

While the magnetic loading is primarily limited by material properties, the electrical properties of the actuator are mainly restricted by thermal constraints. The current density in the coil region defines the heat produced due to dissipation in the windings. Due to this heat, the temperature difference between the armature and the ambient rises to

$$\Delta T = J^2 l_{coil} \rho_{Cu} \left(R_s - \frac{l_{coil}}{2} \right) \frac{1}{k_p R_{out} h}, \qquad (41)$$

where k_p is the packing factor of the coil region. In this expression, the coil and armature are assumed to be perfect heat conductors which is a good approximation [23]. The heat transfer coefficient can have values of approximately 20 $Wm^{-2}K^{-1}$ for natural cooling, up to 70 $Wm^{-2}K^{-1}$ when forced air cooling is used [24].

VIII. Force and Acceleration

The thrust force in a slotless TPMA can be calculated by applying the Lorentz force equation (42) in the coil region

$$\vec{F}_z = \int_{V_{coil}} \left(\vec{J} \times \vec{B} \right) dV, \qquad (42)$$

However, in topology (D) a second force component exists due to the soft-magnetic pole pieces which results in a position dependent reluctance of the airgap. This reluctance force component is calculated with a FEA. The results show that this component is very small compared to the Lorentz force and therefore neglected.

Although both $\vec{J}$ and $\vec{B}$ can be described analytically, the integral is difficult, if not impossible, to solve analytically. Therefore, the integral is approximated by modeling multiple current sheets in the coil region. The coil is split into several slices where in each slice the magnetic flux density, $\vec{B}$ is calculated and multiplied by the current in the current sheet, which is put in the middle of the slice. As shown in Fig. 11, a small number of slices gives a very good approximation of the force. Therefore, calculation time can be saved by using a small number of slices without a reduced accuracy.

A. Acceleration

As presented before, the acceleration is dependent on force and the translator mass, hence active length and stroke of the

TABLE III
PARAMETERS MODELS

Parameter	Topology C	Topology D
l_{stator} (mm)	1.00	1.00
l_g (mm)	0.25	0.25
R_r (mm)	2.00	2.00
R_{in} (mm)	1.25	1.25
τ_p (mm)	8.33	8.33
α_p	0.40	0.75
h ($\mathrm{Wm^{-2}K^{-1}}$)	10.00	10.00
ΔT (K)	40.00	40.00
l_{active} (mm)	100.00	100.00
l_{trans} (mm)	144.94	143.69
k_p	0.60	0.60
Duty cycle	0.34	0.34

translator. Therefore, the acceleration is a function of the active length to stroke ratio and the force, which is linear to the active length of the translator, as depicted in Fig. 12.

The field equations derived in Section V, the results from the parametric search on the magnetic loading in Section VI, the winding configuration given in Fig. 10 and equation (41), are combined in two models. The first one of the quasi-Halbach topology with non-magnetic core, and the second one of the axially magnetized topology. In the simulation the force and acceleration are calculated for several values of coil length, l_{coil}, and magnet length, l_m. The other parameters of both models are listed in Table III. The material properties are shown in Table IV.

As the temperature of the actuator is an important constraint, the current in the coils is varied to have a constant ΔT. As a result of the changing outer area due to a changing $l_m + l_{coil}$, the power dissipated in the coil varies while ΔT is constant (see (41)). In Fig. 13 and Fig. 14, the results of the simulations are shown for topologies (C) and (D), respectively. The dashed lines show values of constant force, the solid lines values of constant acceleration. The thick line marks the flux density in the armature, and for topology (D) the flux density in the pole pieces. To avoid saturation, a working point above this line is required. The cross-marks show the best combinations of values for l_{coil} and l_m.

As can be seen, increasing the magnet length results in a higher force capability. However, the increased magnet length causes a rise of the translator mass resulting in a lower acceleration. Therefore, a trade-off has to be made as both high acceleration and high peak force are required. Note that increasing the active length results in a higher force as well, without affecting the acceleration negatively.

A second important aspect in actuator design is efficiency. Therefore, a second model is created, where the current density

TABLE IV
MATERIAL PROPERTIES

Property	Value	Description
B_{rem} (T)	1.2	Remanent flux density PM
μ_r	1.05	Relative permeability of PM
μ_0 ($\mathrm{Hm^{-1}}$)	$4\pi \cdot 10^{-7}$	Permeability of vacuum
ρ_{Cu} (Ωm)	$1.71 \cdot 10^{-8}$	Resistivity of copper
ρ_{sm} ($\mathrm{kgm^{-3}}$)	$7.68 \cdot 10^{3}$	Mass density of soft-magnetic material
ρ_{pm} ($\mathrm{kgm^{-3}}$)	$7.60 \cdot 10^{3}$	Mass density of PM
ρ_{core} ($\mathrm{kgm^{-3}}$)	$2.70 \cdot 10^{3}$	Mass density of core (aluminium)

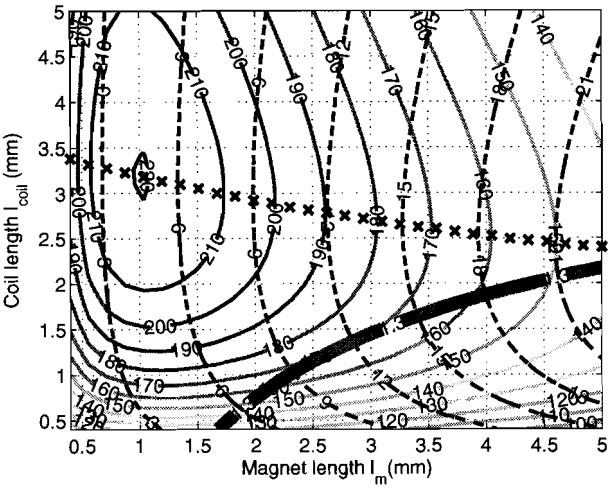

Fig. 13. Force (dashed line) and acceleration (solid line) of topology C, quasi-Halbach magnetization, versus coil length, l_{coil}, and magnet length, l_m. The current in the coils changes to have a constant $\Delta T = 40°\mathrm{C}$ in all cases.

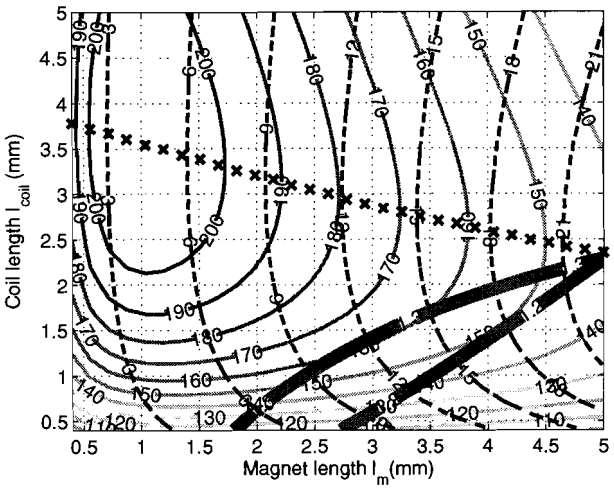

Fig. 14. Force (dashed line) and acceleration (solid line) of topology D, axial magnetization, versus coil length, l_{coil}, and magnet length, l_m. The current in the coils changes to have a constant $\Delta T = 40°\mathrm{C}$ in all cases.

is varied to maintain a constant power dissipation in the coils. Fig. 15 and Fig. 16 show the results of the simulation for topologies (C) and (D), respectively. The main difference between these results and the results for a constant ΔT are the shifted optima. Although the quasi-Halbach topology in Fig. 13 shows better results for a magnet length of 1 mm, the acceleration of the axial topology in Fig. 13 drops slightly less when the magnet length increases. Therefore, the quasi-Halbach topology is favorable when a small translator radius is used, for larger radii the axially magnetized topology becomes more preferable. Albeit that from manufacturing point of view, the axially magnetized topology is preferable. This topology contains less permanent magnet material, and all magnets are magnetized in the axial direction, which is easier than magnetizing in the radial direction.

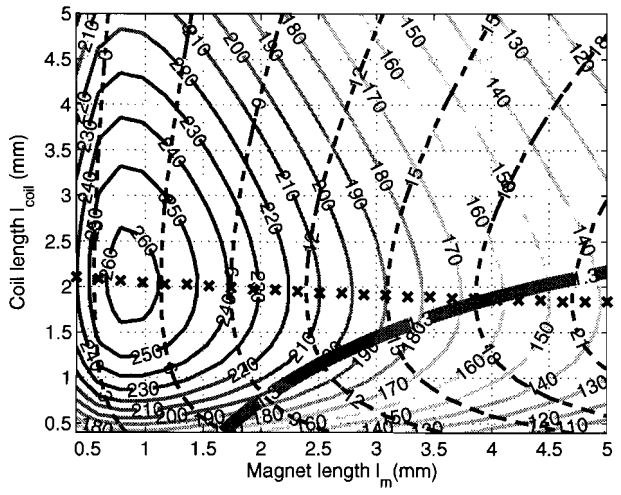

Fig. 15. Force (dashed line) and acceleration (solid line) of topology C, quasi-Halbach magnetization, versus coil length, l_{coil}, and magnet length, l_m. The current in the coils is changed to maintain a constant copper loss.

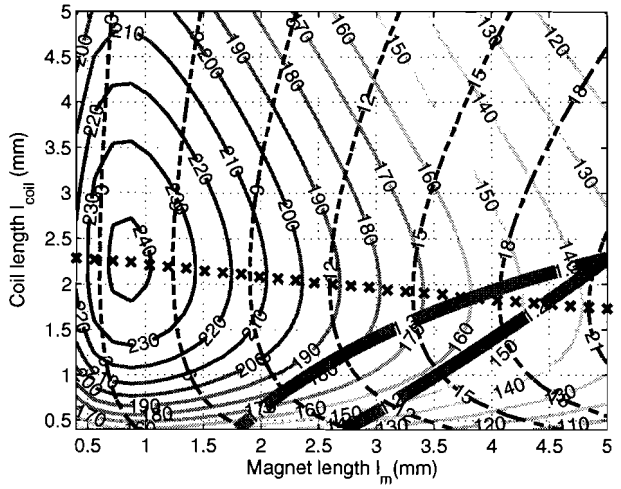

Fig. 16. Force (dashed line) and acceleration (solid line) of topology D, axial magnetization, versus coil length, l_{coil}, and magnet length, l_m. The current in the coils is changed to maintain a constant copper loss.

IX. Conclusions

In this paper, slotless tubular permanent magnet actuators for 2-DoF applications have been researched. The main focus of this paper is on the linear actuator, while the rotary actuator for this application is extensively researched in [12], [13]. A novel unified mathematical description of the magnetic field in the form of semi-analytical equations is proposed for the different researched topologies. The semi-analytical mathematical field description is obtained by applying sets of axisymmetric boundary conditions to the general field equations in the different regions of the actuator. The boundary conditions depend on the permanent magnet structure, the material of the different regions, and the magnetization pattern of the actuator. The advantage of this semi-analytical description is the time-efficient and accurate prediction of the magnetic fields in the actuator.

The unified electro-magnetic models are implemented and are coupled with multi-physical models describing electrical and thermal behavior resulting in a time-efficient analysis tool. Using these models, an extensive analysis is performed to synthesize the best structure according to the requested motion profiles and highest acceleration.

The axially magnetized topology and the quasi-Halbach topology with non-magnetic core show the best performance in terms of acceleration. The highest acceleration is achieved when the translator has a very small radius. The quasi-Halbach topology shows the highest acceleration capability. However, the axially magnetized topology is favorable from manufacturing point of view.

To validate the models used in this analysis, a prototype of the axially magnetized topology is being built and tested.

Appendix A

$$
\begin{aligned}
C_{1n} &= \mathcal{B}_{\mathcal{I}0}(m_n R_r), & C_{2n} &= \mathcal{B}_{\mathcal{K}0}(m_n R_r),\\
C_{3n} &= \mathcal{B}_{\mathcal{I}1}(m_n R_r), & C_{4n} &= \mathcal{B}_{\mathcal{K}1}(m_n R_r),\\
C_{5j} &= \mathcal{B}_{\mathcal{I}0}(q_j R_r), & C_{6j} &= \mathcal{B}_{\mathcal{K}0}(q_j R_r),\\
C_{7j} &= \mathcal{B}_{\mathcal{I}1}(q_j R_r), & C_{8j} &= \mathcal{B}_{\mathcal{K}1}(q_j R_r),\\
C_{9n} &= \mathcal{B}_{\mathcal{I}0}(m_n R_m), & C_{10n} &= \mathcal{B}_{\mathcal{K}0}(m_n R_m),\\
C_{11n} &= \mathcal{B}_{\mathcal{I}1}(m_n R_m), & C_{12n} &= \mathcal{B}_{\mathcal{K}1}(m_n R_m),\\
C_{13j} &= \mathcal{B}_{\mathcal{I}0}(q_j R_m), & C_{14j} &= \mathcal{B}_{\mathcal{K}0}(q_j R_m),\\
C_{15j} &= \mathcal{B}_{\mathcal{I}1}(q_j R_m), & C_{16j} &= \mathcal{B}_{\mathcal{K}1}(q_j R_m),\\
C_{17n} &= \mathcal{B}_{\mathcal{I}0}(m_n R_s), & C_{18n} &= \mathcal{B}_{\mathcal{K}0}(m_n R_s).
\end{aligned}
$$

$$
\mathcal{K}_{an}(m_n r) = -\mu_0 M_{rn} \int_{m_n R_r}^{m_n r} \frac{\mathcal{B}_{\mathcal{K}1}(x)}{\mathcal{B}_{\mathcal{I}1}(x)\mathcal{B}_{\mathcal{K}0}(x)+\mathcal{B}_{\mathcal{K}1}(x)\mathcal{B}_{\mathcal{I}0}(x)} dx,
$$

$$
\mathcal{K}_{bn}(m_n r) = -\mu_0 M_{rn} \int_{m_n R_r}^{m_n r} \frac{\mathcal{B}_{\mathcal{I}1}(x)}{\mathcal{B}_{\mathcal{I}1}(x)\mathcal{B}_{\mathcal{K}0}(x)+\mathcal{B}_{\mathcal{K}1}(x)\mathcal{B}_{\mathcal{I}0}(x)} dx.
$$

Appendix B
Radially Magnetized Topology

The coefficients a_{1n}, b_{1n}, a_{2n} and b_{2n} can be calculated as

$$
\mathbf{x} = \mathbf{E}^{-1} \cdot \mathbf{y}, \tag{43}
$$

where

$$
\mathbf{E} = \begin{bmatrix}
\mathbf{C_{17_N}} & -\mathbf{C_{18_N}} & \mathbf{0} & \mathbf{0} \\
\mathbf{0} & \mathbf{0} & \mathbf{C_{1_N}} & -\mathbf{C_{2_N}} \\
\mathbf{C_{11_N}} & \mathbf{C_{12_N}} & -\mathbf{C_{11_N}} & -\mathbf{C_{12_N}} \\
\mu_r \mathbf{C_{9_N}} & -\mu_r \mathbf{C_{10_N}} & -\mathbf{C_{9_N}} & \mathbf{C_{10_N}}
\end{bmatrix},
$$

$$
\mathbf{x} = \begin{bmatrix} \mathbf{a_{1_N}} \\ \mathbf{b_{1_N}} \\ \mathbf{a_{2_N}} \\ \mathbf{b_{2_N}} \end{bmatrix}, \mathbf{y} = \begin{bmatrix} \mathbf{0} \\ \mathbf{0} \\ \mathbf{C_{11_N}}\mathcal{K}_{\mathbf{a_N}} - \mathbf{C_{12_N}}\mathcal{K}_{\mathbf{b_N}} \\ \mathbf{C_{9_N}}\mathcal{K}_{\mathbf{a_N}} + \mathbf{C_{10_N}}\mathcal{K}_{\mathbf{b_N}} \end{bmatrix},
$$

where $\mathbf{C_{i_N}}$ is a N×N diagonal matrix with coefficients C_{in}, $\mathbf{a_{i_N}}$ and $\mathbf{b_{i_N}}$ are N×1 matrices with coefficients a_{in} and b_{in}, respectively, and $\mathcal{K}_{\mathbf{a_N}}$ and $\mathcal{K}_{\mathbf{a_N}}$ are N×1 matrices with coefficients $\mathcal{K}_{an}(m_n R_m)$ and $\mathcal{K}_{bn}(m_n R_m)$, respectively.

$$\mathbf{E}=\begin{bmatrix} \mathbf{C_{17_N}} & \mathbf{-C_{18_N}} & \mathbf{0} & \mathbf{0} & \mathbf{0} & \mathbf{0} \\ \mathbf{-\varepsilon_{JN}C_{11_N}} & \mathbf{-\varepsilon_{JN}C_{12_N}} & \mathbf{C_{15_J}} & \mathbf{C_{16_J}} & \mathbf{0} & \mathbf{0} \\ \mathbf{C_{9_N}} & \mathbf{-C_{10_N}} & \mathbf{-\frac{1}{\mu_r}\eta_{NJ}C_{13_J}} & \mathbf{\frac{1}{\mu_r}\eta_{JN}C_{14_J}} & \mathbf{0} & \mathbf{-\frac{1}{\mu_r}\sigma_N} \\ \mathbf{-R_mD_NC_{11_N}} & \mathbf{-R_mD_NC_{11_N}} & \mathbf{W_J\left(R_mC_{15_J}-R_rC_{7_J}\right)} & \mathbf{W_J\left(R_mC_{16_J}-R_rC_{8_J}\right)} & \mathbf{R_rD_NC_{3_N}} & \mathbf{\frac{R_m^2-R_r^2}{2}} \\ \mathbf{0} & \mathbf{0} & \mathbf{C_{7_J}} & \mathbf{C_{8_J}} & \mathbf{-\varepsilon_{JN}C_{3_N}} & \mathbf{0} \\ \mathbf{0} & \mathbf{0} & \mathbf{-\frac{1}{\mu_r}\eta_{NJ}C_{5_J}} & \mathbf{\frac{1}{\mu_r}\eta_{NJ}C_{5_J}} & \mathbf{C_{1_N}} & \mathbf{-\frac{1}{\mu_r}\sigma_N} \end{bmatrix} \tag{44}$$

APPENDIX C
QUASI-HALBACH WITH SOFT-MAGNETIC CORE

The coefficients a_{1n}, b_{1n}, a_{2n} and b_{2n} can be calculated as

$$\mathbf{x}=\mathbf{E}^{-1}\cdot\mathbf{y},$$

where

$$\mathbf{E}=\begin{bmatrix} \mathbf{C_{17_N}} & \mathbf{-C_{18_N}} & \mathbf{0} & \mathbf{0} \\ \mathbf{0} & \mathbf{0} & \mathbf{C_{1_N}} & \mathbf{-C_{2_N}} \\ \mathbf{C_{11_N}} & \mathbf{C_{12_N}} & \mathbf{-C_{11_N}} & \mathbf{-C_{12_N}} \\ \mu_r\mathbf{C_{9_N}} & -\mu_r\mathbf{C_{10_N}} & \mathbf{-C_{9_N}} & \mathbf{C_{10_N}} \end{bmatrix},$$

$$\mathbf{x}=\begin{bmatrix} \mathbf{a_{1_N}} \\ \mathbf{b_{1_N}} \\ \mathbf{a_{2_N}} \\ \mathbf{b_{2_N}} \end{bmatrix}, \mathbf{y}=\begin{bmatrix} \mathbf{0} \\ \mu_0\mathbf{M_{z_N}} \\ \mathbf{C_{11_N}\mathcal{K}_{a_N}-C_{12_N}\mathcal{K}_{b_N}} \\ \mathbf{C_{9_N}\mathcal{K}_{a_N}+C_{10_N}\mathcal{K}_{b_N}}-\mu_0\mathbf{M_{z_N}} \end{bmatrix},$$

where $\mathbf{M_{z_N}}$ is a N×1 matrix with coefficients M_{zn}.

APPENDIX D
QUASI-HALBACH WITH NON-MAGNETIC CORE

The coefficient b_{3n} is zero. The coefficients $a_{1n}, b_{1n}, a_{2n}, b_{2n}$, and a_{3n} can be calculated as

$$\mathbf{x}=\mathbf{E}^{-1}\cdot\mathbf{y},$$

where

$$\mathbf{E}=\begin{bmatrix} \mathbf{C_{17_N}} & \mathbf{-C_{18_N}} & \mathbf{0} & \mathbf{0} & \mathbf{0} \\ \mathbf{0} & \mathbf{0} & \mathbf{C_{1_N}} & \mathbf{-C_{2_N}} & \mathbf{-\mu_rC_{1_N}} \\ \mathbf{C_{11_N}} & \mathbf{C_{12_N}} & \mathbf{-C_{11_N}} & \mathbf{-C_{12_N}} & \mathbf{0} \\ \mu_r\mathbf{C_{9_N}} & -\mu_r\mathbf{C_{10_N}} & \mathbf{-C_{9_N}} & \mathbf{C_{10_N}} & \mathbf{0} \\ \mathbf{0} & \mathbf{0} & \mathbf{C_{3_N}} & \mathbf{C_{4_N}} & \mathbf{-C_{3_N}} \end{bmatrix}$$

$$\mathbf{x}=\begin{bmatrix} \mathbf{a_{1_N}} \\ \mathbf{b_{1_N}} \\ \mathbf{a_{2_N}} \\ \mathbf{b_{2_N}} \\ \mathbf{a_{3_N}} \end{bmatrix}, \mathbf{y}=\begin{bmatrix} \mathbf{0} \\ \mu_0\mathbf{M_{z_N}} \\ \mathbf{C_{11_N}\mathcal{K}_{a_N}-C_{12_N}\mathcal{K}_{b_N}} \\ \mathbf{C_{9_N}\mathcal{K}_{a_N}+C_{10_N}\mathcal{K}_{b_N}}-\mu_0\mathbf{M_{z_N}} \\ \mathbf{0} \end{bmatrix}.$$

APPENDIX E
AXIALLY MAGNETIZED WITH NON-MAGNETIC CORE

The coefficient b_{3n} is zero. The coefficients $a_{1n}, b_{1n}, a_{2j}, b_{2j}, a_{3n}$ and B_0 can be calculated as

$$\mathbf{x}=\mathbf{E}^{-1}\cdot\mathbf{y},$$

where $\mathbf{E}$ is defined in (44) and

$$\mathbf{x}=\begin{bmatrix} \mathbf{a_{1_N}} \\ \mathbf{b_{1_N}} \\ \mathbf{a_{2_J}} \\ \mathbf{b_{2_J}} \\ \mathbf{a_{3_N}} \\ B_0 \end{bmatrix}, \mathbf{y}=\begin{bmatrix} \mathbf{0} \\ \mathbf{0} \\ -\frac{\mu_0}{\mu_r}\mathbf{M_{z_N}} \\ \mathbf{0} \\ \mathbf{0} \\ -\frac{\mu_0}{\mu_r}\mathbf{M_{z_N}} \end{bmatrix},$$

where in (44) $\mathbf{D_N}$ is an 1×N matrix with coefficients

$$\frac{1}{m_n}\cos\left(\frac{m_n\tau_{mz}}{2}\right), \tag{45}$$

$\mathbf{W_J}$ is an 1×J matrix with coefficients

$$\frac{1}{q_j}\cos\left(\frac{q_j\tau_{mz}}{2}\right), \tag{46}$$

$\boldsymbol{\varepsilon_{JN}}$ is an J×N matrix with coefficients

$$\frac{\sin(v)}{v}-\frac{\sin(u)}{u}, \tag{47}$$

and $\boldsymbol{\eta_{JN}}$ is an N×J matrix with coefficients

$$\alpha_p\left(\frac{\sin(v)}{v}+\frac{\sin(u)}{u}\right), \tag{48}$$

where

$$v=j\pi-\frac{(2n-1)\pi\alpha_p}{2}\quad,\quad u=j\pi+\frac{(2n-1)\pi\alpha_p}{2}, \tag{49}$$

and $\boldsymbol{\sigma_N}$ is an 1×N matrix with coefficients

$$\frac{4}{(2n-1)\pi}\sin\left(\frac{(2n-1)\pi\alpha_p}{2}\right). \tag{50}$$

REFERENCES

[1] T. Onuki, W. J. Jeon, and M. Tanabiki, "Induction motor with helical motion by phase control," *IEEE Transactions on Magnetics*, vol. 33, pp. 4218–4220, September 1997.

[2] M. Rabiee and J. J. Cathey, "Verification of a field therory analysis applied to a helical motion induction motor," *IEEE Transactions on Magnetics*, vol. 24, pp. 2125–2132, July 1988.

[3] P. de Wit, J. van Dijk, T. Blomer, and P. Rutgers, "Mechatronic design of a z-ϕ induction actuator," *International Conference on Electrical Machines and Drives*, vol. 44, pp. 279–283, September 1997.

[4] Coleman, W. Conrad, and Whittier, "Linear and rotary actuator." U.S. Patent 4,607,197, IMC Magnetics Corporation, September 1986.

[5] Y. Sato, "Development of a 2-degree-of-freedom rotational/linear switched reluctance motor," *IEEE Transactions on Magnetics*, vol. 43, pp. 2564–2566, June 2007.

[6] G. L. Swift, "Rotary-linear actuator system method of manufacturing and method of using a rotary-linear actuator." U.S. Patent 6,798,087, Anorad Corporation, September 2004.

[7] A. Chitayat, "Rotary-linear actuator." U.S. Patent 5,982,053, Anorad Corporation, October 1998.

[8] M. R. Sogard, "Two-dimensional electric motor." U.S. Patent 6,455,956, Nikon Corporation, September 2002.
[9] M. K. Liebman, *Rotary-Linear Axes for High Speed Machining*. PhD thesis, Massachusetts Institute of Technology, September 2001.
[10] J. M. A. M. van Geel, J. C. Compter, and V. Kessler, "Electromagnetic actuator having a cylindrical translation coil and a toroidal rotation coil, actuator unit comprising the actuator and a measurement system, and machine comprising the actuator or the actuator unit." U.S. Patent 5,600,189, U.S. Philips Corporation, July 1995.
[11] T. S. Low, M. A. Jabbar, and T. S. Tan, "Design aspects and performance of a slotless pm motor for hard disk drives," *Industry Applications Magazine, IEEE*, vol. 3, pp. 43–51, Nov-Dec 1997.
[12] K. J. Meessen, "Report 2008.a.01." MSc thesis, Eindhoven University of Technology, January 2008.
[13] K. J. Meessen, J. J. H. Paulides, and E. A. Lomonova, "Eddy-current stator solid steel back-iron losses in small brushless permanent magnet machines," *IEEE International Magnetics Conference 2008*, to be published in May 2008.
[14] L. Encica, *Space-mapping based design strategies applied to novel automotive electromagnetic suspension systems*. PhD thesis, Eindhoven University of Technology, to be published in 2008.
[15] N. Bianchi, S. Bolognani, and D. D. Corte, "Tubular linear permanent magnet motors: An overall comparison," *IEEE Transactions on Industry Applications*, vol. 39, pp. 466–475, March 2003.
[16] J. Wang, G. W. Jewell, and D. Howe, "A general framework for the analysis and design of tubular linear permanent magnet machines," *IEEE Transactions on Magnetics*, vol. 35, pp. 1986–2000, May 1999.
[17] J. Wang and D. Howe, "Tubular modular permanent-magnet machines equipped with quasi-Halbach magnetized magnets - part I: Magnetic field distribution, emf, and thrust force," *IEEE Transactions on Magnetics*, vol. 41, pp. 2470–2478, September 2005.
[18] S. M. Jang, J. Y. Choi, S. H. Lee, S. K. Cho, and W. B. Jang, "Analysis of the tubular motor with Halbach and radial magnet array," *International Conference on Electrical Machines and Systems*, vol. 1, p. 250252, 2003.
[19] J. Wang, G. Jewell, and D. Howe, "Design optimisation and comparison of tubular permanent magnet machine topologies," *IEE Proc-Electr. Power Appl.*, vol. 148, pp. 456–464, September 2001.
[20] E. P. Furlani, *Permanent Magnet and Electromechanical Devices*. Academic Press, 2001.
[21] J. Mallinson, "One-sided fluxes - a magnetic curiosity?," *IEEE Transactions on Magnetics*, vol. 9, pp. 678–682, December 1973.
[22] K. Halbach, "Design of permanent multipole magnets with oriented rare earth cobalt material," *Nuclear Instruments and Methods*, vol. 69, no. 1, pp. 1–10, 1980.
[23] L. Encica, J. J. H. Paulides, E. A. Lomonova, and A. J. A. Vandenput, "Electromagnetic and thermal design of a linear actuator using output polynomial mapping," *Proc. IEEE Industry Applications Society 41st Annual Meeting (IAS 2006)*, vol. 4, pp. 1919–1926, Oct 2006.
[24] J. R. Hendershot and T. J. E. Miller, *Design Of Brushless Permanent-Magnet Motors*. Magna Physics Publishing and Clarendon Press, 1994.